Guard rings investigation of silicon sensors with modified pixel implant shapes in the context of the ATLAS experiment

Supervisor:
Prof. Maximiliano Sioli

Submitted by:
Serena Di Pede

Co-supervisor:
Dr. Jens Weingarten

A mio padre, per la sua travolgente grinta
A mia sorella, per il suo stimolante esempio
A mio fratello, per la sua dolcezza e genuinità
A mia madre, per la sua insostituibile inspirazione

Abstract

Based on the standard design of the planar n^+-in-n silicon pixel sensors of the innermost part of the tracking detector of the ATLAS experiment, six modified pixel designs were developed in Dortmund in order to increase the average electric field and thus the radiation hardness. The REINER pixel sensors contain these six modified pixel implantation shapes beside structures with the standard pixel design. Each pixel structure is provided by 13 guard rings and can be biased and investigated separately.

This thesis aims to deeply investigate the electrical performances of the REINER sensors. The individual pixel designs have been cut from the original full REINER structure for the first time and a study of the single structures has been performed. The obtained results show that the cut sensors are broken and cannot be properly used anymore. These unexpected results that have been obtained hint at the investigation of the multi-guard ring structure of the implants in order to investigate the strength of the electric field at the edge of the sensor.

The results show that the guard ring structure of each design properly works when a design is biased and its guard rings voltage measured. However, when the guard rings voltage is logged on another design, different from the biased one, the non-zero measurements proves that the pixel designs truly influence each other due to a non-ideal operation of the guard ring structure.

Contents

Introduction

During the second half of the 20th century, the huge progress in experimental particle physics has led to a deep understanding of the elementary particles and the fundamental forces in the Universe, which resulted in the building of the so-called Standard Model of particle physics. The experimental discoveries that confirmed the Standard Model were possible due to a series of development concerning accelerator and detector physics.

The **L**arge **H**adron **C**ollider (LHC) is currently the largest particle collider in the world. With energies up to $13\,\text{TeV}$ and a designed luminosity of $10^{34}\,\text{cm}^{-2}\text{s}^{-1}$, it enables the exploration of rare and high-energetic processes. However, to improve the precision of its results, the **H**igh-**L**uminosity LHC (HL-LHC) upgrade is planned to be implemented in 2026, providing higher event rate to improve the statistical precision in data analysis.

One of the four large experiments at the LHC is the ATLAS detector. Its pixel detector, the innermost part of the tracker, is composed of silicon sensors, which are the topic of this thesis. As the pixel detector is the closest to the interaction point, it represents a basic part of the track reconstruction. Its main requirements are high resolution and radiation hardness. With the planned increase of the luminosity, the radiation damage will be even intensified, therefore a new pixel detector featuring improved radiation hard sensors and read-out chips is needed.

Based on the standard design of the planar n^+-in-n sensors of the ATLAS IBL detector, six modified pixel designs have been developed in order to improve the sensor performance after irradiation. The REINER pixel sensors contain these six modified pixel implantation shapes beside two structures with the standard pixel design. These structures with different pixel designs are separated by guard rings to prevent the influence from each other. To evaluate the performance of the different pixel implanatation shapes and to check if they are really independent from each other, the guard rings behaviour is studied and verified.

In Chapter 2, the complex of accelerators at CERN is described with a major focus on the ATLAS experiment and the upgrade plans of its detectors. Since only silicon sensors are analysed in this thesis, an introduction to the theory of semiconductors is given in Chapter 3, with a deepening in the role of semiconductor detectors as particle detectors and the effects of an high radiation environment on them. In Chapter 4, a brief overview of silicon pixel detectors is given before describing in more details the silicon

sensors of the ATLAS pixel detector. Moreover, the working principles of a multi-guard ring structure is presented.

Chapter 5 presents the results of the investigation on the REINER sensors. Measurements for the building, improvement and verification of the setup are shown. The validation of the measurement techniques is discussed in details with test sensors before presenting the results on the cut REINER sensors. The guard rings investigation is performed in Chapter 6, with detailed description of the built setup, its improvement and verification with test sensors. The results of the study of the guard ring structure of the REINER sensors is presented, showing measurements of the individual pixel designs as well as measurements to test the influence among the different pixel implantation shapes. Lastly, conclusions and some outlooks are given in Chapter 7.

Chapter 1

The LHC Physics

The European Organisation for Nuclear Research (CERN) focuses mainly on the research on particle physics, studying the fundamental constituents of matter. But it's physics programme at the laboratory is more broader, ranging from nuclear to high-energy physics, from studies of antimatter to the possible effects of cosmic rays on clouds. Physicists at CERN use the world's most powerful particle accelerators and detectors to test the predictions and limits of the Standard Model. The Standard Model of particle physics is the theory which summarises today's knowledge of the fundamental particles and their interactions. Over the years, this theory has explained many experimental results and precisely predicted a range of phenomena, such that today the Standard Model is considered a well-tested physics theory.

Only the 4% of the known Universe contains ordinary matter while the remain 96% is dark matter and dark energy. Although being a great success of particle physics, the Standard Model describes then only a small portion of the known Universe and there are many open questions, such as the understanding of the gravitational force or the imbalance between antimatter and matter. Physicists at CERN are looking for answers to these questions and more.

1.1   The CERN Accelerator Complex

CERN operates a complex of machines that iteratively accelerate particles to increasingly higher energies. Each machine boosts the energy of a beam of particles before injecting the beam into the next machine in the sequence. The LHC is the last element of this chain and particle beams are accelerated up to 6.5 TeV per beam in there. Most of the other accelerators in the chain have their own experimental halls where beams are used for experiments at lower energies.

A schematic overview of the current accelerator complex is shown in Figure 1.1. Over the years, CERN has grown to its current size. Newer accelerators have been added to

the complex and the old ones have been replaced or upgraded in order to gain new capabilities.
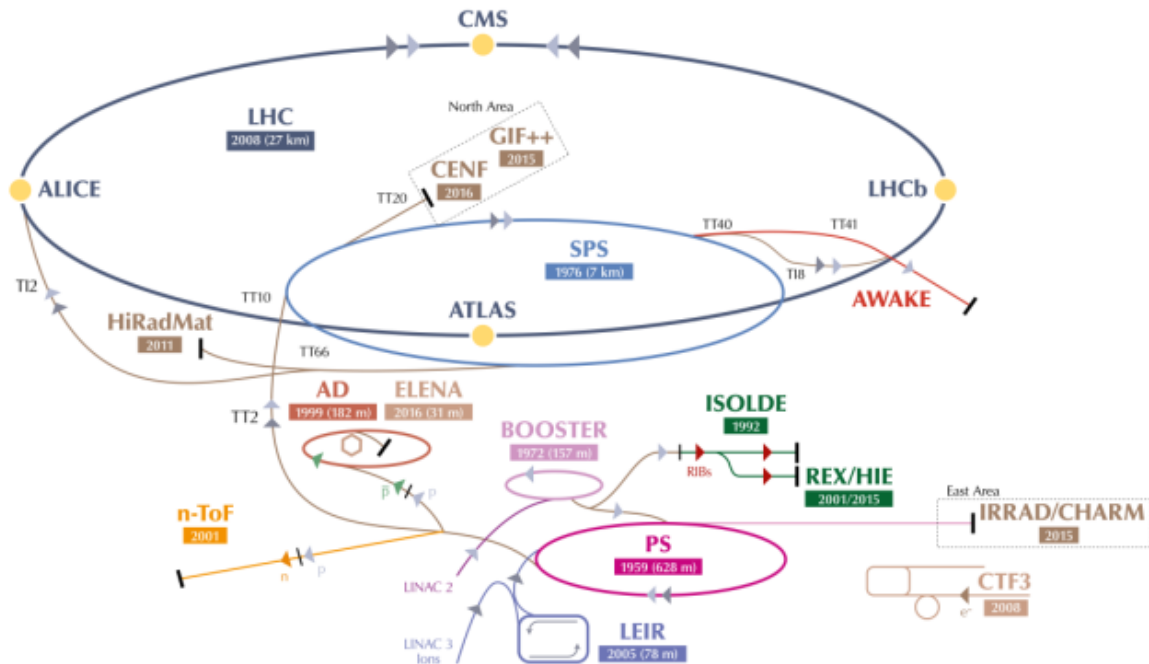
Figure 1.1: The CERN Accelerator Complex [1].

1.2   The Large Hadron Collider

The LHC started its operation in September 2008 and is currently the largest particle accelerator in the world with a circumference of 27 km and a maximum centre of mass energy $\sqrt{s} = 13$ TeV. Unlike other colliders like LEP (**L**arge **E**lectron **P**ositron Collider) or Tevatron, it collides particles with the same sign of electric charge (protons). The proton source in the LHC is a simple bottle of hydrogen gas. Then, an electric field is used to strip the hydrogen atoms of their electrons to yield protons.

Four pre-accelerators are used in order to boost the protons to the necessary energy for the injection in the LHC. The LINAC 2 (**LIN**ear **AC**celerator 2) is the first accelerator in the chain and accelerates protons up to the energy of 50 MeV. The beam is then injected into the second accelerator of the chain, the BOOSTER which accelerates protons up to 1.4 GeV for the injection into the **P**roton **S**ynchrotron (PS). The PS is a key component at CERN complex. With a circumference of 629 m, it accelerates protons up to 25 GeV. Afterwards, the protons are delivered to the experiments, the irradiation facilities in the

East Area or transferred to the **S**uper **P**roton **S**ynchrotron (SPS). The SPS is the second largest machine at CERN. With a circumference of 7 km, it accelerates particles up to 450 GeV in order to prepare the beams for the North Area experiments or the LHC.

At this point, the protons are finally ready to be transferred to the two different beam pipes of the LHC where they circulate in opposite directions so to be brought into collision inside the four detectors: ALICE (**A L**arge **I**on **C**ollider **E**xperiment), ATLAS (**A T**oroidal **LHC A**pparatu**S**), CMS (**C**ompact **M**uon **S**olenoid) and LHCb (**L**arge **H**adron **C**ollider **b**eauty). The ALICE experiment is a heavy-ion detector designed to study the physics of strongly interacting matter at extreme energy densities, such as occurred in the first 10^{-6} s after the Big Bang, where a phase of matter called the quark-gluon plasma forms. The LHCb is a forward-detector designed for the investigation of b-quarks. ATLAS and CMS are more general purpose detectors and reconstruct particles leaving the interaction point in any direction [2].

At LHC, heavy ions acceleration is also possible. Lead ions start from a source of vaporised lead and enter in the LINAC 3 before being collected and accelerated in the **L**ow **E**nergy **I**on **R**ing (LEIR). Then, they follow the same route to maximum energy already described for the protons.

1.3 The ATLAS Experiment

The ATLAS experiment is one of the two general-purpose detectors at LHC together with the CMS experiment. It explores a wide range of physics topics, with the primary focus of improving the understanding of the fundamental constituents of matter. Its layout is optimised for the discover and the study heavy particles, such as the Higgs boson or the top quark, at a high instantaneous luminosity. Luminosity is one of the key parameter of an accelerator's performance: the instantaneous luminosity indicates the number of potential collisions per surface unit over a given period of time and is expressed in $\text{cm}^{-2}\text{s}^{-1}$, while the integrated luminosity is expressed in fb^{-1} and is the integral of the instantaneous luminosity in a Run period [3]. For the Run periods see Section 1.4.

The nominal luminosity of $1 \times 10^{34} \, \text{cm}^{-2}\text{s}^{-1}$ at the LHC is achieved with multiple collisions per bunch crossing (pile-up). A high granularity of the detectors is necessary in order to be able to reconstruct and separate tracks (trajectories of electrically charged particles due to their ionization in the material of the detector) belonging from different primary vertices (the origin point of the reconstructed tracks) and possibly identify secondary vertices. Moreover, since an high luminosity also causes high radiation levels - especially close to the interaction point - detectors need to be sufficiently radiation hard.

Due to the wide range of physics processes studied, a large acceptance in pseudo-rapidity η is also required[1]. These requirements result in a 4π-detector surrounding the

---

[1]The pseudo-rapidity parameter is defined as $\eta = -\ln\tan(\theta/2)$ (with θ being the angle between the

interaction point from nearly all angles using highly granular sub-detectors.

The ATLAS detector is cylindrical with a length of 44 m, a diameter of 25 m and a weight of 7000 t. It is the largest instrumented particle detector ever constructed.
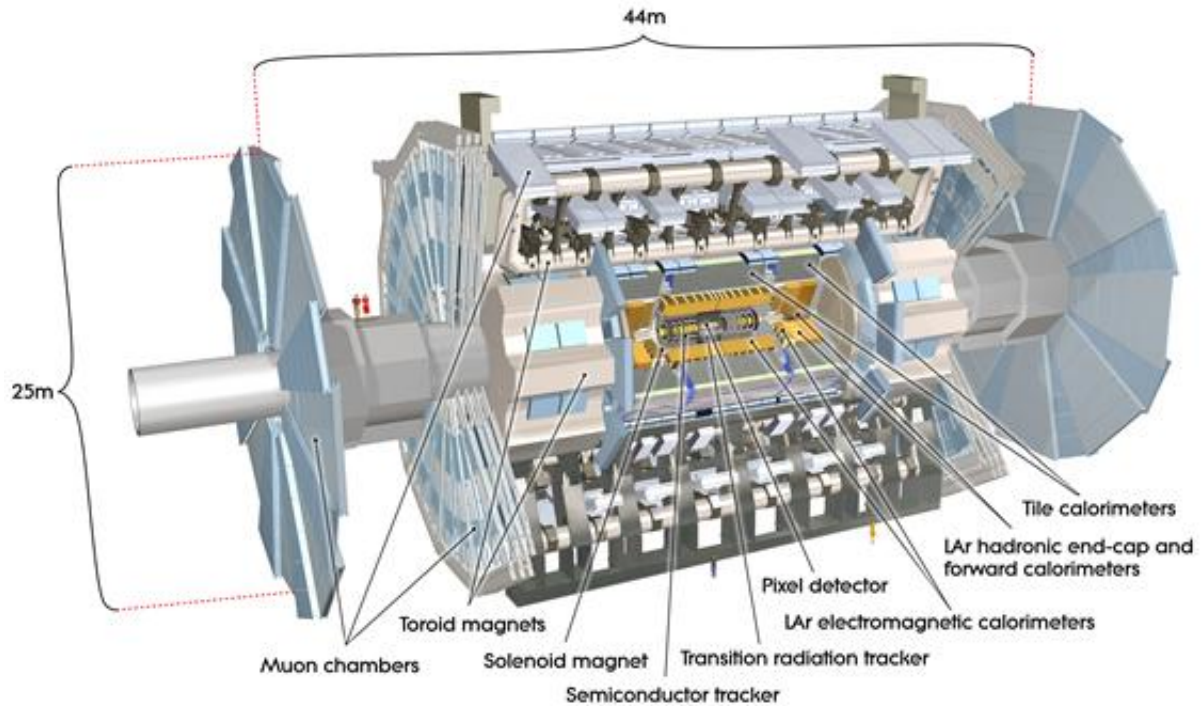
Figure 1.2: Computer generated cut-away view of the ATLAS detector [5].

All the different detecting components are arranged in sub-detectors around the collision point (Figure 1.2): the **I**nner **D**etector (ID), which obtains information about the trajectory, the charge and the momentum of the crossing charged particle; the **E**lectromagnetic and **H**adronic **Cal**orimeters (ECAL and HCAL), which measure the energy of the particles stopped inside themselves, and the Muon System, which detects muons that cross all the other inner sub-detectors. Neutrinos cannot be directly observed in the ATLAS detector. The interactions of different particles in the detector are shown in Figure 1.3.

To be able to measure the momentum and the charge of the crossing charged particles, ATLAS uses a magnet system consisting of two sub-systems: a thin superconducting

particle momentum and the positive direction of the beam axis) and is a quantity frequently used in colliding beam experiments to express angles with respect to the axis of the colliding beams. It has the value 0 for particle trajectories that are perpendicular to the beam, and positive or negative values for those at an angle to the beam [4].
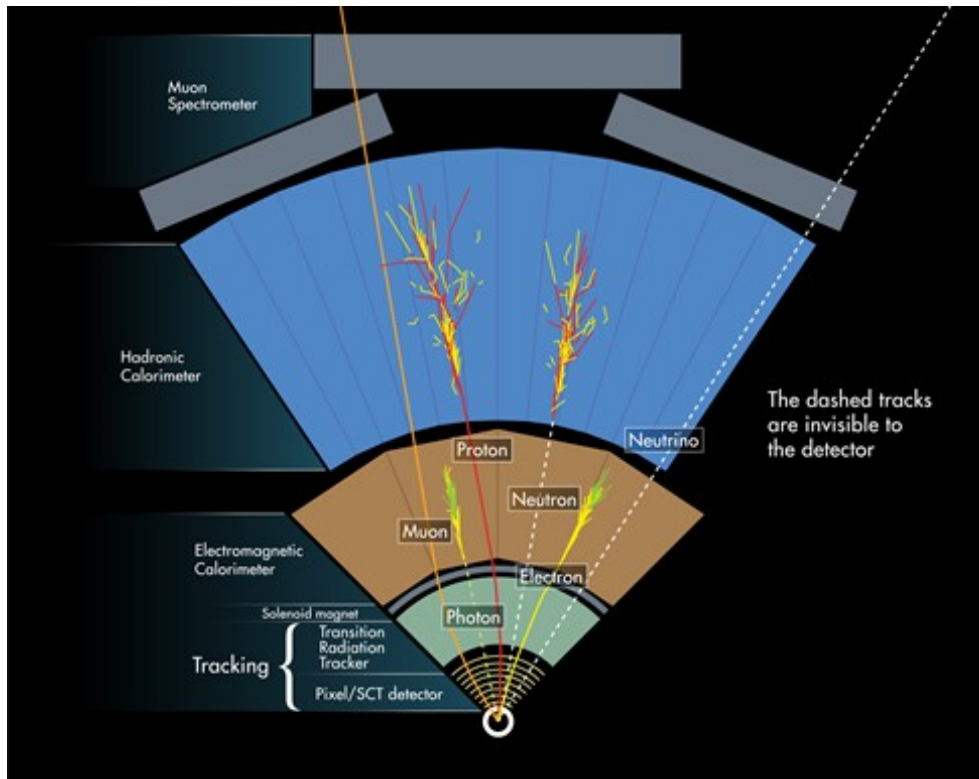
Figure 1.3: Detection of particles in the different sub-detectors of the ATLAS experiment [6].

solenoid surrounding the ID cavity, and three large superconducting toroids (one barrel and two end-caps[2]) arranged around the calorimeters.

The Inner Detector

The ID is the nearest detector to the collision point. It is very compact and highly sensitive, and consists of three sub-detectors, all immersed in a 2 T magnetic field generated by the central solenoid.

Approximately 1000 particles emerge from the collision point every 25 ns within $\eta <$ 2.5, creating a very large track density in the detector. The goal of the ID as tracking detector is to provide an excellent momentum and vertex resolution, while minimising cost and material. These high-precision measurements are provided using fine-granularity detectors. Figure 1.4 shows the layout of the ID components. Closer to the beam pipe there is the silicon pixel detector, which consists of four pixel sub-detectors, including the **I**nsertable **B**-**L**ayer (IBL), installed since the phase-0 upgrade in 2014 (see Section

---

[2]All the ATLAS sub-detectors have a cylindrical "barrel" area which covers the low η region, and the "end-cap" segments which enclose the barrel from both sides.
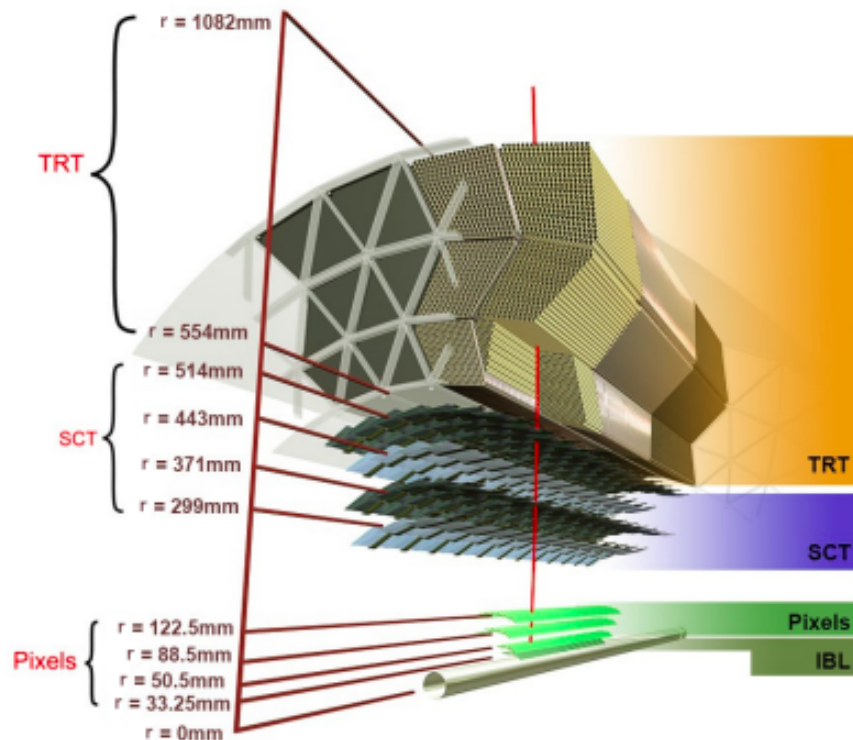
Figure 1.4: Sketch of the ATLAS Inner Detector showing all its components, including the IBL. The distances from the interaction point are also shown. [7]

1.5). At larger radii, there is the **S**emi-**C**onductor **T**racker (SCT), made of four double strip layers, and the **T**ransition **R**adiation **T**racker (TRT). These three sub-detectors in the ID are independent from each other but complementary.

The pixel detector and the SCT are precision tracking detectors and cover the region with $\eta < 2.5$. In the barrel region, they are arranged in concentric cylinders around the beam axis while in the end-cap regions they are located on disks perpendicular to the beam axis. The silicon pixel detectors allow to achieve the highest granularity around the vertex region. Their layers are segmented in the $(R\text{ - }\phi)$ and z direction, with typically three pixel layers crossed by each track[3]. All pixel sensors are identical and have a minimum pixel size in $(R\text{ - }\phi) \times z = (50 \times 400)\,\mu\text{m}^2$ [8].

Eight strip layers of the SCT are crossed by each track. In the barrel region, this detector uses small-angle (40 mrad) stereo strips to measure $(R\text{ - }\phi)$, while in the end-cap

---

[3]ATLAS uses a right-handed coordinate system with its origin at the interaction point, in the centre of the detector, and the z-axis along the beam pipe. The x-axis points from the interaction point to the centre of the LHC ring and the y-axis points upward. Cylindrical coordinates (r,ϕ) are used in the transverse plane, with ϕ being the aximuthal angle around the z-axis.

region has a combination of a set of strips running radially and a set of stereo strips. The mean strip *pitch* (distance), for both the strips in the barrel and in the end-caps, is $80\,\mu$m. The intrinsic accuracies, in the barrel and in the disks, of the pixel and strip modules, can be found in [8].

The TRT comprises many layers of gaseous straw tube elements interleaved with transition radiation material. It provides a large number of hits (typically 36 per track) and enables track-following up to $|\eta| = 2.0$.

The combination of precision trackers at small radii with the TRT at a larger radius gives a very robust pattern recognition and high precision in both the (R - ϕ) and z coordinates. In particular, the straw hits at the outer radius significantly contribute to the momentum measurement, since the lower precision per point compared to the silicon is compensated by the large number of measurements and longer measured track length [8].

The Calorimeter System

The calorimeter system consists of an ECAL, HCAL and **F**orward **Cal**orimeter (FCAL), and it covers the range $\eta < 4.9$. Calorimeters are designed to "absorb" most of the particles coming from a collision, forcing them to deposit all of their energy within the detector in order to measure it. Sampling calorimeters are designed alternating layers of "passive" (or absorbing) high-density material interleaved with layers of "active" materials.

The ECAL is situated directly behind the ID and uses liquid Argon (LAr) as active medium and lead as absorber. It is ideally suited for precision measurements of electrons and photons. Its total thickness is enough to cover > 22 radiation length (X_0) in the barrel, and $> 24\ X_0$ in the end-caps.

The HAD Calorimeter, at larger radii from the interaction point than the EM Cal, is made up of the **Tile Cal**orimeter (TileCal) in the barrel and the **H**adronic **E**nd-cap **C**alorimeter (HEC). The TileCal is placed directly outside the EM calorimeter envelope and is also a sampling calorimeter using scintillator tiles as active material while steel as absorber. The HEC consists of two independent wheels per end-cap and is located directly behind the end-cap of the ECAL. The HCAL, together with the ECAL, provides approximately 9.7 interaction length (λ) in the barrel, while 10 λ in the end-caps. These values are adequate to avoid punch-through into the Muon System and provide good resolution for high-energy jets.

The FCAL is also a sampling calorimeter using LAr providing $\sim 10\,\lambda$. It is made up of three modules: the first one uses copper as absorber to measure the energy of electromagnetic particles, the other two use tungsten to absorb hadrons.

The Muon System and the Magnets Configuration

Since the calorimeters cannot stop muons, a third important detector system is needed to measure their momentum, considering the deflection of muon tracks in the large superconducting toroid magnets.

Over the range $|\eta| < 1.4$, magnetic bending is provided by the large barrel toroid. For $1.6 < |\eta| < 2.7$, muon tracks are bent by two smaller end-cap magnets inserted into both ends of the barrel toroid. In the transition region $1.4 < |\eta| < 1.6$, magnetic deflection is provided by a combination of barrel and end-cap fields. This magnet configuration provides a field which is mostly orthogonal to the muon trajectories.

The Muon Spectrometer consists of four different types of gas chambers filled with a Ar/Co_2 mixture. A precision measurement of the track coordinates in the principal bending direction of the magnetic field is provided by the **M**onitored **D**rift **T**ubes (MDT). At large pseudo-rapidities, the **C**athode **S**trip **C**hambers (CSC, multiwire proportional chambers with cathodes segmented into strips) are used because of their higher granularity. The function of MDT and CSC is to perform precise tracking. Resistive Plate Chambers in the barrel and Thin Gap Chambers in the end-cap regions are instead used for triggering and to determine a second coordinate in the orthogonal direction determined by the precision-tracking chambers.

1.4   The HL-LHC project

The operation of the LHC is divided into multi-year runs. Between these runs, the **L**ong **S**hutdowns (LSs) take place in which the accelerators and the machines are upgraded. The current schedule is shown in Figure 1.5.

LHC started operations in Run 1 at $\sqrt{s} = 7\,\text{TeV}$, which was increased to $8\,\text{TeV}$ in 2012. On the 4 of July 2012 the ATLAS and CMS collaborations announced their first major discovery: the long-sought Higgs boson, a milestone in the verification of the Standard Model of particle physics [10, 11]. After two years of LS1, in spring 2015, the LHC restarted for Run 2 at an increased $\sqrt{s}$ of $13\,\text{TeV}$. A further increase of $\sqrt{s}$ to $14\,\text{TeV}$ is scheduled for Run 3 which will start in 2021. Along with the energy, also the instantaneous luminosity was increased during the years since higher luminosity allows the experiments to gather more data which enhances the possibility of observing rare processes and provides more accurate measurements of new particles.

The upgrade HL-LHC is scheduled to be completed in 2026, after the LS3. The goal is to increase the instantaneous luminosity up to $\mathcal{L} = 7.5 \times 10^{34}\,\text{cm}^{-2}\text{s}^{-1}$, which corresponds to an average number of proton-proton collisions per bunch crossing of $\langle \mu \rangle \sim 200$. This means that the integrated luminosity will reach $4000\,\text{fb}^{-1}$, which will improve the investigation of rare channels of Standard Model processes with better precision, as well as the search for processes of the physics Beyond the Standard Model (BSM).

Figure 1.5: Time schedule for the LHC/HL-LHC upgrade [9].

The HL-LHC physics program of the ATLAS experiment, for example, will focus on the precision measurement of the production and decay channels of the Higgs boson [12].

1.5 Upgrades of the ATLAS Tracking System

Phase-0 upgrade: the IBL

The IBL (*Insertable B-Layer*) was installed in the ATLAS experiment in 2014, during the LS1 [13]. It was designed to operate until the end of Phase-1, before the full tracker upgrade for the HL-HLC operation.

The IBL is a new layer of pixel sensors designed to fit between the B-Layer and a new smaller radius beam pipe. It consists of 14 carbon staves, each supporting 20 pixel sensor modules together with their electrical services and a cooling pipe.
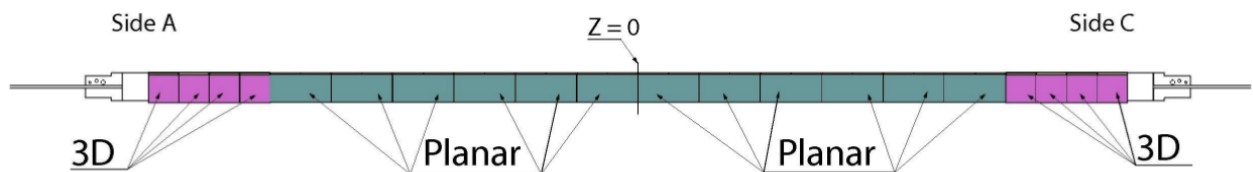
Figure 1.6: Longitudinal layout of planar and 3D modules on the IBL stave [13].

The stave layout is shown in Figure 1.6: twelve planar n^+-in-n sensors populate the central region while four 3D sensors are placed at the two stave extremities. For the sensors read-out, a new generation of Front-End electronics was developed, the FE-I4.

The planar sensors are based on the sensors of the three-layer pixel detector, but their design layout was revised to reduced the width of the inactive edge [14]. The pixel size was shrunk to $50 \times 200 \, \mu\text{m}^2$ and the pixel matrix was enlarged to be suitable for the new read-out chips. The sensors have a thickness of $200 \, \mu\text{m}$ and each is read out by two FE-I4. The 3D sensors are based on a novel concept for radiation hard silicon sensors and are placed at the stave extremities due to their vertical electrode orientation [15].

Both the planar and 3D sensor technologies will be described in Section 3.1 and the FE-I4 in Section 3.2.3.

Phase-2 upgrade: the ITk

With the challenging conditions expected for the HL-LHC upgrade, new requirements for tracking detectors are necessary in order to cope with the increased luminosity, data rate and radiation damage. For this reason, the ID of the ATLAS experiment will be replaced with the new Inner Tracker (ITk) during the phase-2 upgrade, starting in 2024. The ITk is an all-silicon detector designed to operate with an integrated luminosity of $4000 \, \text{fb}^{-1}$ and an average pile-up of $\langle \mu \rangle \sim 200$. It will use the same volume as the ID with the $2 \, \text{T}$ magnetic field generated from the central solenoid.

The layout of one quadrant of the ITk is shown in Figure 1.7. It consists of a pixel subsystem (shown in red) with five flat layers in the barrel enclosed by five pixel rings in end-caps region, and a strip subsystem (shown in blue) with four strip layers in the barrel region enclosed by six strip disks on each side. A more detailed description for the Pixel Detector subsystem and the Strip Detector subsystem can be found in the Technical Design Reports [16, 17].

The strip subsystem covers a pseudorapidity region of $|\eta| < 2.7$ while the pixel subsystem covers up to $|\eta| < 4$ [16]. The combination of the two systems is designed to have at least 9 precision measurement per track for the full width of the expected beam spot size, for any charged particle with $p_T > 1 \, \text{GeV}$, traversing the detector in $|\eta| < 4.0$ [18]. Apart from tracking performance, an important target is also the minimal use of material to achieve as little deposited energy in the detector volume as possible to improve the energy measurement in the calorimeter.

All the improvements in the ITk will increase the physics performance in identifying charged particles and measuring their properties while operating under the challenging HL-LHC conditions. An example of the improved momentum resolution for muons expected with the ITk is shown in Figure 1.8.
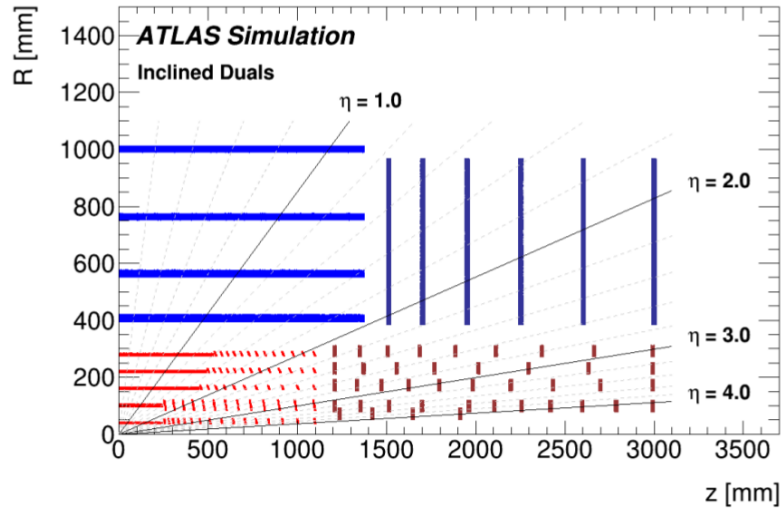
Figure 1.7: Schematic layout of one quadrant of the possible ITk. The Strip Detector sensors are represented in blue for the barrel and in dark blue for the end-cap region. The Pixel Detector sensors are shown in red and dark red, respectively, for the barrel and the end-cap rings [16].
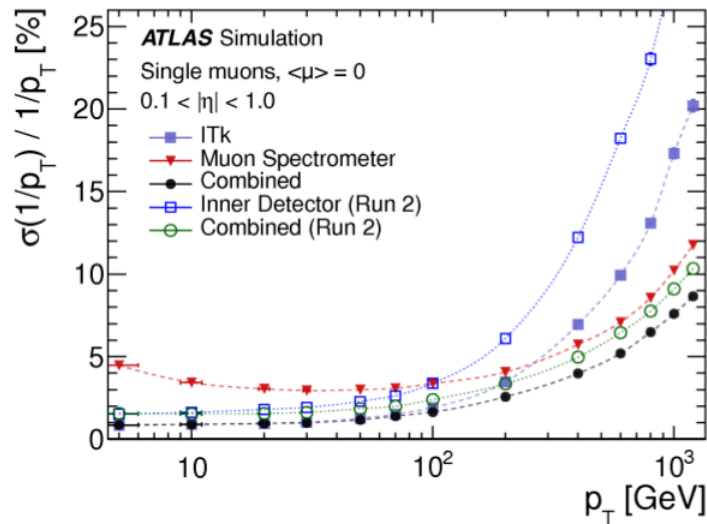
Figure 1.8: Combined muon momentum resolution as a function of the transverse muon momentum, and individual contributions from the ITk and the upgraded Muon Spectrometer [16].

Chapter 2

The Physics of Semiconductors

Nowadays, semiconductor detectors are used in a large variety of fields in science and technology. Their development also enriched particle physics, not only in computing or read-out electronics, but also as sensitive material in modern detectors. The success of semiconductor detectors is due to several unique properties such as the possibility to achieve a high spatial and temporal resolution, as well as an excellent energy resolution in spectroscopy.

As already explained in Chapter 2, the SCT and the Pixel Detector of the ATLAS ID are semiconductor detectors made with silicon, which is an important semiconductor of the fourth main group in the periodic table. Since the behaviour of semiconductors depends on many parameters like the temperature, the impurities' concentration or the magnetic field, an introduction into the theory of semiconductors is necessary for the description of the sensors.

2.1   Semiconductor Properties

2.1.1   Crystals and Electronic Band Model

For their use as particle detectors, semiconductor materials are required in the form of high-purity crystals. Crystals are solids in which the atoms are arranged in a well-defined periodic structure. The smallest assembly of atoms that can be repeated to form the entire crystal is called primitive cell, whose dimension is given by the lattice constant (see Figure 2.1). The form of these lattices is influenced by the semiconductor element. For example, silicon atoms always form diamond lattices where each atom of one sub-lattice is tetrahedrally surrounded by four atoms of the other sub-lattice and shares one electron with each of the the four neighbouring atoms, to form covalent bonds.

While in single atoms the electrons have discrete energy levels, atoms arranged in a lattice structure can influence each other, thus their electrons' energy levels split

into states which differ only in small amount of energy due to mutual interactions.
The allowed energy states are then grouped together in bands separated by forbidden gaps, called band gaps. The magnitude of these gaps is related to the nature of the chemical bonds in the solid. At room temperature the value of the forbidden energy gap E_g is 1.12 eV for Silicon and 0.665 eV for Germanium [20]. The E_g is expected to depend both on temperature and pressure since the electron energy levels depend on the spacing between atoms.

There are two energy bands: the lower-energy *valence* band and the higher-energy *conduction* band. E_V names the highest energy level of the valence band while E_C indicates the lowest energy level of the conduction band. The energy difference between the two levels is the energy gap E_g and represents the minimum amount of energy necessary to break a covalent bond and excite an electron from the valence to the conduction band. The magnitude of E_g depends also on the material composition and determines the electrical properties of the material, namely if it is an insulator, a conductor or a semiconductor (see Figure 2.2).

Figure 2.1: Diamond lattice of some representative elements like Silicon, Germanium or Carbon, with a being the lattice constant [19].

The E_F level drawn in Figure 2.2 is the Fermi energy, the highest energy state that can be occupied by an electron at a 0 K temperature. As can be seen in the figure, for insulators and semiconductors E_F is located in the band gap between the conduction and the valence band. At T = 0 K, both insulators and semiconductors would theoretically show no electrical conductivity: the valence band is completely occupied while the conduction band is completely empty. In metals instead, the valence and conduction bands overlap so there is no band gap and the E_F is in the overlapping region. The conduction band is partially filled and the electrons are available for conduction.

In semiconductors, at higher temperatures, thermal vibrations may break the covalent bond and a valence electron can migrate in the conduction band, leaving behind a free place (*hole*). This *electron-hole pair* (the free electron in the conduction band and the hole in the valence band) created is then available for conduction. For this reason, in semiconductors, the conductivity grows exponentially with temperature, instead of decreasing with temperature as in conductors. Insulators, instead, have larger band gap energy than semiconductors, thus even for excited electrons result too high overcome it.

2.1.2   Intrinsic Semiconductors

Intrinsic semiconductors contain no (in practice, very few) impurities compared with the number of thermally generated electron-hole pairs. These pairs are the charge carriers

Figure 2.2: The band structure of an intrinsic and extrinsic (doped) semiconductors, conductor and insulator [21].

and give rise to the intrinsic semiconduction characterized by equal concentrations of free electrons and holes in the crystal. This is because each thermal generated electron leaves a hole behind, therefore the number of conduction electrons equals the number of holes in the valence band, at equilibrium. The intrinsic charge carrier concentration n_i can be expressed with [20]:

$$n_i = \sqrt{N_C N_V} \exp \left(- \frac{E_g}{2kT} \right) \tag{2.1}$$

where N_C and N_V are the effective densities of states in the conduction and valence bands respectively, k is the Boltzmann constant and T the absolute temperature.

The conductivity in an intrinsic semiconductor is due both to the negatively and positively charge carriers instead of only electrons as for metals. It is also possible to determine the value of the conductivity σ by using the intrinsic carrier density n_i and the mobilities μ_e (e = electrons) and μ_h (h = holes), summing both the electrons and

holes current components [22]:

$$\sigma = en_i(\mu_e + \mu_h) \tag{2.2}$$

This value also gives the resistivity ρ which is just the inverse of σ. Since for silicon, at room temperature, $\mu_e = 1350$ cm^2/Vs and $\mu_h = 480$ cm^2/Vs [22]:

$$\rho_{Si} = \frac{1}{\sigma} = 230000\,\Omega\text{cm} \tag{2.3}$$

2.1.3 Doping: Extrinsic Semiconductors

Perfect crystals are never obtainable and real crystals usually contain various types of imperfections which have an influence on the electrical properties of semiconductors. These imperfections are chemical impurities or structural defects. In most cases, the properties of the material can be intentionally altered by adding small fractions of specific impurities. This procedure is called *doping* and can be performed either during the crystal growth or later in selected regions of the crystal. The obtained doped semiconductor is called *extrinsic*.

Depending on the type of the added material, an *n-type* semiconductor is obtained if there is an excess of electrons in the conduction band, or a *p-type* semiconductor if there are additional holes in the valence band (see Figure 2.3).
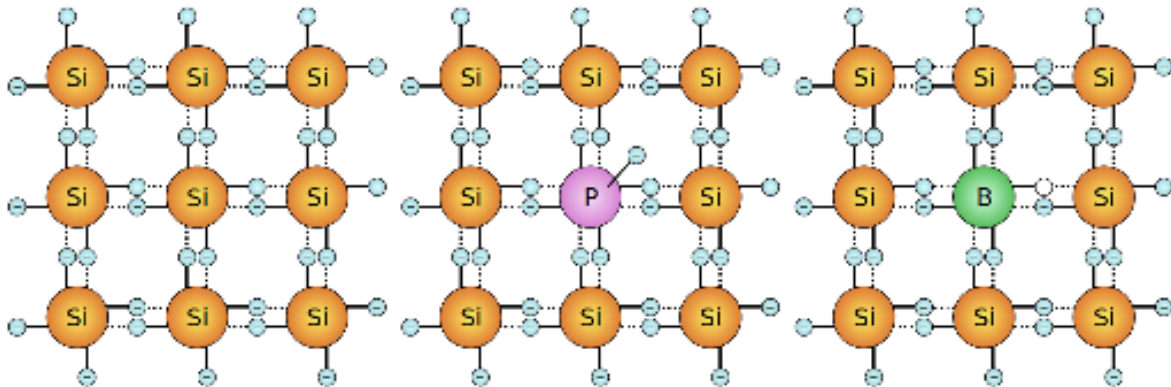
Figure 2.3: The lattice structure of silicon. From the left, the first 3x3 no-doped silicon cell, the n-doped (with phosphorus) silicon cell, and the p-doped (with boron) silicon cell [23].

n-type semiconductors

In the case of silicon, a small concentration of pentavalent (elements from the fifth group of the periodic table) impurities is added. As shown in Figure 2.3, the new phosphorus elements will occupy a substitutional site within the lattice, taking the place of normal

silicon atoms. Because now there are five valence electrons surrounding the impurity atom, one is left over after all covalent bonds with the four neighbours atoms have been formed. The extra electron is slightly bound to the original site and it takes a very little energy to dislodge it to form a conduction electron, without a corresponding hole.

These impurity atoms are usually referred to as *donors*, because they readily contribute to the conduction. Also, since they are not part of the regular lattice, they can occupy a position within the forbidden gap. Therefore, adding impurities introduces localized levels in the forbidden energy gap. E_D is the energy state related to the donors which is illustrated in Figure 2.2. Since it is close to the conduction band, electrons can be lifted to the conduction band by smaller thermal excitation. In this way, the concentration of donor impurities completely dominate the number of conduction electrons expected in the conduction band for the respective intrinsic material. The net effect in an extrinsic n-type material is that the number of conduction electrons is much greater and the number of holes much smaller than in the corresponding pure material. Moreover, the electrical conductivity is determined almost exclusively by the flow of electrons (now called the *majority carriers*), while the holes (now *minority carriers*) only play a small role.

The electrical conductivity of a doped semiconductor is always much larger than the corresponding pure material since the total number of charge carriers is now much greater. Consequently, the resistivity of a doped material is much smaller.

p-type semiconductors

Always in the case of silicon, the addition of trivalent (elements from the third group of the periodic table) impurities results in the situation that there is one fewer electron in the impurity's site than the surrounding silicon atoms. One covalent bond is left unsaturated but the present vacancy is a different kind of hole. If an electron is captured to fill it, it will participate in a covalent bond not identical to the bulk of the pure crystal, being slightly less firmly attached than a typical valence electron. In Figure 2.3 is shown the p-doped silicon with boron atoms.

These impurity atoms are referred to as *acceptors* and also create localized levels in the forbidden gap (E_A in Figure 2.2), which now lie near the top of the valence band. The number of holes is completely dominated by the concentration of acceptors and this decreases the equilibrium number of conduction electrons. In an extrinsic p-type semiconductor, the holes are the *majority carriers* and dominate the electrical conductivity.

A schematic representation of the energy bands of intrinsic and extrinsic semiconductors can be seen in Figure 2.4.
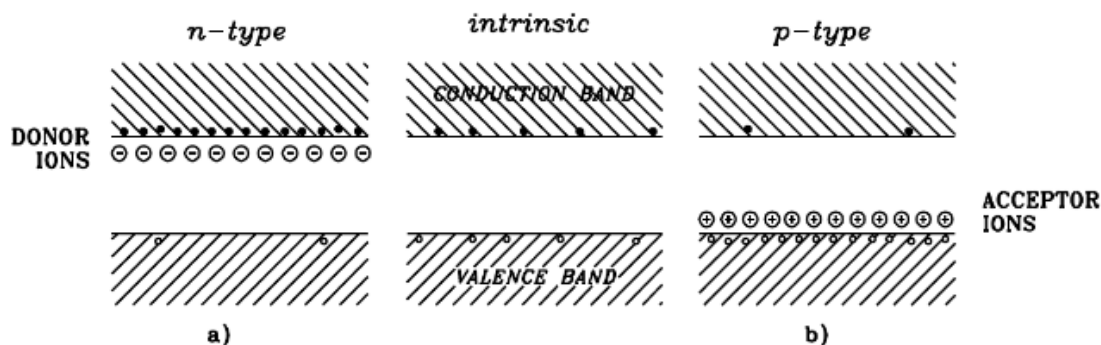
Figure 2.4: Energy band structure of an extrinsic n-type (a), p-type semiconductor (b) [20].

2.1.4   Charge Carriers Transport

The probability of thermally generated electron-hole pair depends critically on the temperature and the E_g. Materials with large band gap operated at low temperature will show very low conductivity due to a low probability of thermal excitation.

The thermally generated electrons and holes take part in a thermal motion which results in their diffusion away from the point of origin. In the absence of an electric field, the electron-hole pairs recombine and an equilibrium is established.

If an electric field E is applied, both electrons and holes undergo a net migration, which is a combination of the random thermal velocity and the drift velocity parallel to the direction of the applied electric field. At low-to-moderate values of E, the drift velocity is proportional to the applied field through the mobility of the carriers $(\mu_{h/e})$. Considering that in semiconductors the mobility of an electron and a hole are roughly of the same order, the velocity $(v_{h/e})$ of the carriers is $v_{h/e} = \mu_{h/e}E$. At higher electric field values, the drift velocity increases more slowly with the field and reaches a saturation velocity independent from the electric field. These saturated velocities are of the order of 10^7 cm/s, therefore time required to collect the carriers over typical dimensions of 0.1 cm will be under 10 ns [22]. For this reason, semiconductor detectors can be among the fastest-responding of all radiation detector types.

2.2   The p-n junction

2.2.1   The p-n junction in Thermal Equilibrium

A p-n junction is the most important structure in semiconductor-based detectors. It is obtained by joining together a n-type and p-type semiconductors. At thermal equilibrium, without applying any bias voltage, the carrier concentrations and the charge density in the junction area are shown in Figure 2.5. In figure, the gray regions are

neutral charged regions, while the light red and blue zone are, respectively, positively and negatively charged.
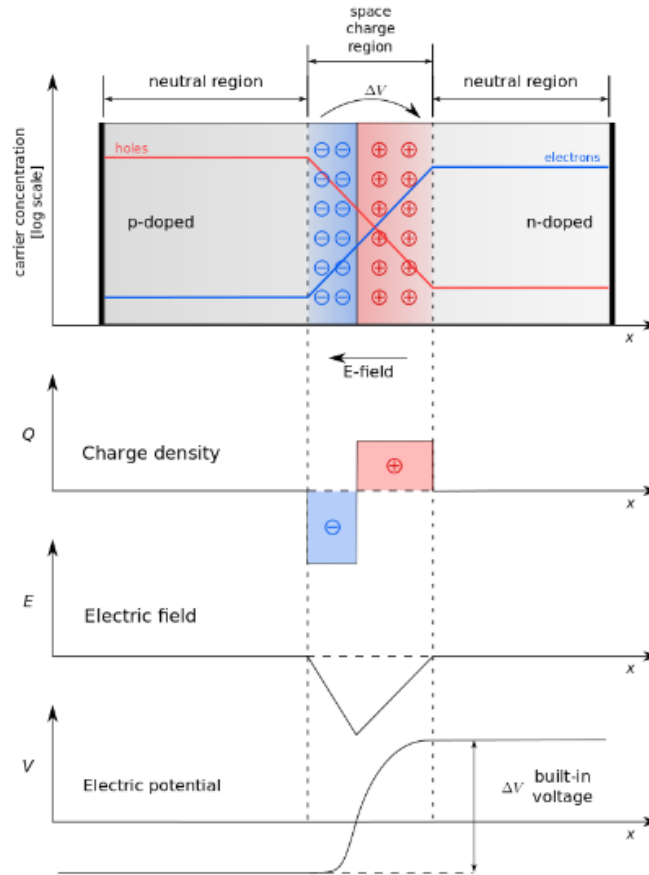
Figure 2.5: A p-n junction in thermal equilibrium with the concentrations for electrons and holes (respectively, blue and red lines). The other plots represent the charge density, the electric field and the potential in the junction area [24].

When the p-type and n-type semiconductor are brought into contact a diffusion movement of charge carriers takes place due to the different concentrations. Electrons move from the n-side to the p-side and, analogously, holes move into the opposite direction. The initial n and p profiles are subsequently altered in the proximity of the p-n junction.

Electrons in the p-side recombine with the holes, as the holes with the electrons in the n-side, in a way that all the free charge carriers vanish. The combined effect is to build up a net negative space charge on the p-side and a positive one on the n-side of the junction. This region, without free charge carriers, is called *space charge region* or *depletion zone*. The region is "depleted" in the sense that the concentration of holes and electrons is greatly suppressed so that the only charges remaining are the immobile

ionized donor sites and the filled acceptor sites. These charges do not contribute to conductivity, thus the depletion region exhibits a very low conduction (high resistivity) compared with the n-type or p-type materials on either side of the junction [22].

The accumulated space charge creates then an electric field which counteracts the diffusion movement and causes charge carriers to be driven in the opposite direction of the diffusion. At equilibrium, a stable depletion zone, without charge carriers, will form at the junction. If the concentration of donors on the n-side and acceptors on the p-side are equal, the depletion region extends in equal distance into the both sides.

The build-up of net charge within the region of the junction leads to the establishment of an electric potential difference (the *contact potential* or *built-in* voltage) which, at equilibrium, nearly amounts to the full band gap value of the semiconductor. The contact potential V_0 can be described with [20]:

$$V_0 = \frac{q}{2\epsilon\epsilon_0}(N_A + N_D)d_n d_p \qquad (2.4)$$

where d_n and d_p are respectively the depth of the depletion zone in the n-side and the p-side, while N_A and N_D are the doping concentrations respectively in the p-side and the n-side.

It is also possible to calculate the depth $d = d_p + d_n$ of the depletion zone, with the condition $N_A d_p = N_D d_n$ so to have equal charges on both sides [20]:

$$d = \sqrt{\frac{2\epsilon\epsilon_0}{q}}\sqrt{\frac{N_A + N_D}{N_A N_D}}\sqrt{V_0} \qquad (2.5)$$

In order to calculate the values in the Equations 2.4 and 2.5, another formula for V_0 is needed since d_p and d_n are unknown. Using the concentration of the charge carriers in an intrinsic semiconductor, n_i, V_0 can also be calculated with [20]:

$$V_0 = \frac{kT}{q}\ln\frac{N_A N_D}{n_i^2} \qquad (2.6)$$

These formulas are based on abrupt changes in the doping profile, which is not given in actual semiconductor devices.

2.2.2   The p-n junction with application of an external voltage

P-n junctions used in radiation detection application are most commonly employed with the application of an external voltage. This because the width of the depletion region can be modified by the application of an external voltage and large depletion regions are necessary for detecting the passage of particles crossing semiconductor-based detectors.

The size of the depletion region with the application of an external voltage can be described by [20]:

$$d = \sqrt{\frac{2\epsilon\epsilon_0}{q}}\sqrt{\frac{N_A + N_D}{N_A N_D}}\sqrt{V_0 - V_{bias}} \qquad (2.7)$$

where V_{bias} is the applied voltage in the forward direction.

In *forward-bias* condition, a positive (negative) bias voltage is applied to the p-side (n-side), the V_0 is reduced and the depletion zone is shrunk or even vanishes. In *reverse-bias* condition, a negative (positive) bias voltage is applied to the p-side (n-side), the V_0 is increased and the depletion zone is enlarged. The two different biasing conditions are shown in Figure 2.6, together with the p-n junction in thermal-equilibrium:

(a) Thermal-equilibrium condition.   (b) Forward-bias condition.   (c) Reverse-bias condition.
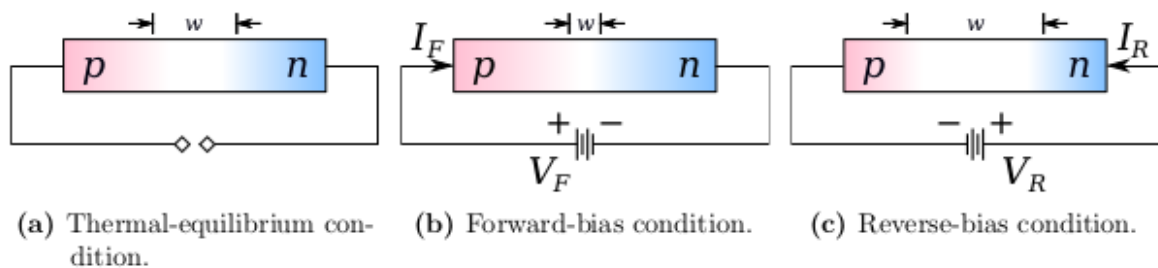
Figure 2.6: Schematic representation of the depletion region width of a p-n junction under the three biasing conditions [15].

A biased p-n junction behaves almost like a diode, allowing the flow of the current mainly in one direction. This can be seen in Figure 2.7: in forward-biased condition, the current increases exponentially with the V_{bias}, while in reverse-biased, a small current can be measured until the breakdown voltage is reached.
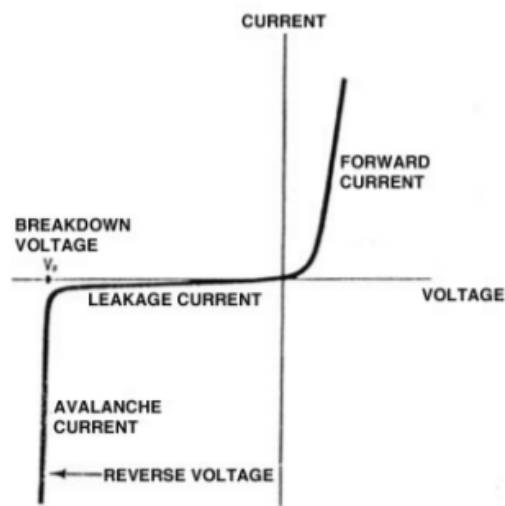
Figure 2.7: The ideal current-voltage IV characteristics of a p-n junction [25].

Fully depleted detectors

The necessary condition to use semiconductor sensors as particle detectors is that the depletion region has to reach through the entire volume of the sensor. *Fully depleted* sensors can be obtained by increasing V_{bias} far enough that the extension of the depletion region reaches the boundary of the sensor's volume.

In particular, the voltage required to achieve the full depletion of a sensor is called *depletion voltage* V_{dep} and depends on the bulk (volume) thickness d_{Bulk} of the sensor, the doping concentration N_D for an n-doped bulk material for example, the permittivity ϵ_0, the electric charge e and the dielectric constant ϵ of the material [20]:

$$V_{dep} \sim \frac{eN_D}{\epsilon\epsilon_0} \frac{d_{Bulk}^2}{2} \tag{2.8}$$

Leakage Current

In reverse-biased p-n junctions, a current, called *leakage current* can be measured. The origins of the leakage current are related both to the bulk volume and the surface of the detector. The surface current usually makes a small contribution as it depends rather on the geometry of the surface than on the applied voltage. This current is more affected by contaminations on the surface or damages caused by scratches.

The main sources of the bulk leakage current are the electron-hole pairs generated by thermal excitation within the depleted (active) volume of the sensor. This current strongly depends also on the absolute temperature T and on the E_g according to [15]:

$$I(T) \propto T^2 \exp\left(\frac{E_g(T)}{2kT}\right) \tag{2.9}$$

To compare currents measured at different temperatures, a scaling law of a current I at a measured T to a current I_R measured at a reference temperature T_R is useful, especially in the case of working with different measuring setups. The scaling law is expressed by [15]:

$$I_R = I \cdot \left(\frac{T_R}{T}\right)^2 \cdot \exp\left[-\frac{E_g}{2k}\left(\frac{1}{T_R} - \frac{1}{T}\right)\right] \tag{2.10}$$

Capacitance

A p-n junction has a capacity consisting of two parts: the junction capacitance C_j and the diffusion capacitance C_d. The C_d is caused by the current through the junction and depends on the current density of the holes j_h and the recombination lifetime of the holes τ_h, but in the case of the sensors investigated in this thesis is negligible.

The C_j is caused by the space charge and is relevant in reverse-biased p-n junctions. Since the depletion region is similar to a dielectric, with the surrounding material compared to conducting plates, C_j can be therefore described like the capacity of a plate

capacitor with the formula [23]:

$$C_j = \frac{\epsilon_0 \epsilon}{d} A \tag{2.11}$$

with A being the surface of the junction.

Since C_j depends on the thickness d of the depletion region, and this latter depends on the applied bias voltage (Equation 2.7), the capacitance can be calculated as a function of the applied bias voltage [26]:

$$C_j = \begin{cases} \sqrt{\frac{\epsilon_0 \epsilon N_D A}{2 V_{bias}}}, & V_{bias} < V_{dep} \\ \frac{\epsilon_0 \epsilon A}{d} & V_{bias} > V_{dep} \end{cases} \tag{2.12}$$

where the thickness d of the depletion region equals the sensor thickness d_{Bulk} when the depletion voltage is reached.

In Figure 2.8 the reverse-squared of the capacitance is shown as a function of the applied voltage: $\frac{1}{C^2}$ increases linearly with the applied voltage as the depletion region grows in depth. When the depletion voltage is reached (69 V in figure), the depletion region does not grow any further and the capacitance assumes a constant-value above the applied voltage. From this plot, the depletion voltage can be calculated from the intersection point of a straight line and a constant line fitted on the data.
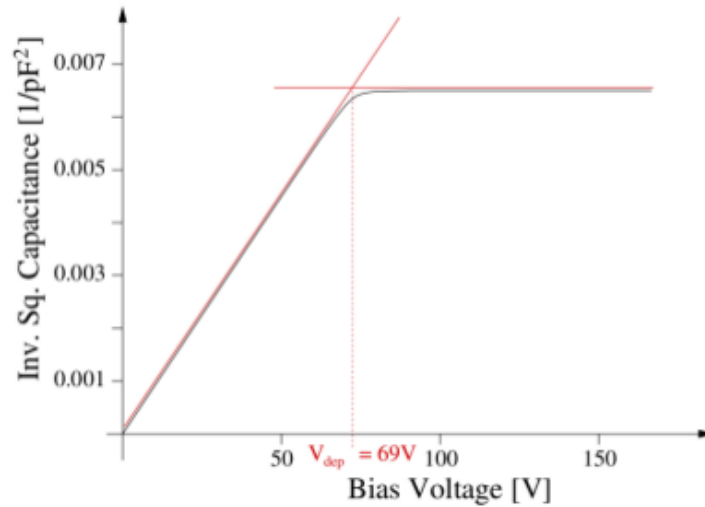
Figure 2.8: Extrapolation of V_{dep} from the capacitance-voltage CV characteristics of a diode [23].

2.3 Semiconductors as Radiation Detectors

Compared with the other radiation detectors based on ionization in gas, semiconductor detectors have unique properties that make them very suitable for the detection of ionizing radiation.

In an intrinsic semiconductor, the small E_g leads to the creation of a larger number of charge carriers per unit energy loss of the ionizing particle to be detected. The average energy for creating an electron-hole pair in semiconductor is $\sim 3.6\,\mathrm{eV}$, one order of magnitude smaller than the ionization energy of gases ($\sim 30\,\mathrm{eV}$) [20].

The high material density of semiconductors leads to a large energy loss per traversed length of the ionizing particle, allowing to build thin detectors that can still produce large signals. On the other hand, the higher material density does not prevent electrons and holes to move almost freely in semiconductors. This leads to a rapid ($\sim 10\,\mathrm{ns}$) charge-collection and makes these detectors really suitable in high-intensity environments.

2.3.1 Ionising Radiation

The interaction of radiation with doped semiconductors causes the creation of electron-hole pairs in the depletion zone. These pairs are then separated because of the drift movement in the direction of the respective electrodes, caused by the applied external electric field. The working principle of semiconductor detectors is to register these electrons and holes as signal and, in order to detect the largest signal-charge, they should be operated in fully depletion. The interaction with ionising radiation is a reversible process which leaves the detector undamaged. It can be distinguished between processes of photons and charged particles.

Photons Their effect in matter highly depends on their energy and on the atomic number of the absorbing material. For low-energy photons, the photoelectric effect is dominant, while high-energy photons usually produce an electron-positron pair in the Coulomb field of the nucleus (pair production effect). For energies in the middle, between $\sim 30\,\mathrm{keV}$ and $5\,\mathrm{MeV}$, the Compoton effect is more common. In silicon, if photons are absorbed through the photoelectric or pair production effect, they release detectable electrons or positrons in the sensor. If they are absorbed via the Compton scattering, the recoiling electrons are detected.

Charged Particles The energy deposition of heavy charged particles in material is explained by the Bethe-Bloch formula [27]. It describes the mean energy loss of charged particle, which is due to many scattering processes with the electrons of the atoms of the absorbing material. Particles with low energies deposit their energy mainly by collision effects, such as excitation or ionization of atoms. Particle with higher energies cause radiation effects, such as bremsstrahlung. In thick material the energy deposition follows a Gaussian distribution but, with decreasing material

thickness, the energy deposition changes into a Landau shape. This means that the mean energy loss is not equal to the most common value. In this thesis, sensor with thickness of about $200\,\mu$m have been investigated, which can be considered as thin materials.

The Energy Deposition Process

The fraction of energy of the ionising particle converted into the electron-hole pair creation is a property of the detector material and it is only weakly dependent on the type and the energy of the radiation, except at very low energies that are comparable with the E_g.

For a given of radiation energy, the mean amount of electron-hole pairs generated in such processes is [25]:

$$N_{e/h} = \frac{E_d}{E_{pair}} \tag{2.13}$$

where E_d is the energy deposited and absorbed in the detector, and E_{pair} is the mean energy spent for creating an electron-hole pair ($\sim 3.6\,$eV for Silicon).

The electron-hole pair production is an almost stochastic process, but it is not independent from pair to pair as the energy deposition occurs in a cascade of energy transfers from the incoming particle to the carriers and from excited carriers to other carriers. This correlation between the different pair production events leads to the use of the Fano factor F in the intrinsic energy resolution of a semiconductor sensor to account for the lower standard deviation value observed with regard to the Poisson predicted standard deviation value [27]:

$$\sigma_{Si} = \sqrt{FN_{e/h}} = \sqrt{F \cdot \frac{E_d}{E_{pair}}} \tag{2.14}$$

For most semiconductors, like silicon and germanium, the Fano factor is significantly below the unity, which explains the good energy resolution of silicon- or germanium-based detectors [20].

The Signal Generation in Silicon Pixel Detectors

Silicon sensors, as radiation detectors, use the depletion zone at the junction as the *active* detection region. Charge carriers, in an un-depleted silicon sensor, recombine after ionisation and return to the equilibrium state, preventing the collection by the respective electrodes and thus the registration of the signal by the read-out electronics. Electron-hole pairs created in the depletion zone, instead, do not recombine and if an external bias voltage is applied, they are drifted towards the electrodes, where they can induce the signal.

Silicon detectors are usually built with highly asymmetric p-n junctions, consisting of highly doped surfaces and a low doping concentration in the bulk. The bulk can be either a p- or a n-type. The signal process generation can be seen in Figure 2.9, where pixel detectors (described in Chapter 3) are represented. Figures 2.9a and 2.9b show the situation of a n^+-in-n sensor, where the n^+ implantation represents the pixel implantation (front-side of the sensor) while the p^+ implantation is the backside. In this configuration, when negative bias voltage is applied on the backside, the depletion region grows from the p^+ implantation side. Since the read-out system is connected to the pixel-side, a full depletion of the sensor is needed in order to detect the largest possible signal created by the passage of an ionising particle (2.9b).
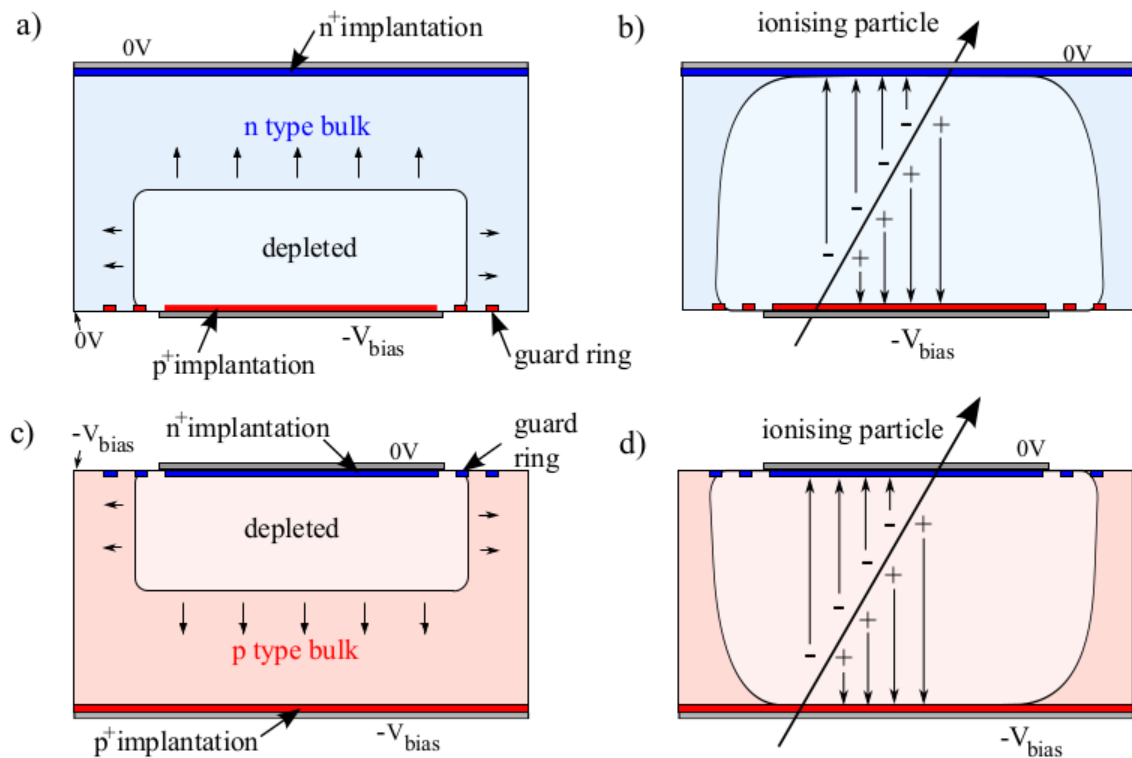
Figure 2.9: Growth of the depletion region and ionisation in depleted n-bulk (a,b) and p-bulk (c,d) diodes [28].

With p-type bulk the situation is represented in Figure 2.9c and 2.9d. In n^+-in-p sensors the depletion zone grows from the front-side and this allows the detection without full depletion of the sensor. However, full depletion is still desired since larger depletion zone means more electron-hole pairs and thereby increased signal strength.

2.3.2 Radiation Damage in Silicon

Although irradiated sensors have not been investigated in this thesis, it is worth to explain some of the effects caused by the interaction of a non-ionising radiation with the lattice atoms of the crystal. This process is a non-reversible process which results in the creation of crystal imperfections that can change irreversibly the material. Radiation damage on silicon is usually divided into *bulk* and *surface* damages.

Bulk Damage

Bulk defects are caused by the interaction of the incident particles with the nuclei of the lattice atoms. It can produce the displacement of them out of their lattice positions, resulting in crystal imperfections which may be electrically active and change the electric properties of the material.

The removal of a silicon atom (the **P**rimary **K**nock on **A**tom, PKA) creates a vacancy (V) in the left lattice position and an interstitial (I) in the position where now the displaced atom is. This process cause the formation of a Frenkel pair V-I, or *Frenkel defect*. For example, to remove a silicon atom, a minimum recoil energy of about 25 eV is required [29].
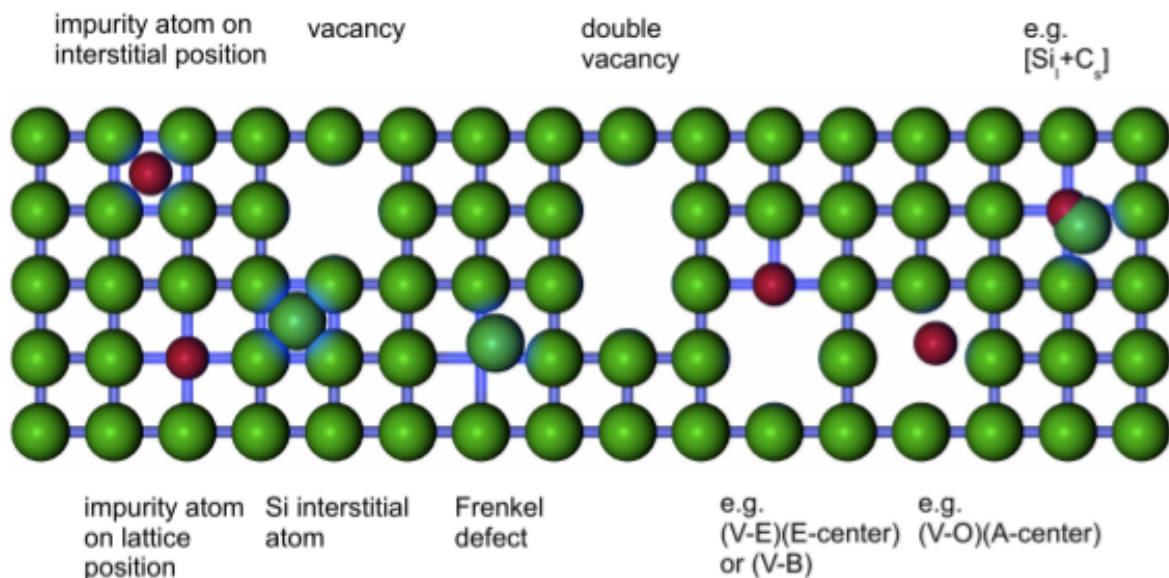
Figure 2.10: Schematic illustration showing different crystal defects [23].

The probability to produce a PKA depends on the kind and the energy of the imping-ing particle. Gamma rays, neutrons or electrons with energy of a few MeV or less create only *point defects*, whereas heavy charged particles like protons or pions of equivalent

energy are generally more damaging since they also interact electromagnetically. They form the so-called *cluster defects*, a large number of point defects, along the track of a PKA.

To be able to compare the damage caused by different types of particles at different energies, the radiation damage is scaled with the so-called **N**on-**I**onizing-**E**nergy-**L**oss (NIEL)-hypothesis, valid as long as the defects consists of point or cluster defects. It normalises the effect of the tested radiation to a "standard radiation" which is usually referred to as 1 MeV-neutrons. However, only the interaction with the first hit atom depends on the kind of the impinging radiation, while further damages are caused by the PKA.
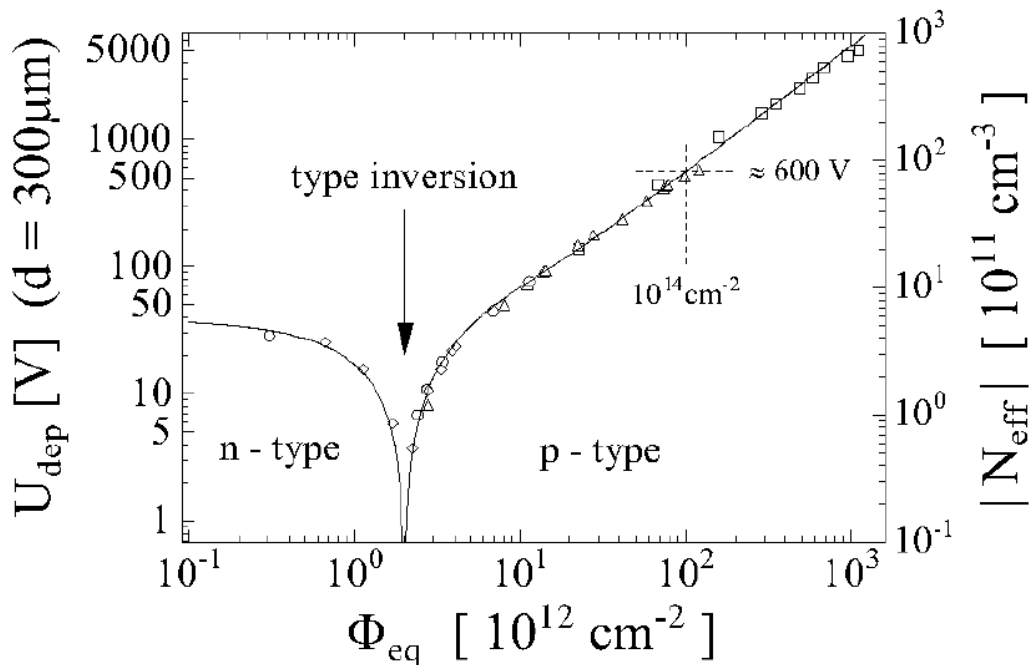
Figure 2.11: Change of the full depletion voltage of a 300 μm thick silicon sensor and its absolute effective doping versus the normalized fluence, immediately after the irradiation [29].

Bulk damages have consequences on the operation of irradiated sensors. Point defects create energy levels in the band gap, which act as *generation-recombination* centres that can emit or catch electrons (or holes). Altering the emission of the charge carriers in the space charge region, the reverse-bias leakage current increases which, together with the increasing of operation voltage, leads to an increased power dissipation heating the sensor. Also the effective doping concentration changes with irradiation, as the point defects can be charged. The fluence dependence of the effective doping concentration and of the full depletion voltage are plotted in Figure 2.11. Starting with a n-doped

material, the absolute effective doping concentration decreases up to a certain fluence at which the bulk material becomes almost intrinsic, to then increases again with further irradiation. The material behaves now like a p-material and for this reason the effect is known as *type-inversion*.

Surface effects

The surface properties of a silicon crystal can also be permanently changed with irradiation. The surface is characterized by the abrupt termination of the periodic lattice structure since silicon atoms have no covalent bonds to neighbouring ones there. These so-called *dangling bonds* make the atoms chemically and electrically active.

In order to overcome this problem, the surface of the wafer is usually passivated by a silicon dioxide (SiO_2) film which is thermally grown. The passage of a radiation can cause the build-up of permanent charges in the SiO_2 layer. As the crystal structure of this layer is highly irregular, displacement of single atoms due to irradiation do not lead to macroscopic changes but cause changes of the interface properties. After the creation of an electron-hole pair in the oxide layer, most pairs recombine immediately. Electrons have much more larger mobility than holes in the oxide ($\mu_{e,oxide} \approx 20\,cm^2/Vs$, $\mu_{h,oxide} \approx 2 \cdot 10^{-5}\,cm^2/V$) therefore are collected by any positively biased electrode close by [29]. The holes have instead lower mobility because of the existence of a large number of deep traps in the transition region between the Si/SiO_2 that can capture and keep them permanently. The trapping centres are also a problem in the bulk. Their presence in the depletion region can cause the reduction of the signal height, if they hold part of the signal charge for a time longer than the charge-collection time.

The Si/SiO_2 interface hosts electronic states whose number and properties are altered by ionising irradiation. These interface states lead to an increased reverse-bias current after irradiation, which adds to the leakage current caused by defects in the bulk. However, surface damage has no direct consequences for the operation of the particle sensors. The design has to be adjusted in a way that the changes in the electric field due to the oxide charges do not influence the sensor performance. One important aspect in this sense is the design of the guard rings structure in the sensor and will be discussed in Section 3.3.

Chapter 3

The ATLAS Pixel Detector

As already described in Section 2.3, the detection of particles using silicon sensors is based on the creation of charge carriers in the depletion region of a p-n junction which gives the signal. The signal then needs to be amplified and digitized by specialized read-out circuits. In this chapter, after a brief overview on the current technologies of pixel detectors, the focus is concentrated in explaining the design, functionality and operation of the ATLAS pixel detector. The layout of the sensors analysed in this thesis is also presented as well as the guard rings structure properties.

3.1 Sensors Technologies

3.1.1 The Hybrid Pixel Design

Pixel semiconductor detectors are usually defined *hybrid* in the sense that the pixel sensor and the read-out matrix are separately fabricated and then mated together via special techniques called *bump bonding* (see Figure 3.1). This is done using the so-called *bump bond balls* (shown in Figure 3.2), which are distributed between the pixel and the read-out matrix, flipped and positioned between each sensor and read-out chip (*flip-chip* process). In particular, the connection is established by heating the solder balls, in a process that requires the highest precision. To ease this, alignment marks are usually implemented on the sensor surface.

A single sensor chip connected to a single chip of the read-out via bump bond is called *assembly* or *module*. Afterwards, the connection of a module to the outside world is realized in the detector by flexible **P**rinted **C**ircuit **B**oards (PCBs), which host and route the signal, and supply lines, with low material costs. Rigid PCBs are used therefore for measurement in the laboratory and beam tests.

The innermost sub-detector of the ATLAS experiments demands the implementation of a silicon pixel system in order to cope with the high collision rates and the resulting

radiation damage, as well as the need to achieve high resolution and fast read-out times. For this reason, a *hybrid pixel detector* is implemented for the innermost tracking layers.
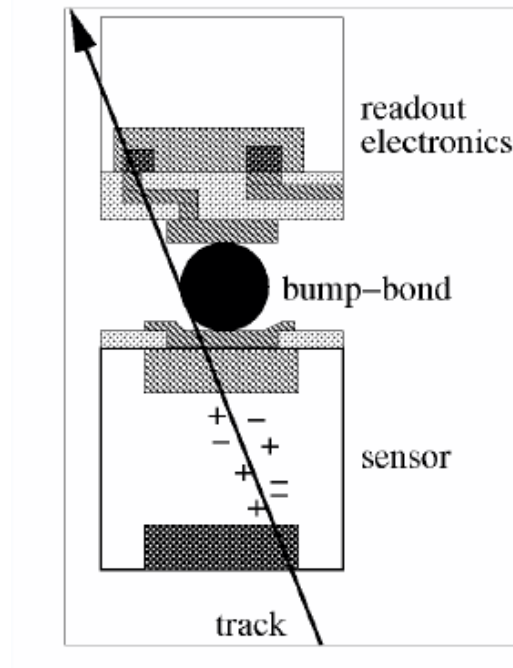
Figure 3.1: Sketch not in scale of the cross section of a hybrid pixel detectors, showing one connection between sensor and the electronics together with a particle track releasing ionisation in the sensor volume [29].
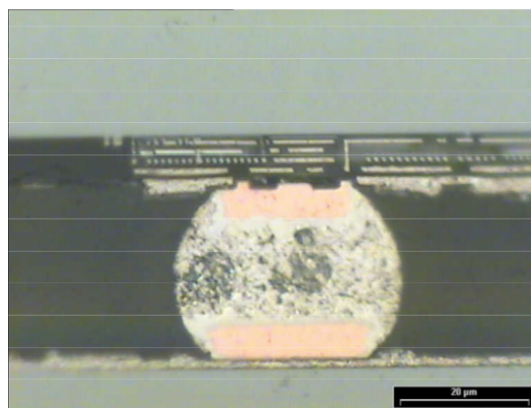
Figure 3.2: Cross section of a solder bump connecting pixel sensor to front-end electronics [29].

3.1.2 Planar Silicon Sensors

Hybrid pixel detectors can be made of planar pixel sensors. A planar pixel silicon sensor is produced on a silicon *wafer* (a thin slice of semiconductor) which consists of a slightly n- or p-doped bulk material while the surfaces are highly doped (as the example in Figure 2.9). The front-side is highly doped with n^+ or p^+ implantations, forming an array of small rectangular pixel diodes. The back-side is instead usually created with a dopant opposite to the pixels side. Bias voltage is applied between the two opposite sides of the sensor in order to deplete it and create an electric field in the bulk, allowing the drift of the charge carriers generated by the passage of an ionizing particle. The carrier cloud generated is localized in a small region around the particle track, which allows to measure the position in the sensor using the signal induced on the individual pixel. A guard ring structure is disposed in order to ensure a smooth transition of the surface bias potential, from the active area to the edge of the sensor. Each concentric ring is self-biased, with the inner guard ring taking the pixel electrode potential, or the high voltage in the back-side, and the outermost one taking the edge potential.

Planar silicon sensors can be used in four different configurations (shown in Figure 3.3) of pixel implant and bulk type. For example, in the n^+-in-p configuration, the n^+ describes the pixel implant type and p is the bulk material.

(a) n-in-n sensor

(b) p-in-n sensor

(c) n-in-p sensor

(d) p-in-p sensor
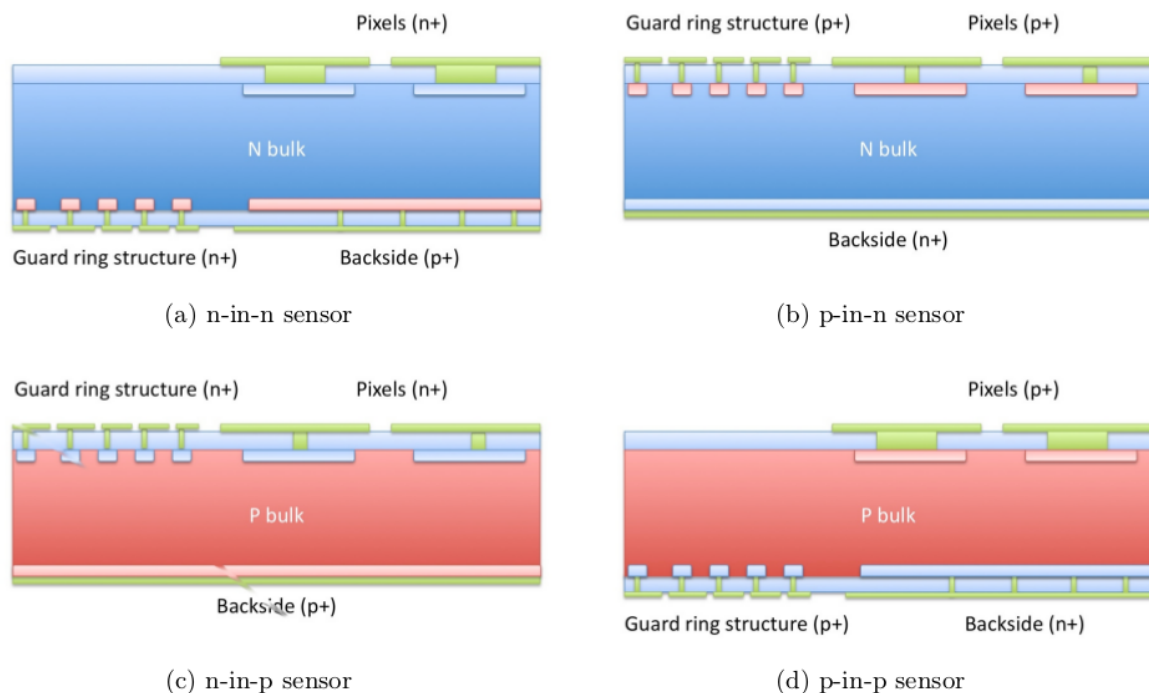
Figure 3.3: Schematics of the possible pixel sensor implant and bulk configurations [25].

Historically, n-type bulks have been used because of their most developed technology with respect to p-type bulk. The two possible n-type bulk configurations are shown in Figure 3.3a and Figure 3.3b. They have different doping type of the pixel implantations, respectively n^+ and p^+. For n^+-in-n sensors (Figure 3.3a), the depletion zone starts at the back-side and grows towards the pixel side, while for p^+-in-n type (Figure 3.3b), the depletion zone begins on the pixel side and extends towards the back-side with higher bias voltage. The same happens with the two configurations using the p-type bulk: in n^+-in-p sensors (Figure 3.3c) the depletion zone grows from the pixel side towards the back-side, while in p^+-in-p (Figure 3.3d), it grows from the back-side towards the pixel side. The guard ring structure must be placed on the side from which the electric field starts to grow, when a bias voltage is applied between the two sides of the sensor. Therefore, they are placed on the back-side for n^+-in-n (or p^+-in-p) and on the pixel side for n^+-in-p (or p^+-in-n) sensor types. In this way, they fulfil their role preventing the extension of the electric field over the sensor edges.

The choice of the pixel implantation type, n^+-type or p^+ type, is driven by the selection of the main-carriers signal in the sensor. The n^+-type implantations collect electrons while the p^+-type one read out the hole signal. Therefore, n-type implantations are usually preferred over p-type because of the higher mobility of electrons in silicon with respect to holes (see Section 2.1.2), and also because electrons are less prone than holes to eventual traps existing in the bulk, which affects the collection of the signal.

Another aspect to be considered is that, since each surface of the sensor needs to be realized with a particular process (the *photo-lithography* method), it appears clear that, in the case of Figure 3.3a for n^+-in-n sensors and Figure 3.3d for p^+-in-p sensors, the sensor needs to be processed from both the back- and front-side. This so-called *double-sided* process of the sensor is more expensive than a *single-sided* process, which can be done when the guard ring structure is located on the pixels side (Figure 3.3b and Figure 3.3c). On the other hand, if the guard ring structure is located on the front-side, some high voltage coming from the back-side can be also present in the guard ring region and therefore reach the front-side, which might be detrimental to the read-out chip connected to the pixel implantations.

As explained in section 2.3.2, the n-type bulk can invert into a p-type after irradiation. Figure 2.11 shows that, before the bulk-inversion, the depletion voltage is decreased from the initial value, while after, it raises again due to the Space Charge Sign Inversion (SCSI). In the case of a n^+-in-n sensor, the SCSI is actually beneficial since the electric field, after type inversion, grows from the pixel side, which is connected to the read-out, therefore even if the sensor bulk is not fully depleted, charge is collected at the read-out. This is not the case of the p^+-in-n where, after the SCSI, the electric field grows from the back-side towards the front-side, therefore if the sensor is not fully depleted, no charge can be collected at the read-out.

The development of the p-type bulk represents a promising technology for the pixel sensors. The configuration n^+-in-p (Figure 3.3c) has the advantage of being realized in a

single-sided process and of collecting the electrons signal even if not fully depleted, since the electric field grows from the front-side towards the back-side. Instead, the p^+-in-p configuration (Figure 3.3d) is not really used since it does not have advantages over the other configurations.

The current ATLAS planar pixel sensors are made of n^+-in-n sensors but the possibility of the n^+-in-p sensors has been considered for the new ITk [31].

3.1.3   3D Silicon Sensors

Hybrid pixel detectors can also be made of sensors with 3D technology. The main difference between planar and 3D structures is the orientation of the electrode implants in the sensor (see Figure 3.4). With chemical etching techniques, deep holes are created in the sensor while implants are created on the surface of the holes, forming p-type and n-type columns in the sensor. These holes are then filled with a conductive material to form the anodes and the cathodes. The bias voltage is applied between the two column types and the carriers drift then laterally. The lateral bias scheme avoids the problem of high voltage distribution at the edges of the planar sensors and thus reduces the inactive edges.

For sensors with a pixel pitch smaller than the wafer thickness, it is possible to obtain faster signals and lower depletion voltages. Also, because of the short drift distances of the carriers, the loss probability of the carriers-induced signal due to trapping is reduced, making the 3D design more radiation hard than the planar one. For this reason, they represents the baseline option for the innermost layer (Layer 0) of the ITk Pixel Detector, and a possible alternative for Layer 1 [16].
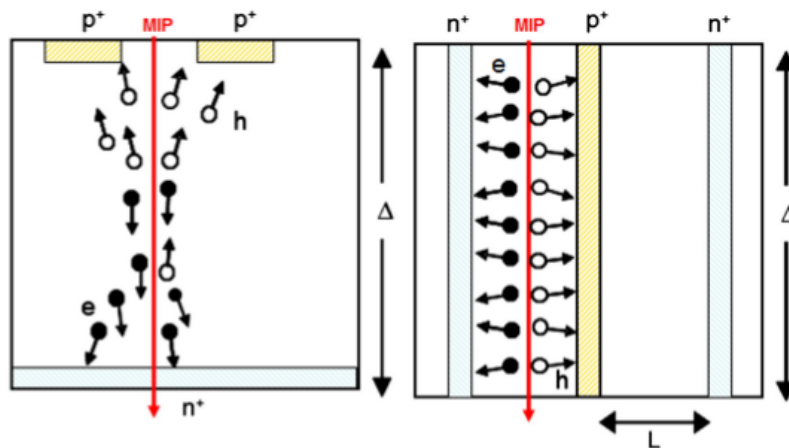
Figure 3.4: Schematic cross section of the p^+-in-p planar sensor (left image), compared with the 3D sensor (right image), emphasizing the decoupling of active thickness (Δ) and the collection distance (L) for the 3D sensor [15].

3.2 The ATLAS Pixel Design

3.2.1 The Standard Sensor Design

The ATLAS pixel detector of the ID consists of planar n^+-in-n and 3D silicon sensors. In this thesis only the planar sensors have been investigated and their structure is explained in this section.

A schematic cross section of a planar n^+-in-n sensor is shown in Figure 3.5. A high-resistivity, lightly n-doped wafer is used as bulk material. The sensor is processed from both sides (double-sided process) which ensures radiation hardness, despite of the additional fabrication costs. On the front-side, the pixel matrix is formed by n^+ implantations while on the back-side one large p^+ implant is installed covered by the HV pad for the application of the bias voltage.
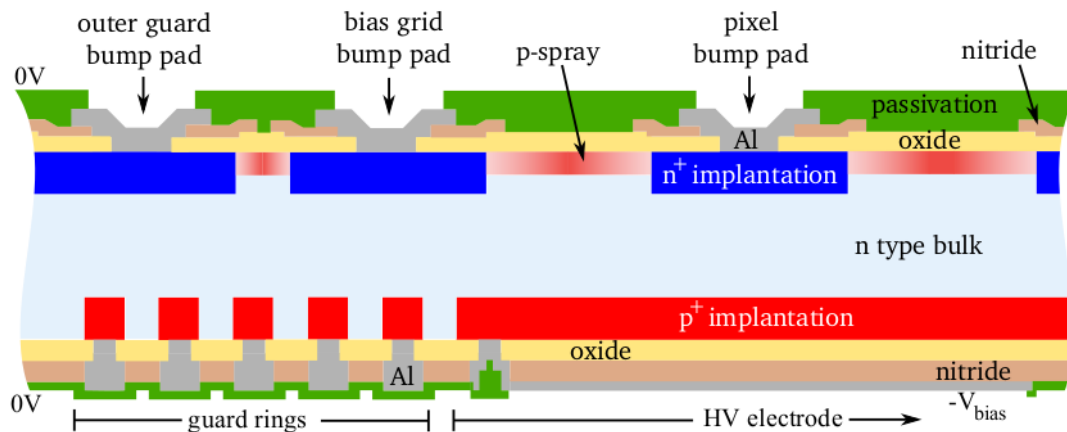
Figure 3.5: Schematic cross section of the ATLAS pixel sensor with the dimensions not in scale [15].

Each surface of the sensor consists of five layers which require different masks during the photo-lithography process. To the n-type core the following coatings are applied, from the inside to the outside:

1. the n^+/p^+-implantation

2. the oxide passivation

3. the inner nitride passivation

4. the metal (AlSi alloy)

5. the outer nitride passivation

The last layer of passivation, present on the front-side, is punctuated by openings which allow the connection to the **F**ront-**E**nd **I4** (FE-I4) to read-out every pixel. This connection point on the sensor is called *bump pad*.

Since it is possible to have a conductive channel between two pixel implantations, because of the formation of oxide charges, a *p-spray* doping is applied between them for insulation. This is usually done between the steps 3 and 4. The p-spray concentration has to be higher than the low doping of the bulk substrate but significantly lower than the n^+ implantations. In particular, the so-called *moderated p-spray* is used in the ATLAS pixel sensor design, which is shown in Figure 3.5 by a red color gradient: the p-doping is spread homogeneously over the complete wafer surface, and the strength of the doping is moderated by the nitride layer which is already existent. The full dose is placed in those regions without nitride and a reduced dose in those regions with the nitride. The effective doping profile results in a smooth distribution without high field intensities next to the pixel implantations.

The sensitive area of the sensor is defined where the n^+ implantations on the front-side are located. They are surrounded by two guard rings, which represent the inactive edge of the sensor: the *bias grid* ring and the *outer* ring (visible in Figure 3.5). The bias grid is implemented in order to have the possibility to test the sensor before the bump bonding with the read-out chip and is also used to keep all the pixel implants at the same potential. This mechanism is illustrated in Figure 3.6.
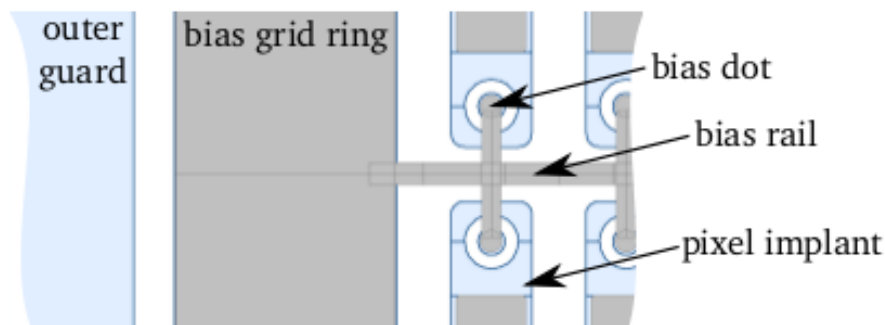
Figure 3.6: Top view of the bias grid of the ATLAS pixel sensor. The n^+ implantation is blue, the metal grey [28].

The bias grid, implemented on the pixel side, runs between every double column and each pixel is connected to it through a *bias dot*, which is a circular implantation inside the pixel implantation. A metal *bias rail* connects the bias dot and the bias grid ring. The *punch-through effect* that takes place between the bias dot and the pixel implantation takes all the pixels on the same potential [28].

The IBL Planar Pixel Design

As shown in Figure 1.4, the innermost layer of the ATLAS ID is the IBL. The pixel cells of planar n^+-in-n sensors of the IBL design, have a pitch of $250\,\mu$m in the long and $50\,\mu$m in the short direction. Their design is shown in Figure 3.7. The rectangular n^+-implantation (blue in the figure) is positioned centrally with rounded corners to avoid maxima in electric field strength. It is surrounded by openings in the nitride layer, which are used for the moderated p-spray technique and are represented in green. The opening in the outer passivation layer for the subsequent bump bond deposition is on the right represented in orange, while the bias dot, with the connection to the bias grid, is on the left. In between there are three openings in the inner passivations which ensure a conductive connection from the n^+ implantation through the metal (gray) layer to the bump bond.
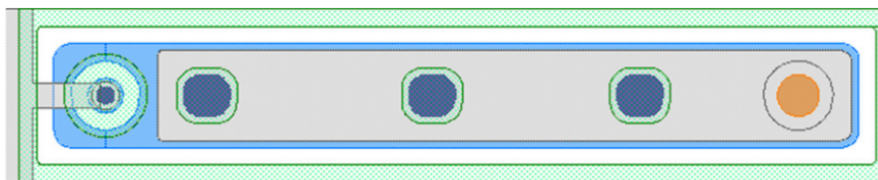
Figure 3.7: Schematic layout of the IBL planar pixel design [32].

The IBL planar pixel design is described in details in [28]. It was adopted from the original design of the ATLAS planar pixel sensors with the intention of reducing the inactive areas since the availability space didn't allow an overlapping of the sensors. Inactive areas are necessary to decrease the high voltage at the cutting edge. Investigations on how much reduction is compatible with a reliable sensor operation were performed [28].

Figure 3.8 shows a comparison between the edge designs of the ATLAS pixel sensor and the IBL. The first is shown in Figure 3.8a. It has 16 guard rings covering a width of about $600\,\mu$m, while $500\,\mu$m are left as safety margin. The overall inactive edge is of $\sim 1100\,\mu$m between the edge pixels and the cutting edge. The IBL "conservative" design is shown in Figure 3.8b. The inactive edge distance between the pixel matrix and the cutting edge shrinks to below $450\,\mu$m and the number of guard rings are decreased to 13, reducing also the safety margin to $\sim 90\,\mu$m. Figure 3.8c shows the current slim edge IBL design, in which the inactive edge is further reduced, extending to $500\,\mu$m length the edge pixels, so that one half of them is placed opposite to the guard rings. This configuration is only possible for the n^+-in- sensors as the guard rings and the pixels are placed in opposite sides of the wafer.

Because of the offset between the high voltage pad and the edge pixel, an inhomogeneous electric field is expected in the region of the pixel overlap. This results in a non-uniform development of the depletion zone and thus in a lower but still sufficient

efficiency of the pixels edge [28].
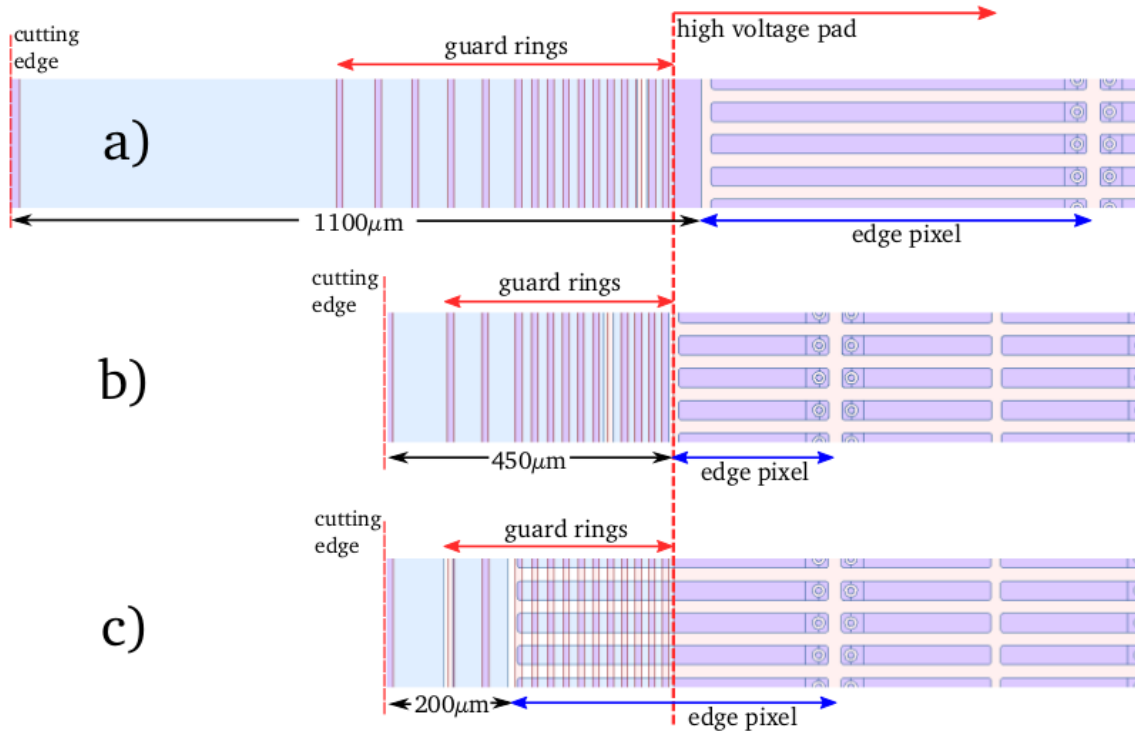
Figure 3.8: Top view of the sensor edge region of the standard ATLAS pixel sensor (a), the conservative (b) and the slim edge (c) IBL design. The n^+ implantation is seen in blue, the p^+ implantation is in red [28].

3.2.2 The modified Pixel Implantations

Based on the IBL pixel design seen in Section 3.2.1, six modified pixel designs were developed in Dortmund [28]. With these modified designs the electric field strength should be increased and higher efficiencies should be reached at lower voltages, which results in better performance of the sensor at lower voltages.

They are numbered from V1 to V6 and their layouts can be seen in Figure 3.9. With the same color code: the n^+ implantation is blue, the metal in grey, the nitride openings in green and the bump pad opening (the opening in the outer passivation) in orange. In both V1 and V4, the n^+ implantation is divided into four segments but with different corners, rounded for V1 and sharper for V4. The moderated p-spray profile is continued between the individual segments. The V2 and V3 pixels feature sub-divisions to ten and 16 segments, respectively, and they both have rounded corners. Due to reduced space between the single segments, no moderated p-spray profile could be implemented. V5

and V6 have the n$^+$ implantation narrowed by a factor of three. The difference between the two is that V6 has the same moderated p-spray profile as the standard design while this is changed in V5. The width of the high dose area is also largely increased. All designs have an identical bias dot and bias grid structure.
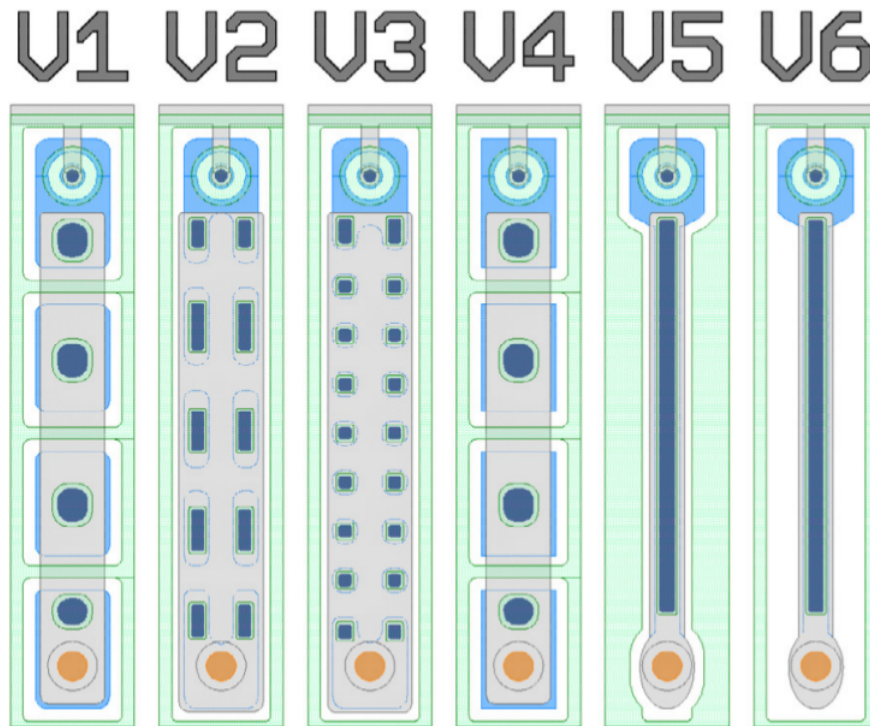
Figure 3.9: Schematic layout of the modified designs V1 to V6 [32].

The six pixel designs together with two standard IBL designs, named V0 and 05, are placed on the same sensor called REINER[1]. Figure 3.10a shows the p-side of the sensor, while Figure 3.10b shows the n-side with the pixels matrix. The sensor consists of 26880 pixels distributed in 80 columns and 336 rows, and it has a bulk thickness of 200 μm.

The pixels have a size of 250 μm × 50 μm, while only the first and last column have longer pixels of 500 μm × 50 μm size. After ten columns, the pixel design changes thus eight structures are located on the REINER sensor, with one structure consisting in 10 columns and 336 rows of the same pixel design. The pixels on the n-side are continuous, while the p-side is divided by 13 guard rings into the eight structure of special pixel design. The pixel design name is printed centrally for each pixel design on the p-side, and high voltage pads for contacting are located at the top and bottom, in a way that each structure can be individually powered. In Figure 3.11 a detailed view of the guard

---

[1]**RE**designed **IN**novative **E**xciting and **R**ecognizable.

ring layout between two designs is shown, where it can be noted that the next-to-last column of pixels is fully shifted beneath the guard rings.

(a)   (b)
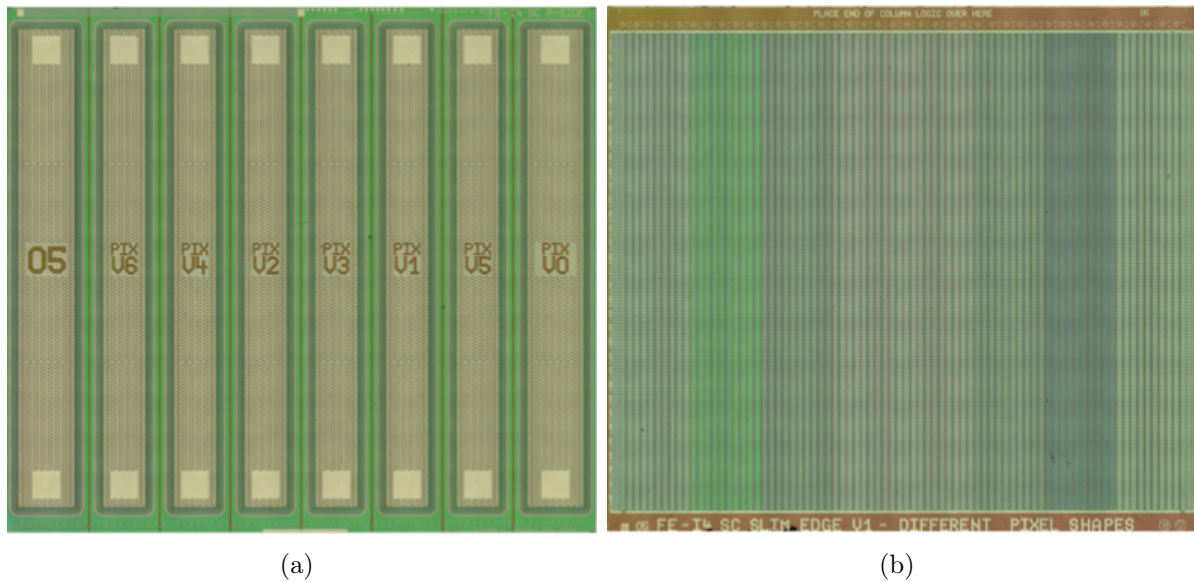
Figure 3.10: Microscope images of the p-side (a) and n-side (b) of the REINER sensor.
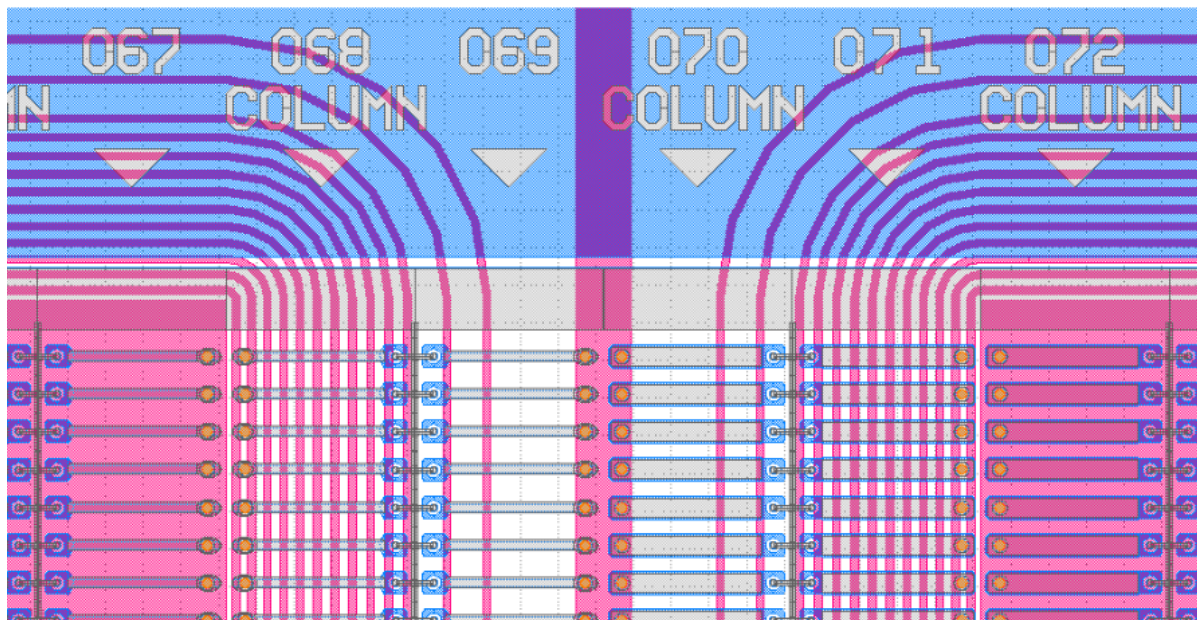
Figure 3.11: Guard ring layout between two designs. The two outermost pixel columns of each structure are located under the guard rings.

3.2.3 Front-End and Assembly

To read out the analog signals from the pixels, a read-out system is necessary. The integrated circuit of *Front-End* (FE) is built with individual cells matching the pixels, so that they are coupled together using bump-bonding techniques, as already described in general for the hybrid design. In this way, each pixel channel is then individually read in a digital format to obtain the position and energy of the crossing particle. For the connection via bump bonds, the ATLAS pixel production uses two different techniques, the tin-silver bumps and the indium bumps. More details about these techniques can be found in [29]. Before the actual bump bond process, the pads of the sensor and the chip have to be prepared with additional metal layers, the under bump metal (UBM).

Each FE pixel cell features an analogue and a digital part. The charge coming from the sensor is amplified by a pre-amplifier and then its output is digitized by a discriminator which convert it into a **T**ime-**o**ver-**Threshold** (ToT). The ToT is thus a measure of the amount of charge.

The ATLAS FE read-out chips are shown in Figure 3.12.
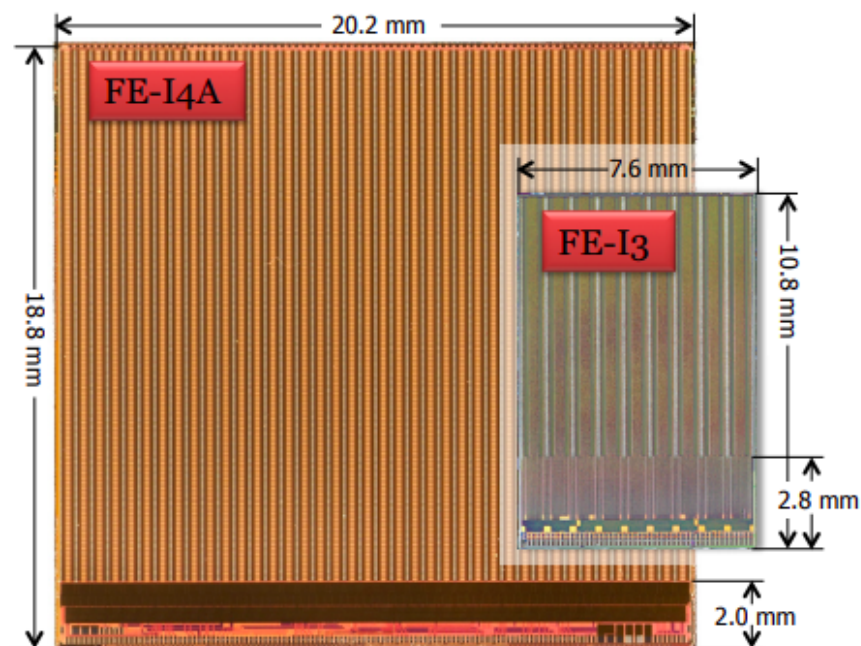
Figure 3.12: Picture of the FE-I4A in comparison with the FE-I3 [33].

The FE-I3 read-out chip was developed in 2003 and used for the three original barrel layers and end caps of the ATLAS pixel detectors. It features 2880 pixel cells, arranged in 18 columns with $400\,\mu$m pitch and 160 rows with $50\,\mu$m pitch. The FE-I4 is the

successor of the FE-I3 and was fabricated in 2010 for the IBL [33]. It offers a much larger size while the inactive area is reduced. The chip is arranged in a matrix of 26880 pixels, divided into 80 columns with 250 μm pitch and 336 rows with 50 μm pitch.

In order to test the performance and the efficiency of the sensor chip assemblies, in lab or beam test setups, they are mounted on and connected via wire bonds to the *read-out cards*, which provide connection for high and low voltage, and data transfer. The read-out card for the REINER sensors allow to power different designs separately via jumpers. This can be seen in Figure 3.13.
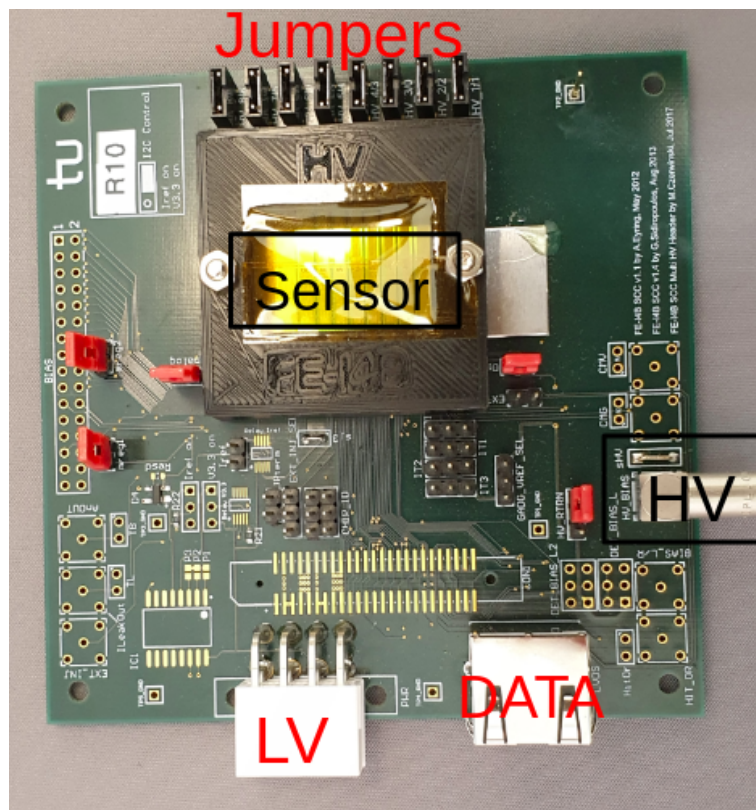
Figure 3.13: Sensor assembly on PCB listed in Table 4.1.

3.3 The Multi-Guard Rings Structure

The main goal of introducing a guard ring structure into the design of fully depleted silicon detectors is to stabilize their long-term behaviour. It has been known that the presence of the guard rings improves the performance of silicon detectors, in particular the breakdown voltage, reduces the leakage current and improves their spectroscopic response [34, 35].

The role of the guard ring structure near the high-voltage electrode, or the pixel matrix of the silicon sensor described, is to ensure a smooth transition from the high voltage to the ground, while approaching the outer edge of the device. The edge termination is always a critical issue for the long-term stability of silicon detectors since it depends very much on the potential of the sensor surface. After some time, the edge usually takes the same potential as the back-side of the sensor, independently from its configuration, because the cutting edge is conductive due to the mechanical damages caused by the cutting procedure. Each guard ring acquires its bias voltage by the punch-through mechanism and the potential drop between them can be influenced by their spacing and the metal overlap. If a uniform potential drop between the rings is aimed for, the spacing has to increase from the inner to the outer regions [29].

The number of the guard rings depends on the maximal bias voltage targeted. A reliable edge termination can be also reached with only two guard rings, one very close to the edge on backside potential and one very close to the sensitive region on ground. However, with *multi-guard ring* structure a breakdown voltage in the keV region can be reached [29].

In the ATLAS pixel sensor design the number of guard rings is 16, with an implant width of $10\,\mu$m. Guard rings represent a dead zone in the pixel sensors since no particle can be detected close to the structure (Figure 3.14). The presence of these inactive zones surrounding the sensor force their overlapping in the ATLAS ID to avoid detection gap between sensors. On the other hand, this overlap increases the amount

Figure 3.14: Corner view of a n$^+$-in-p pixel sensor structure showing the guard ring structure and the first 3 columns and 18 rows of the pixel matrix.

of material present in the tracker. This should be avoided to reduce material budget in the ID and to increase the simplicity of its configuration. Simulations to evaluate the effects of modifying the number of guard rings and their spacing factors to reduce the dead zone while maintaining adequate operation conditions for the sensor were performed [36]. Also the effect of radiation damage on the efficiency of the guard ring structure was studied.

As shown in Figure 3.8, the reduction of the guard rings area for the sensors to be used in the IBL was the key in minimizing the inactive zones and the material budget. This was done by shifting the pixels under the guard rings area. In particular, the shift, in the case of the "Slim-Edge" IBL candidate, is $250\,\mu$m, while for the "conservative" candidate (Figure 3.8b) is $100\,\mu$m [25].

Figure 3.15 shows the electric field magnitude in the region of the edge pixel where the overlap occurs, for a shift of $1001\,\mu$m (a) and $200\,\mu$m (b). The presence of the guard

rings affects the distribution of the field under the pixel and the field is weaker in the section of the pixel overlapping the guard ring.
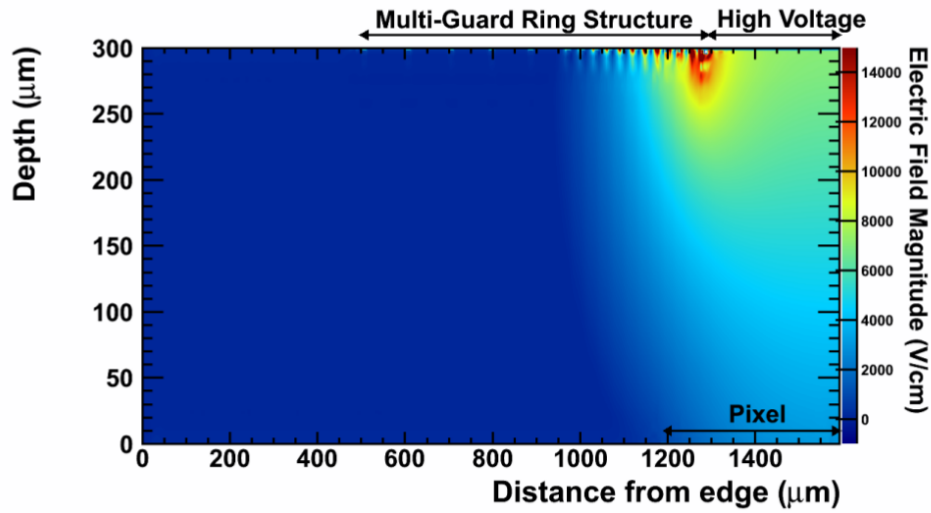
(a)
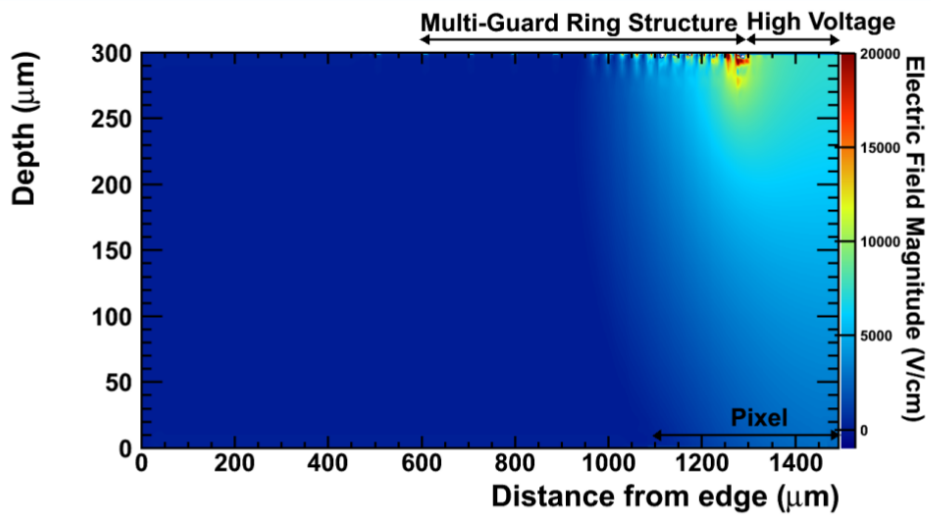
(b)

Figure 3.15: Electric field magnitude in the Slim-Edge multi-guard ring structure with a shift of $100\,\mu$m (a) and $200\,\mu$m (b) [25].

Chapter 4

Electrical performances of REINER Sensors

4.1 Methodology

Different quality tests can be performed on sensors before taking any signal measurement. These tests consist in measuring the current-voltage (IV) and the capacity-voltage (CV) characteristics since they give informations on important parameters of the sensors, such as the depletion voltage, the leakage current and the silicon purity.

In this section the experimental setups and the methodology used for the IV and CV measurements of the sensors analysed in this thesis are explained. Also the effect of changing parameters like the temperature or the humidity in the experimental setup is shown. Monitoring the temperature, and eventually the humidity percentage, is important during an experiment since any variation of these quantities affect the reproducibility of the measurement.

Investigated Sensors

The sensors investigated in this thesis are grouped in Table 4.1. The nomenclature of the sensors follows these rules: the first number, "6142" or "312967", is the batch number[1], the second number, "14" or "9", symbolizes the wafer, and the third is the sensor's position on the wafer. An example of the n-side of a wafer from the IBL planar sensor wafer production of 2011 (details in Figure A.1, in Appendix A) is shown in Figure 4.1, where the number, coding the position of the sensors on it, is indicated. All REINER sensors, for example, are placed on the same position (05), therefore they all have the same ending number and, from now on they will be all referred to without their ending number.

The Front-End of the sensors follows a similar nomenclature, as can be seen in the

---

[1]The batch indicates a bunch of wafers having the same bulk type and bulk thickness.

last row of Table 4.1: "A8PL4WH" is the batch number, "60" the wafer, and "R10" the sensor's number.

Sensor	Sensor's Number	Type	Thickness (μm)
Guard rings diode	6142-14-16	Bare Sensor + LIL-P	250
Guard rings diode	6142-14-17	Bare Sensor + LIL-P	250
Piece of wafer	312967-9	Bare Sensor	300
Full REINER	312059-24-05	Bare Sensor	200
Piece of wafer	310893-04	Bare Sensor	200
Full REINER	310894-22-05	Bare Sensor	200
Full REINER	312060-07-05	Bare Sensor	200
Cut REINER	310892-01-05	Bare Sensor	200
Cut REINER	310892-05-05	Bare Sensor	200
Piece of wafer	331831-21	Bare Sensor	250
Piece of wafer	331831-22	Bare Sensor	250
Full REINER + Front End	371409-19-05 A8PL4WH-60-R10	Sensor assembly on PCB	200

Table 4.1: List of sensors investigated in this thesis.
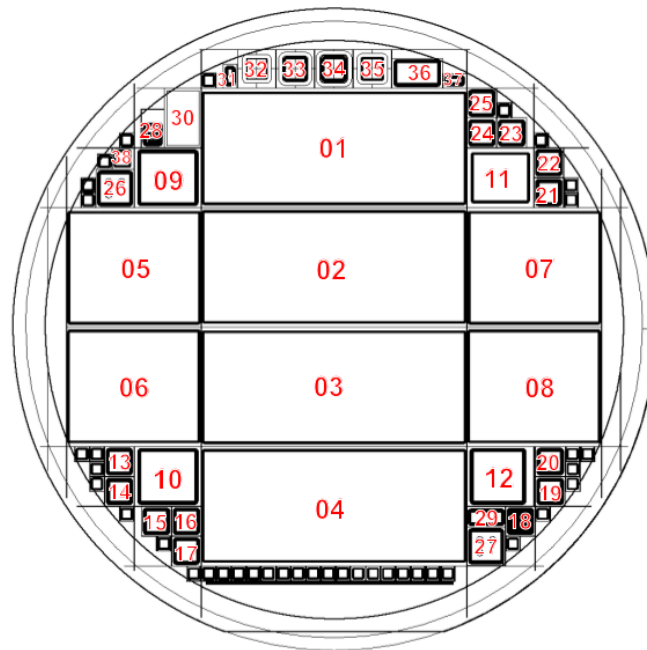
Figure 4.1: Layout of the n-side of the IBL planar sensor production wafer of 2011 (200 μm of thickness), with indicated the numeric code for the sensor's position [28].

The difference between "Full" and "Cut" sensors will be explained in 4.4. In the third column, the type of the sensor is shown, namely if they are bare sensors or assembly, and if they are mounted on PCBs. The last column reports the absolute value of the sensors' thickness, taken from the production's specifications.

All the sensors listed in Table 4.1 are an original ATLAS production. They are all n^+-in-n sensors except for 312967-9 which contains n^+-in-p sensors.

Software

The used measurement software in this thesis is *E4control*, *"a python-based software for device controlling and data taking"*[2]. The software is based on the *e4meas*-library, which uses a Phyton-framework and includes all the measurement devices, such as the Source Meter *Keithley 2410*, the LCR Meter *HP 4284A*, the Climate Chamber *Weiss SB22*. The device classes implemented for this library can be used to perform measurements by running one of the scripts already provided. It is also possible to log and control both the temperature and humidity through the sensor *SHT75*, which is read-out by a *Raspberry pi*.

4.1.1 IV Measurements

The IV characteristic of a sensor is obtained by measuring the leakage current as a function of the applied bias voltage. The measurements are performed inside the Climate Chamber *Weiss SB22* and the schematic setup is shown in Figure 4.2: the bias voltage is provided by the source meter *Keithley 2410* and applied to the p-side of the sensor. The ground of the source meter is instead applied on the chuck (the metal plate shown in Figure 4.3b) and therefore on the n-side. We assume that any deviation from the ground potential due to the contact between the chuck and the n-side of the sensor is negligible. The source meter is connected via GPIB cable and a GPIB-to-Ethernet adapter to a network.

Depending on the type of the investigated sensor, two different setups can be used. The setup used for the guard rings diode is shown in Figure 4.3a. The diode is connected to the LIL-P via wirebonds (indicated in figure) and a LEMO connector is used to apply the bias voltage and the ground, provided by the source meter. Bare sensors, like the ones on 312967-9, are instead biased with the help of a probe needle and attached (n-side down) on a chuck with the use of a vacuum pump. The laboratory ground potential is connected to the chuck. This setup is shown in Figure 4.3b and allows the measurement of single structures.

Before sourcing the voltage, the "compliance limit" of the source meter is set to 10 μA. This value is used by the device to adjust the applied voltage in a way that the current

---

[2]`https://github.com/sdungs/E4control/blob/master/README.md`
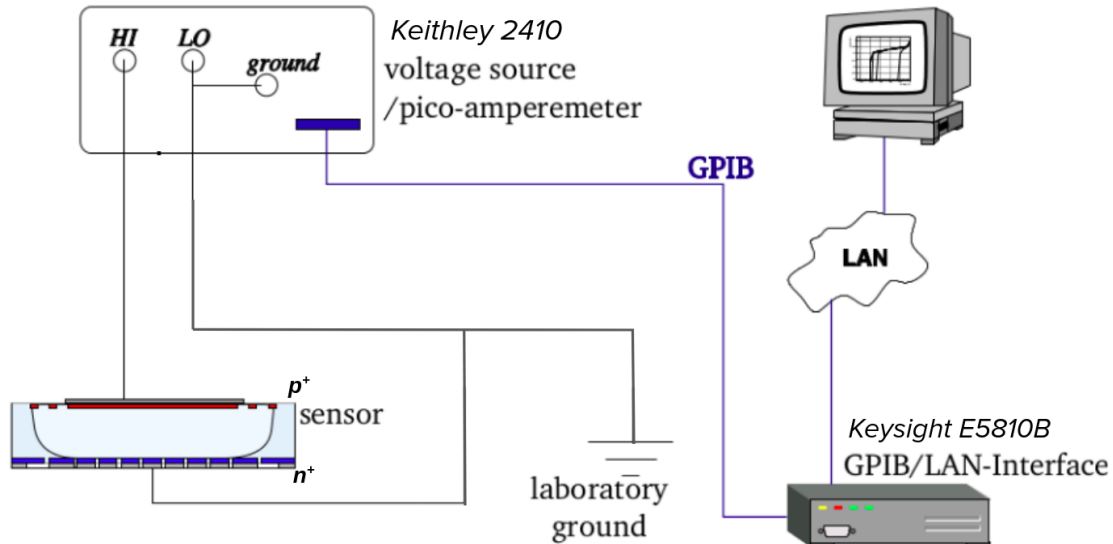
Figure 4.2: Schematic setup for IV measurement, originally taken from [28] and modified.

(a)   (b)
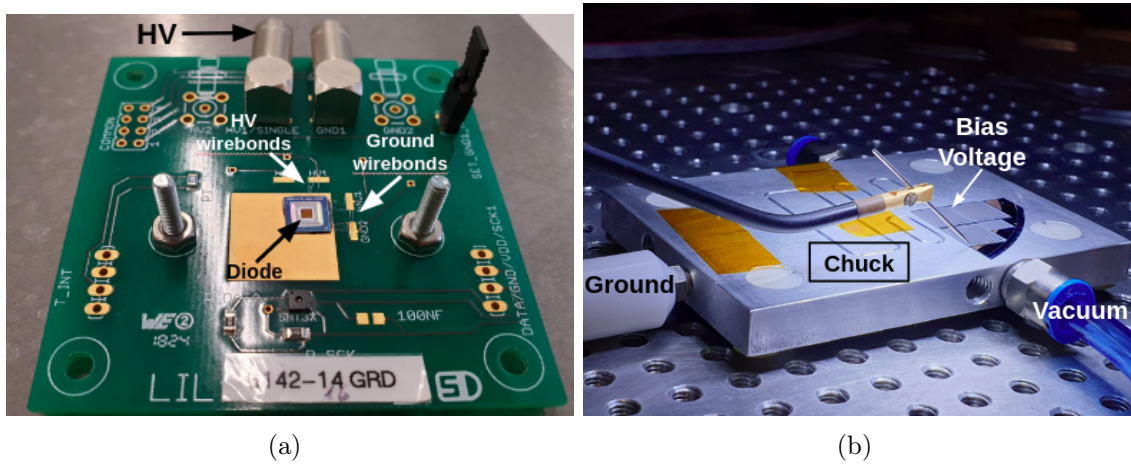
Figure 4.3: The diode 6142-14-16 mounted on the LIL-P (a), and the setup for the IV measurement of the sensors on 312967-9 connected via a needle (b).

does not exceed this limit. The IV curve is obtained using the python software *IVmeas* provided by *e4control*. For each voltage step, the current is measured n times, while n can be set by the user. The software calculates the mean value I_{mean} and its standard error ΔI_{mean} of the n measurement points.

As a primary check, the IV measurements of the diode 6142-14-16 and the four sensors present on 312967-9 are shown in Figure 4.4. The four sensors are shown in the sub-figure
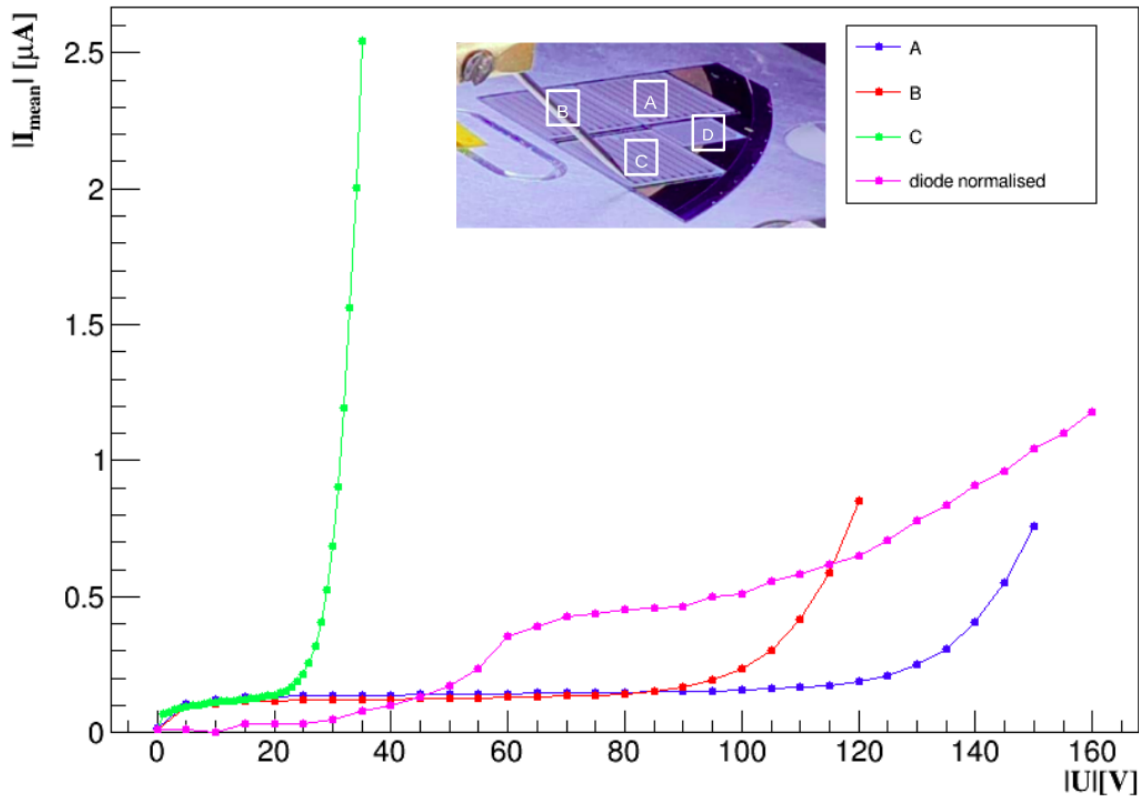
Figure 4.4: Comparison among the IV curves of the sensors A, B, C on 312967-9 and the diode 6142-14-16.

of the plot and are labelled as 'A', 'B', 'C', 'D'. The plot does not show the IV curve of the 'D' sensor because it is smaller than the others. All the measurements are taken at room temperature. Each value of the current is plotted with its standard error ΔI_{mean} given by the software, but the error bars are to small to be seen in this plot.

The diode "16" is chosen for comparison with the sensors A, B, C, instead of the "17", because it has better IV-shape in terms of longer plateau before the breakdown region. Since the current in the diode is many orders of magnitude smaller than the current measured in the sensors on 312967-9, a scaling factor has to be chosen for the comparison. Taking the current values at $U_{bias} = 0\,\mathrm{V}$, the mean value of the ratios $\frac{I_S}{I_{diode}}$ (with S = A, B, C) is calculated and taken as a scale factor of the diode's IV curve, for comparison with the other IV curves. In particular, the numeric number used is 129.

The parameters used for the IV measurements are listed in Table 4.2. As can be seen from the voltage range, the sensors have to be always measured in reverse-bias condition. For the diode, negative voltage is applied on the p-side (ground on the n-side), while for the sensors A, B, C, positive voltage is applied on the p-side (ground on the n-side),

because they are n$^+$-in-p sensors, while the diode is an n$^+$-in-n.

Parameter (sensor)	Set Value
Voltage range (diode)	(0, -200) V
Voltage range (A,B,C)	(0, 200) V
Voltage step (diode, A, B)	5 V
Voltage step (C)	1V
n of data acquisition per step (all)	10
Current limit (A, B)	1 μA
Current limit (C)	3 μA
Current limit (diode)	0.01 μA
Delay between two measurements (all)	5 s

Table 4.2: Set parameters for the IV curves in Figure 4.4.

The breakdown region of the IV curves in Figure 4.4 is clearly visible for each sensor: A and B have breakdown voltage of, respectively, $\sim$130 V and $\sim$105 V, while C shows an earlier breakdown ($\sim$25 V). For this reason, the current limit of C is increased to 3 μA instead of 1 μA during the measurements, in order to log the whole characteristic of the sensor. Moreover, smaller step in voltage of 1 V, instead of 5 V, is used in order to obtain enough points for the curve.

4.1.2 Temperature Measurements

The IV measurements are performed in the climate chamber in order to monitor and change the chamber's temperature (T) and humidity (H) to analyse the dependency of the leakage current from these two quantities.

Three SHT75 sensors are used: S1 is on the chuck, close to the investigated sensor; S2 is left free in the chamber and S3 is positioned near the fan of the climate chamber. When the chamber is cooled down, the S1 sensor is the warmest since it represents the chuck's temperature and it takes longer to cool down compared to the air temperature, measured by S2. The python software *dcs*, provided by *e4control*, is used to control and set T and H directly from the computer. When the set values are reached and show no significant variation, the IV measurement is performed. The IV curves of the sensor 312967-9A, at three different temperatures (22 °C, 15 °C, 5 °C) is shown in Figure 4.5. Also the error of each current value, calculated by the program, is plotted, but the error bars are to small to be seen.

The plot shows an overall lower leakage current at all voltages as the chamber is cooled down. The breakdown voltage of the curve instead slightly increasing with lower temperature, from $\sim$130 V at T = 22 °C to $\sim$140 V at T = 5 °C.
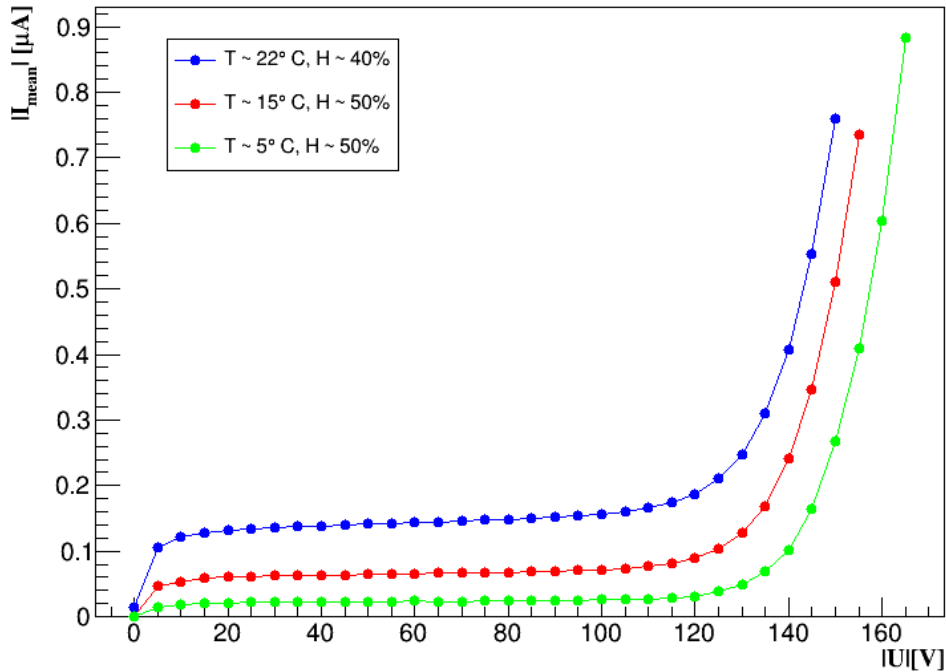
Figure 4.5: IV curves of 312967-9A at different temperature and humidity conditions.

Using the Equation 2.10, the expected scaled current values are calculated and compared with the measured current values, at different temperatures. The numerical values used for the constants are: E_g (silicon) $= 1.7945 \cdot 10^{-19}$ J and $k_B = 1.3087 \cdot 10^{-23}$ J/K.

Two examples are given: a "down" temperature scaling (T $= 22\,°\text{C} \rightarrow 15\,°\text{C}$) and an "up" temperature scaling (T $= 5\,°\text{C} \rightarrow 15\,°\text{C}$). The ratio $\frac{I_{calc}}{I_{meas}}$ of the calculated scaled current and the measured current (at T $= 15\,°\text{C}$) is shown in Figure 4.6a for the "down" scaling and in Figure 4.6b for the "up" scaling. The values at V $= 0$ V are not shown because the measured current values at this voltage are not really reliable, therefore they do not match with the theoretical predictions. At all voltages, the ratio is close to one, thus the values compare well with each other. At low voltages until ~ 10 V and at higher voltages, larger than 120 V, the comparison is not anymore reliable since, as it can also seen in Figure 4.5, the current values measured in the breakdown region are farther away from each other. An opposite behaviour at higher voltages can be seen: in the "down" scaling, the calculated values seem to underestimate the measured ones, while in the "up" scaling the calculated values are overestimating them. This can be explained by the fact that the temperature sensor S1 is actually measuring the chuck's temperature and not the sensor's temperature. In Figure B.1 (Appendix B) the comparison between the IV curves calculated and measured for the two scaling examples are shown.
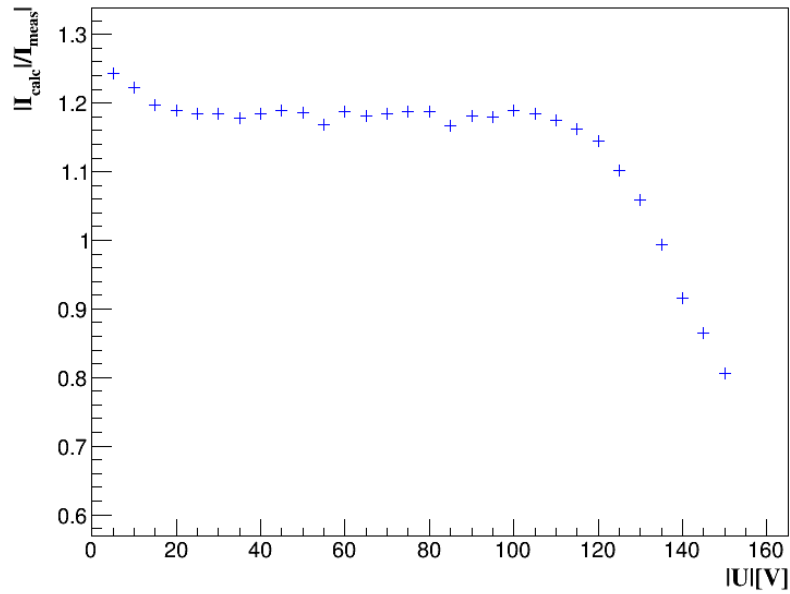
(a)
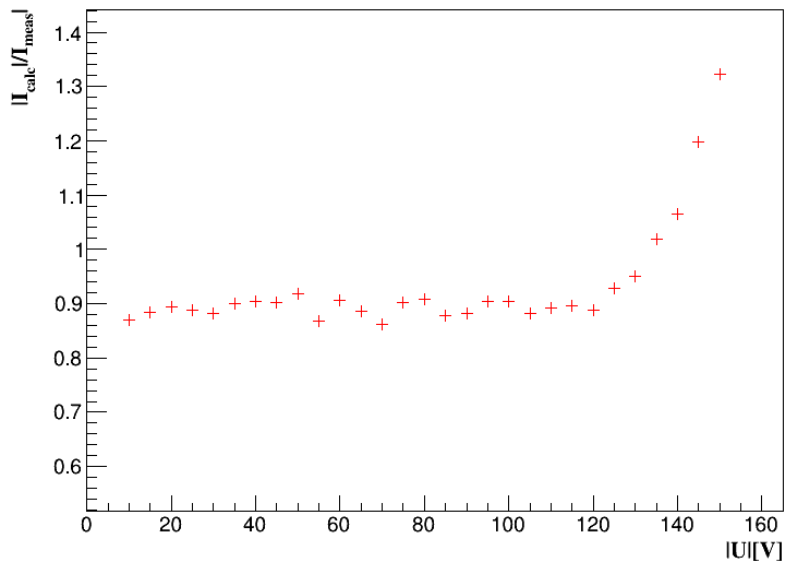
(b)

Figure 4.6: Ratio of the expected current values and the measured ones, for a "down" scaling $(T = 22\,^\circ C \rightarrow 15\,^\circ C)$ in (a) and for a "up" scaling $(T = 5\,^\circ C \rightarrow 15\,^\circ C)$ in (b).

4.1.3 CV Measurements

The CV characteristics is obtained by measuring the capacitance of the sensor as a function of the applied bias voltage. The LCR meter *HP 4284A* measures the capacitance by applying an AC voltage (of amplitude 50 mV) on the investigated sensor and measuring the amplitude and the phase shift of the resulting current. It operates with the *four-terminal* pair configuration, which divides sensing from powering cables. These four output terminals are then connected via BNC cables to a biasbox, whose main role is to separate the LCR meter from the HV supplied by the source meter. The use of the source meter is justified by the fact that the maximum applicable voltage of the LCR meter is 2 V, therefore it needs an external source [23]. The LCR meter is then connected via GPIB and GPIB-to-Ethernet adapter to the network. The schematic setup for CV meausurements can be seen in Figure 4.7.
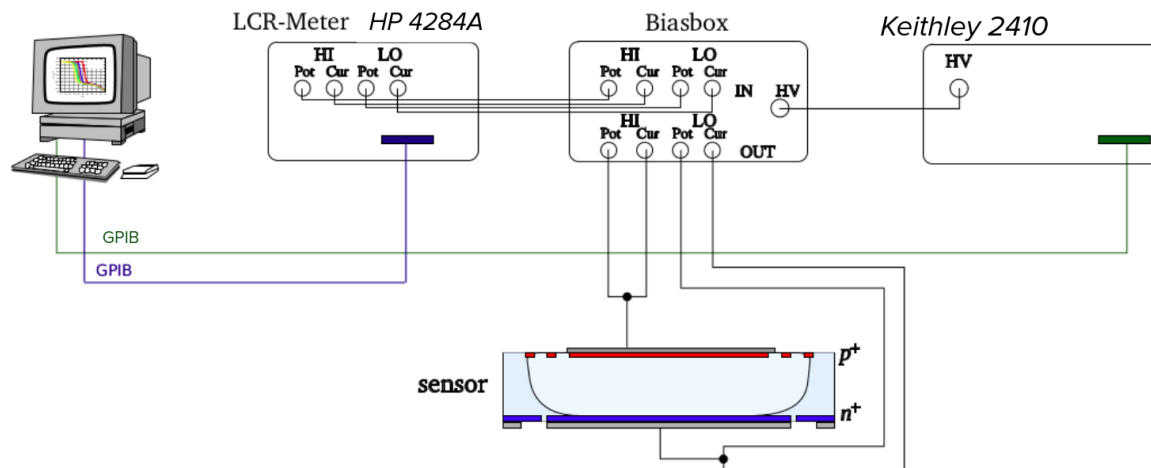
Figure 4.7: Schematic setup for the CV measurement, originally taken from [28] and modified.

The LCR meter calculates the capacitance using two parameters, obtained from the amplitude and the phase shift of the signal. Various parameters need to be set in this device in order to achieve optimal measurement results. The tuned parameters for the measurements performed are shown in Table 4.3. The frequency and the signal level settings influence the exact results of the depletion voltage [23]. After setting these values, the open and short corrections are performed. This is done constructing, respectively, an open and a short circuit with the LCR terminals. The calculated values are then automatically subtracted from the measured capacitance by the LCR meter.

The CV curves are obtained using the python software *CVmeas* also provided by *e4control* which gives the mean value of the capacitance C_{mean} and the standard error ΔC_{mean} of $n = 10$ measurements per voltage step. The reverse squared value of the

Parameter	Set Value
Frequency	10 kHz
Level	50 mV
Open Correction	On
Short Correction	On

Table 4.3: Settings of the used LCR meter parameters.
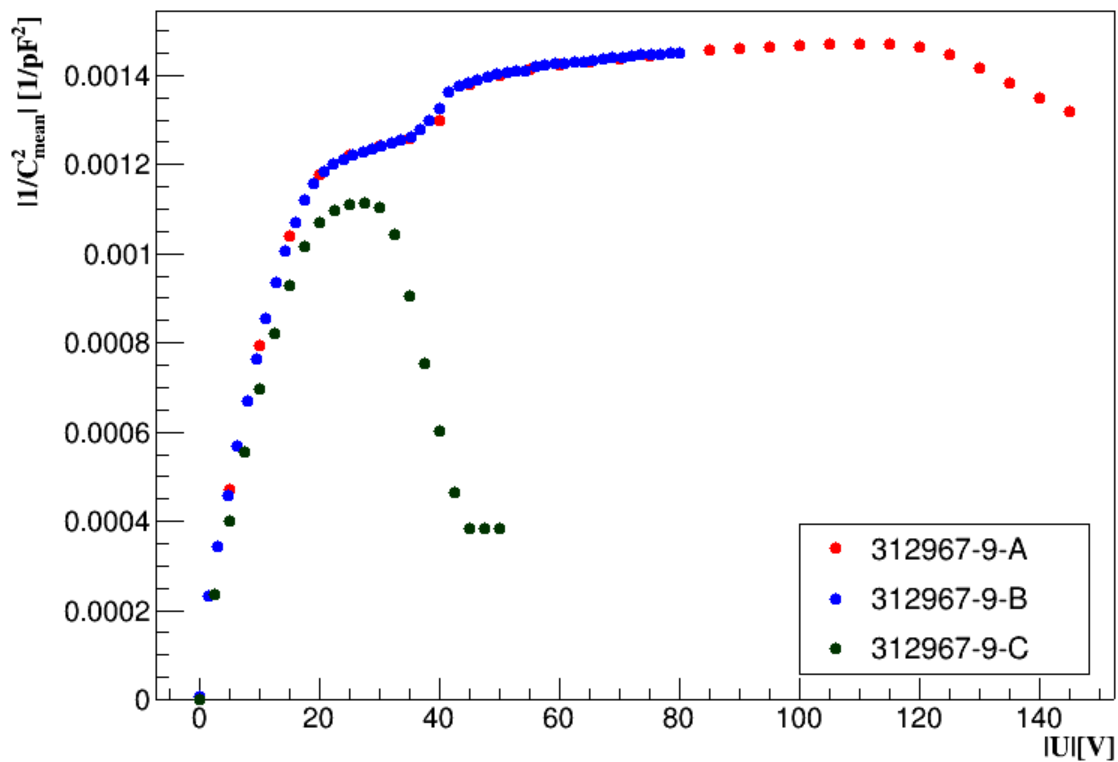
Figure 4.8: CV measurements of the sensors 312967-9A, B and C.

capacitance $1/C^2$ is calculated and plotted as function of the bias voltage due to their linear relation, as showed in Equation 2.12. The CV curves of the sensors A, B, C are shown in Figure 4.8 and the parameters used for CV curves are listed in Table 4.4. Since the sensors have different breakdown voltages, the CV curves evolve in different ways. At higher voltages, a slight (sensor A) or steep (sensor C) decrease can be seen due to the avalanche current generated in the sensor after the breakdown voltage.

The value of the capacitance (or its reverse squared) decreases (increases) with grow-

Sensor	Parameter	Set Value (V)
A	Voltage range; Vstep	(0, -145); 5
B	Voltage range; Vstep	(0, -80); 1.6
C	Voltage range; Vstep	(0, -50); 2.5

Table 4.4: Set parameters for the CV measurement of the sensors A, B, C.

ing bias voltage as in a plate capacitor. Increasing the bias voltage, the depletion zone increases and the capacitance decreases. If the depletion zone extends through the full sensor thickness and the sensor's current is not in breakdown, the capacitance saturates. Thus, the sensor is fully depleted and the depletion voltage can be calculated from the point of which the capacitance is constant. At higher voltages than the breakdown voltage, no statement can be made about the capacitance since the leakage current is affecting its value.

The direct comparison between the IV and CV measurements of the sensor C are shown in Figure 4.9. The decrease of the reverse squared capacitance after the breakdown voltage is clearly visible.
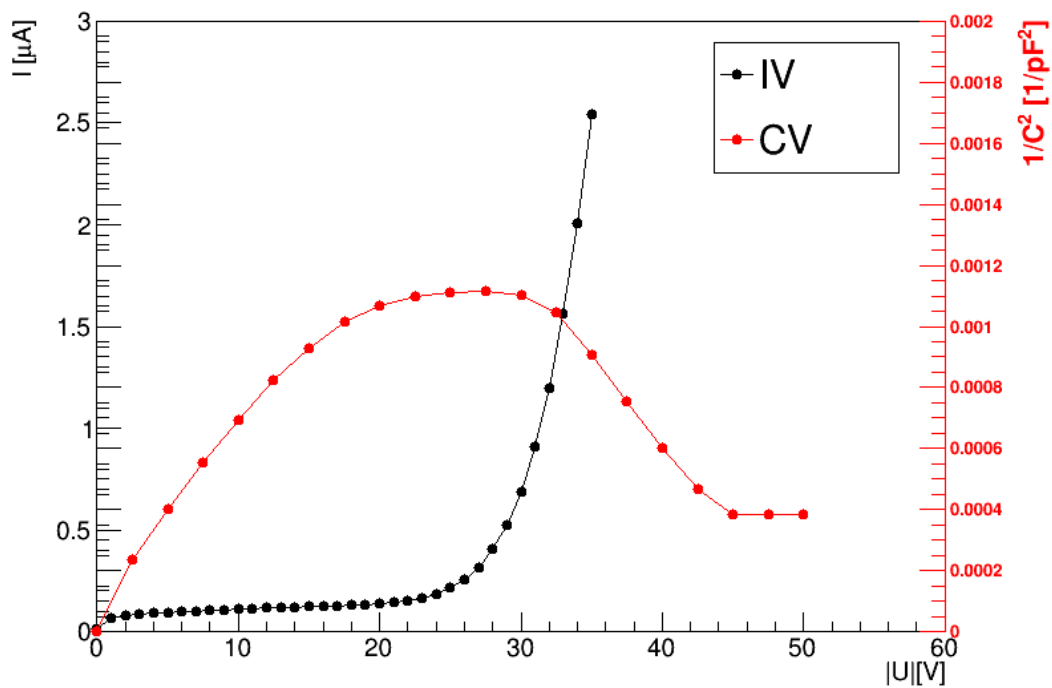
Figure 4.9: Comparison between the IV and CV curves of the sensor C.

Determination of the V_{dep} and N_{eff}

The CV measurement is an important tool to determine the depletion voltage of sensors. A straight line is fitted to the rise and to the plateau region and the depletion voltage is obtained from the intersection point of the two fitted lines.

An example of this is shown in Figure 4.10. The fit in the plot is performed in ROOT using the χ^2-method. Since the data around the depletion voltage do not match a straight line or a constant, several data points surrounding the guessed depletion voltage are not used for fitting ("non used data" in Figure 4.10). In particular, data between 17 V and 77 V are not used.
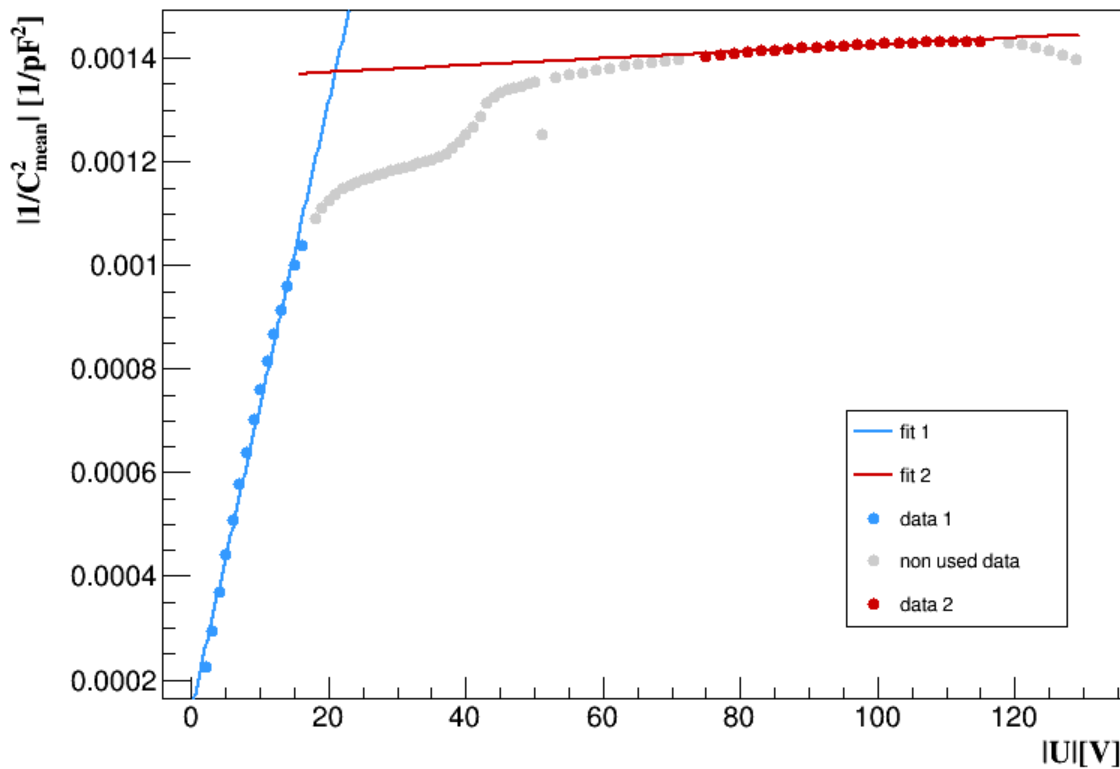
Figure 4.10: Determination of the depletion voltage for the sensor 312967-9A.

The depletion voltage of the sensors A, B and C are shown in Table 4.5. The errors of the depletion voltage are calculated with the formula of error propagation 4.1 using the results of the fit:

$$\delta q = \sqrt{\left(\frac{\partial q}{\partial x}\delta x\right)^2 + \cdots + \left(\frac{\partial q}{\partial z}\delta z\right)^2} \qquad (4.1)$$

As can be seen in Table 4.5, the depletion voltage values are consistent with each other within the error bars. The fact that the depletion voltage is almost the same among the three sensors is because the capacitance is a property of the silicon wafer therefore it does not change for different sensors of the same wafer. The error for the sensor C is larger because of the less number of points at disposal to fit the curves.

The effective doping concentration can be also extracted from the depletion voltage according to Equation 2.8. The results are shown in Table 4.5 using the bulk thickenss of Table 4.1 and the constant values: $\epsilon_{Si} = 12$, $\epsilon_0 = 8.85418 \cdot 10^{-12}\,\mathrm{F/m}$, $e = 1.602 \cdot 10^{-19}\,\mathrm{C}$. The errors are calculated also using Equation 4.1.

Sensor	Depletion voltage (V)	N_{eff} (1/m^3)
A	21.4 ± 0.7	$(3.2 \pm 0.1) \cdot 10^{17}$
B	20.7 ± 0.8	$(3.1 \pm 0.1) \cdot 10^{17}$
C	19.0 ± 1.3	$(2.8 \pm 0.2) \cdot 10^{17}$

Table 4.5: Depletion voltages and effective doping concentrations of the sensors A, B, C.

4.2 Measurements on Full REINER Sensors

4.2.1 IV measurements

The Full REINER sensors analysed in this section are listed in Table 4.1. IV and CV measurements are performed in the setup already described, inside the climate chamber, at a constant T $\sim$ 21°C and H $\sim$ 40%.

Figure 4.11a shows the contacted REINER sensor 312059-24. Each pixel design can be individually biased with the probe needle and, if the guard rings on the p-side are properly working, the different biased implantations show different IV characteristics.

Biasing the right and the left HV Pad

A measurement to understand if contacting the left (L) or the right (R) HV pad of each pixel implantation shows different results, is performed. The parameters used for the IV measurements of 312059-24 shown in Figure 4.12 are listed in Table 4.6.

Bias voltage is separately applied on the L and R HV pad (Figure 4.11b) and the results for the 05 and V2 design are shown in Figure 4.12. The current values are the mean of 15 values registered by the *IVmeas* program at each voltage step, and the error bars in the plot are calculated as the standard error by the program. As expected, no significant difference in the IV curves can be seen, therefore the pixel implants are then biased indifferently on the right or left pad, depending on the best configuration for the setup.

(a)   (b)
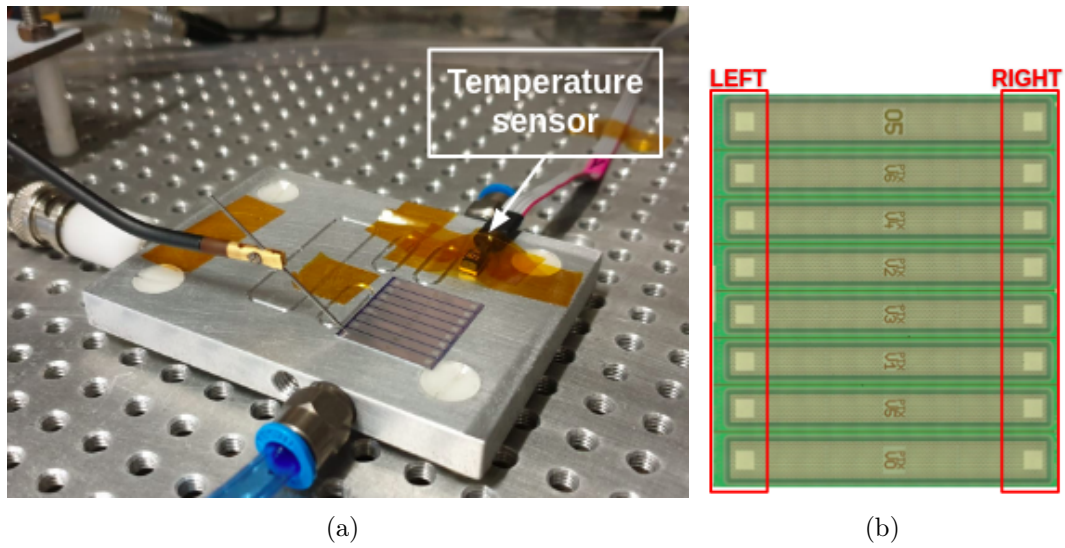
Figure 4.11: Left figure: contacted REINER sensor 312059-24 for the IV measurement. Right figure: the left and right HV pad of the pixel implants, investigated for the comparison.
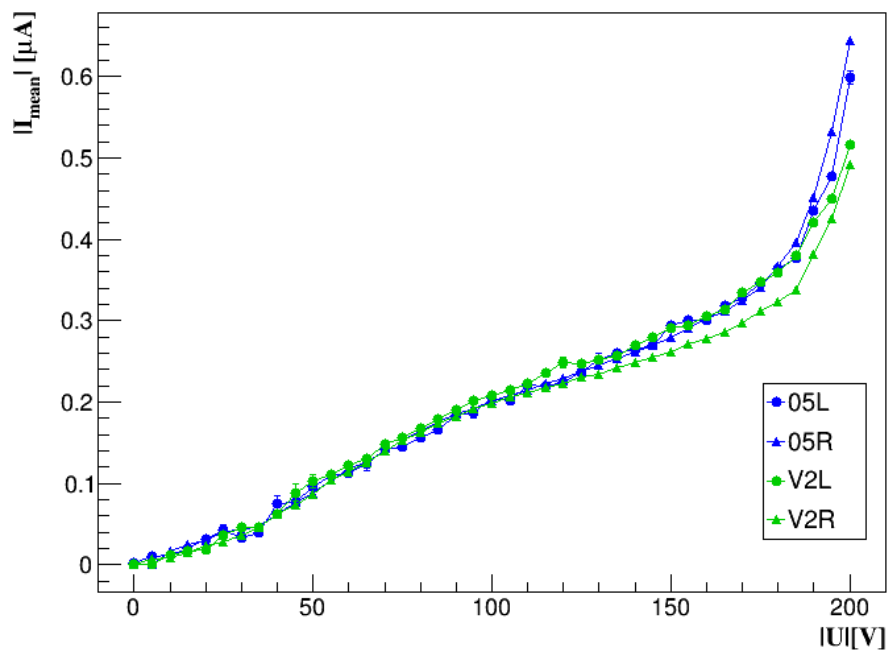
Figure 4.12: IV measurements of the 05 and V2 biasing the Right (triangle) and Left (circle) HV pad of the sensor 312059-24

Parameter	Set value
Voltage range; step	(0, -200) V; 5 V
Current limit	$3\,\mu A$
n meas per step	15

Table 4.6: Parameters for the IV measurement of 312059-24.

Improvement of the set-up

Some IV measurements showed high susceptibility to the experimental setup probably due to the loss of contact between the probe needle and the HV pad of the sensor. One of the measurement indicating this problem is shown in Figure 4.13a for the V6 design of the sensor 312059-24: a current consistent with zero is measured almost in the whole voltage range.

(a)   (b)
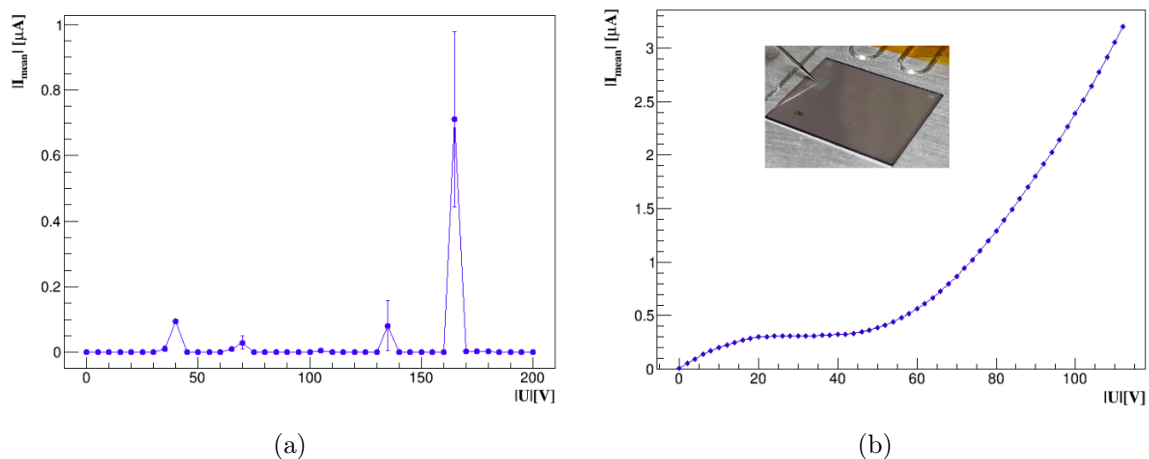
Figure 4.13: The probleamatic IV measurement of V6 on the left, and the IV of the sensor 310893-04 with the setup shown in Figure 4.14 on the right. In small, a photo of the contacted sensor.

Measurements performed in a climate chamber can suffer the problem of vibrating setup, because of the movement of the fan, if the chuck of the sensor is placed on a block in direct contact with the walls of the chamber. For this reason, in order to decouple the block from the walls of the chamber, tennis balls are introduced below it. The new setup with the tennis balls is shown in Figure 4.14. IV measurements of the sensor 310893-04 are taken in order to prove the good operation and improvement of the setup and are shown in Figure 4.13b.

Figure 4.14: New experimental setup with the introduction of the tennis balls.

IV measurements of the Full REINER sensor 310894-22 and 312060-07

The IV curves of the eight pixel designs of the sensor 310894-22 and 312060-07 are shown, respectively, in Figure 4.15 and Figure 4.16. The measurement parameters are the same listed in Table 4.6 except for the current limit which is now enlarged to $10\,\mu$A in order to log the complete IV shape. For Figure 4.16 also the voltage range is enlarged up to -400 V in order to investigate the breakdown region.

As already described in [26, 37], the highest leakage currents are observed for the V5 and V6 designs. Their earlier breakthrough, at $\sim$150 V, is due to the narrowed n^+ implantations.

4.2.2 CV measurements

CV measurements of the V2, 05 and V0 designs of the sensor 310894-22 are shown in Figure 4.17. Since V0 and 05 have the same standard pixel design, similar results for both of them are expected. From previous results in [26, 37], it is expected that the other designs show CV curves in between the V2 and the V0, 05 designs because these last two designs have larger n^+ implantation and not segmented, therefore higher capacitance.
The procedure to calculate the depletion voltage is shown in Figure 4.18 for the 05 design. In the fit, values between 24 V and 50 V are not used, as indicated in Figure 4.18. The depletion voltage values for the three designs are shown in Table 4.7 and they agree within the error bars, as expected, since they are part of the same sensor.
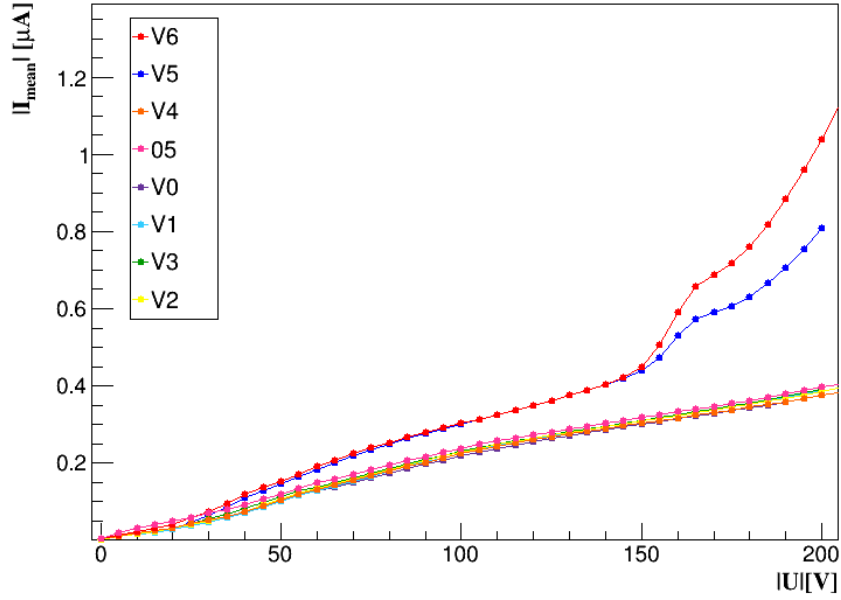
Figure 4.15: IV curves of the sensor 310894-22.
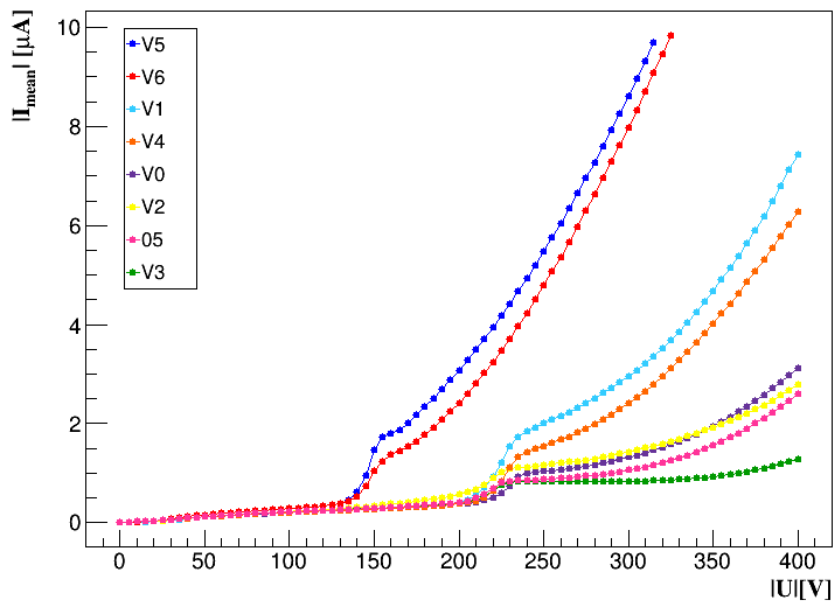
Figure 4.16: IV curves of the sensor 312060-07.
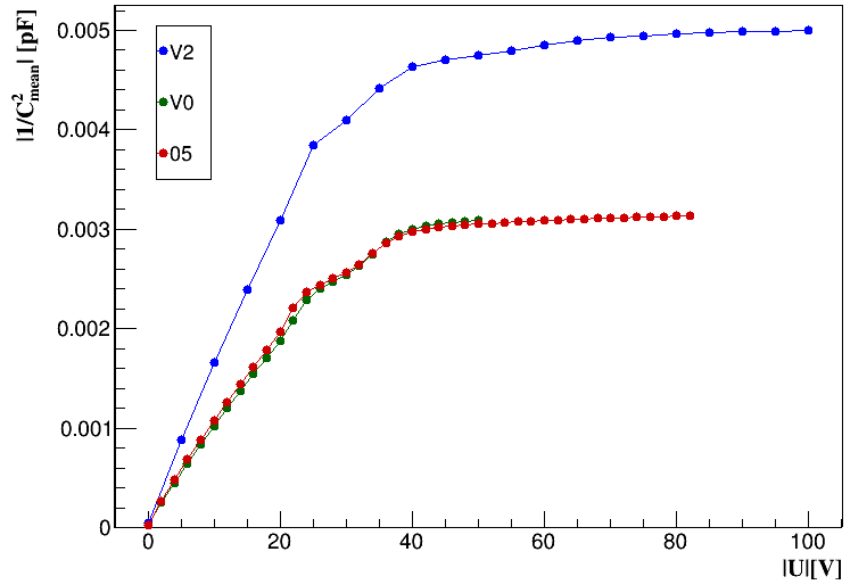
Figure 4.17: CV curves of the V2, 05 and V0 designs of the sensor 312060-07.
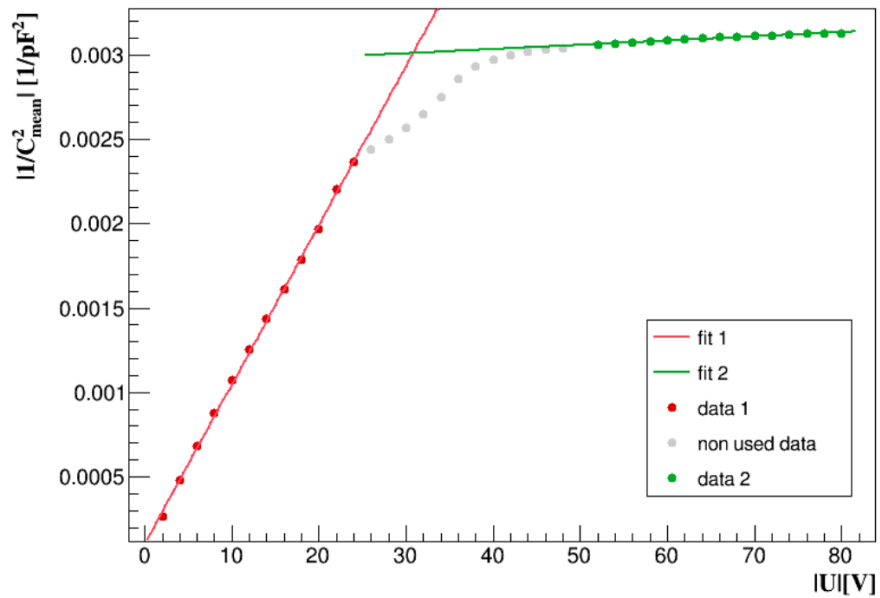
Figure 4.18: Depletion voltage calculation of the 05 design of the sensor 312060-07.

Design	Depletion voltage (V)
V2	31.6 ± 0.6
V0	31.6 ± 0.5
05	30.7 ± 0.3

Table 4.7: Depletion voltage of V2, V0 and 05 of the sensor 312060-07.

4.3   Measurements on etched REINER Sensors

Motivation and etching procedure

The etching is a chemical procedure used to remove unwanted parts in the workplace material. This is done on the sensors in order to prepare them for laser induced charge measurements [38]. For these measurements, a laser illuminates the sensor and generates charge inside the bulk. Therefore, the metal layer needs to be removed if the photons need to reach the silicon material.

| (a) | (b) |
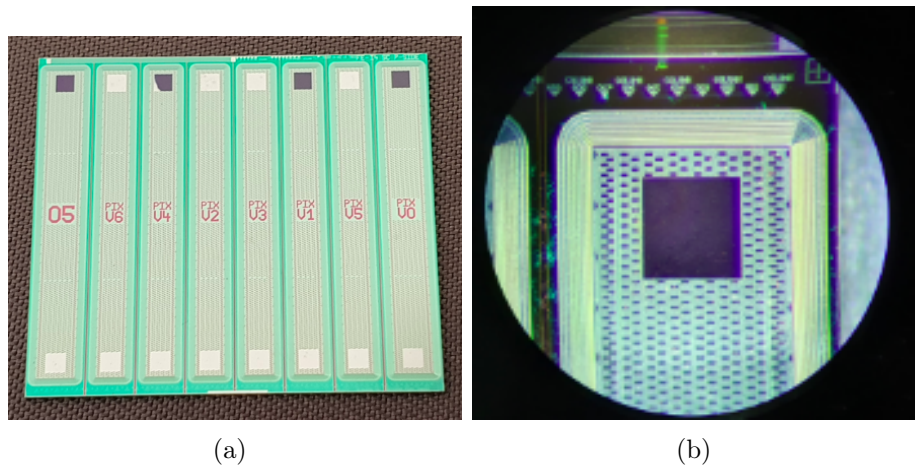
Figure 4.19: The etched 312060-07 sensor (a) and a microscopic view of the etched HV pad of V0.

The aluminium HV pads of the V0, 05, V1 and V4 design of the sensor 312060-07 are chemically etched (Figure 4.19a). The etchant used is sodium hydroxide NaOH at 20% in aqueous solution at room temperature, poured onto the HV pad through a pipette. Together with the etchant temperature, also the time the etchant is left to settle on the aluminium is important, since they affect the chemical activation of the etchant. After five minutes, the bubbles on the pad evaporate and the HV pad becomes black-tinted, which is the silicon colour. Then the pad is cleaned with water and the sensor is ready for test measurement. The microscopic view of the etched pad is shown in Figure 4.19b.

Consequences on the electrical properties of the sensor

To understand if the etched sensors are still usable for further studies and if, and how, the etching changed the electric properties of the sensors, IV curves are performed.

Figure 4.20 shows the IV curves of 05, V0, V1 and V4, before and after the etching. The curves are irreversibly affected after the etching, in a way that they do not show anymore the typical 'knee' rise of the REINER sensors, but an earlier and steeper breakdown. The curves group two-by-two because of the similar pixel designs: V1 and V4, 05 and V0 (see Figure 3.9).
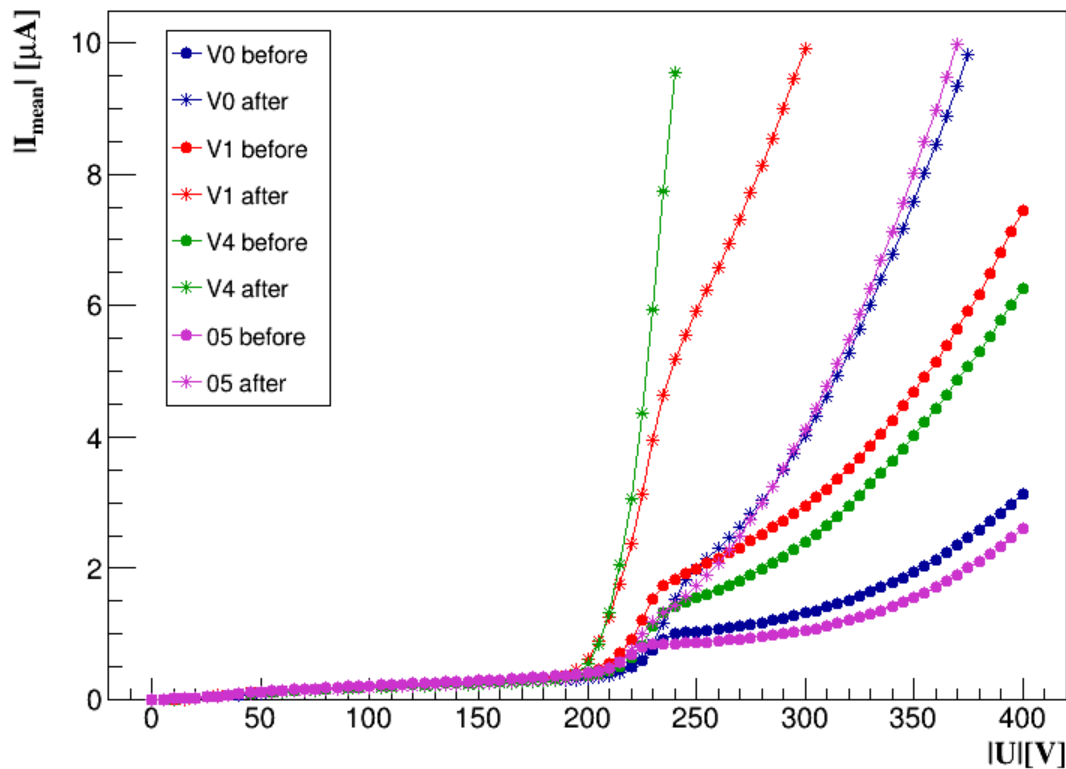
Figure 4.20: Comparison between the IV measurements of the V0, V1, V4, 05 designs of the sensor 312060-07, before and after the etching.

The relative current ratio of each etched design is shown in Figure 4.21 as a function of the bias voltage. A zoom of the y-axis around the zero value and in the voltage range (0 - 250) V is shown in Figure C.1 (Appendix C). In the plot, I_0 indicates the leakage current measured in the non-etched sensor, while I_E is the leakage current measured in the etched sensor. As can be seen, the value is almost zero at all voltages until the
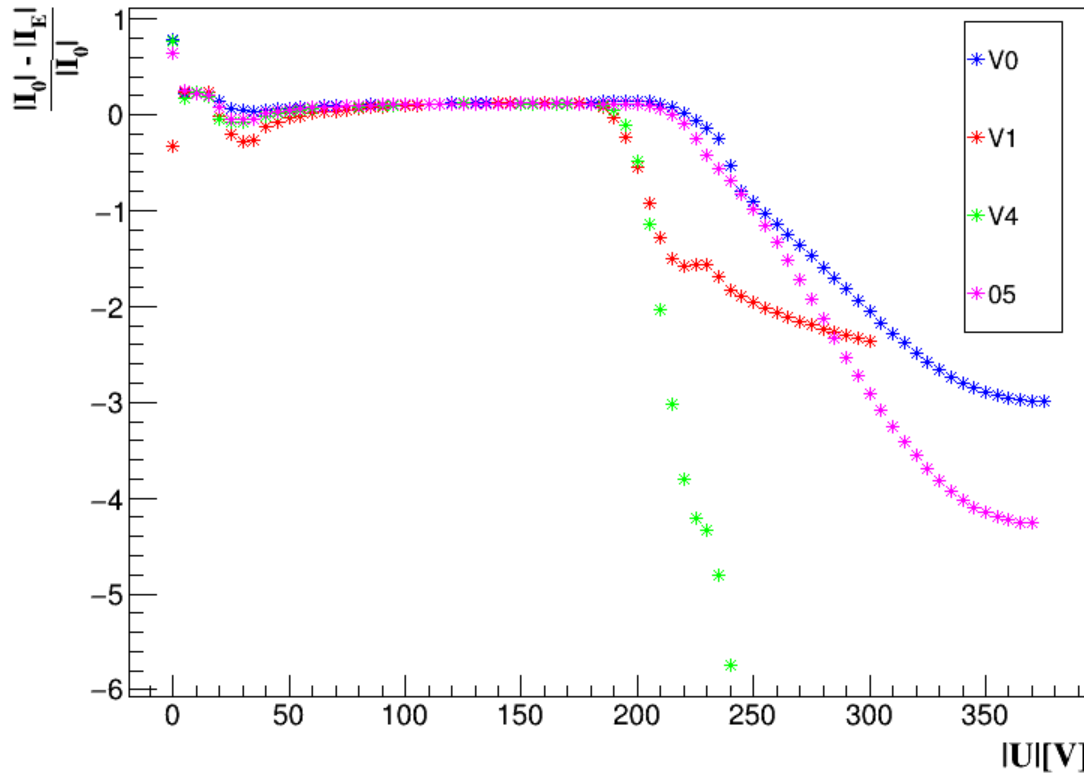
Figure 4.21: Relative current ratio of the etched design with I_0 the leakage current before the etching, and I_E the leakage current after the etching.

breakdown voltage is reached (200 - 250)V. At the beginning of the breakdown region, the difference starts to largely increase. The V4 design (green points) is the one more affected by the etching as can be seen from the steeper behaviour. This is also evident from the comparison of the IV curves in Figure 4.20.

Therefore, the etching changed the sensor characteristic, as the breakdown happens earlier. However, the change is small since the breakdown voltages are only shifted by a small amount, from $\sim 230\,\mathrm{V}$ to $\sim 210\,\mathrm{V}$ (reduction by only 9%).

4.4   Measurements on Cut REINER Sensors

The purpose of cutting the REINER sensors is linked to the investigation of the individual pixel design. If the guard rings around each structure (see Figure 3.11) are working properly, the different designs do not influence each other, therefore the cutting procedure should not affect the electrical properties of the sensor.

(a) (b)
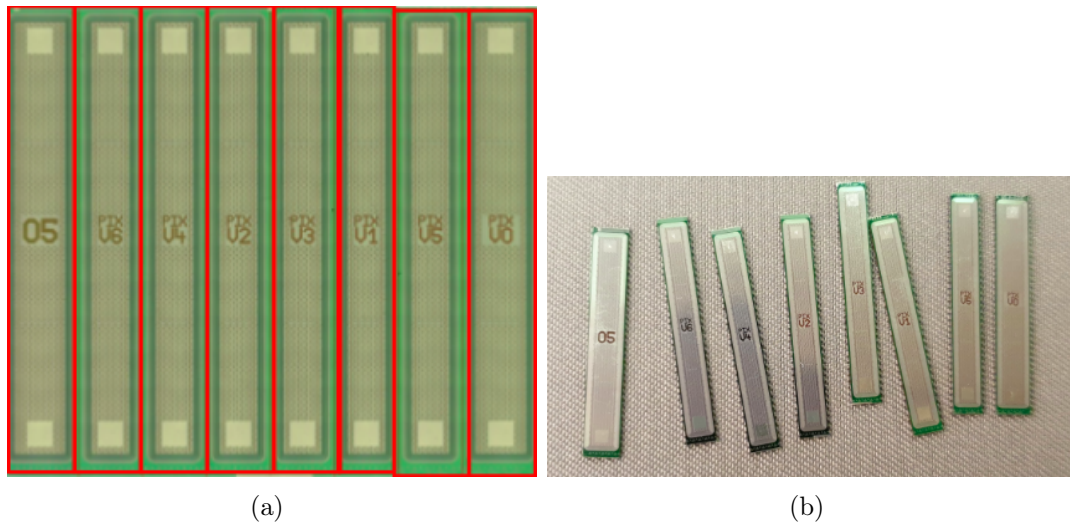
Figure 4.22: The cut lines of the REINER sensor (a), the cut sensors of 310892-01 (b).
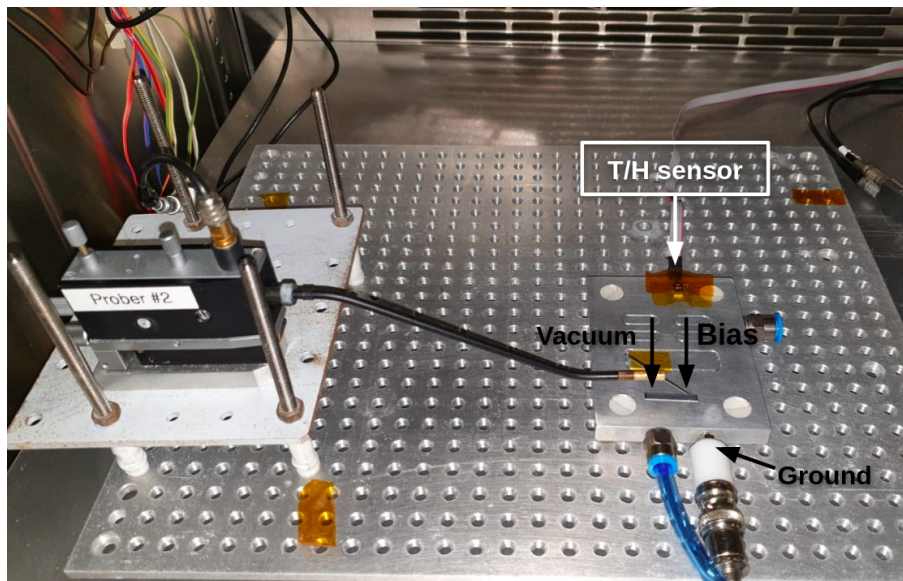
Figure 4.23: Experimental setup for the IV and CV measurement of the cutted sensors.

The Full REINER sensors 310892-01 and 310892-05 are cut along the lines shown in Figure 4.22a and an image of the cut sensors is shown in Figure 4.22b. The setup for the measurement of the IV and CV characteristics of the cut sensors is shown in Figure 4.23. Because of the small size of these sensors, the probe needle has to be applied together with the vacuum hole on the chuck in two opposite sides of the sensor, in order to counterbalance the sensor's position on the chuck. In this way, the sensor results

properly attached on the chuck.

The analysis on the cut sensors is compared with the corresponding full ones performed in [26]. The comparison among the IV curves of the two sensors 310892-01 and 310892-05 is shown, respectively, in Figure 4.24 and Figure 4.25. The results of the full sensors are shown with a cross, while those of the cut sensors are indicated via dots. The 05 design is missing for the sensor 310892-05 because it was used for other tests during the time of these measurements.
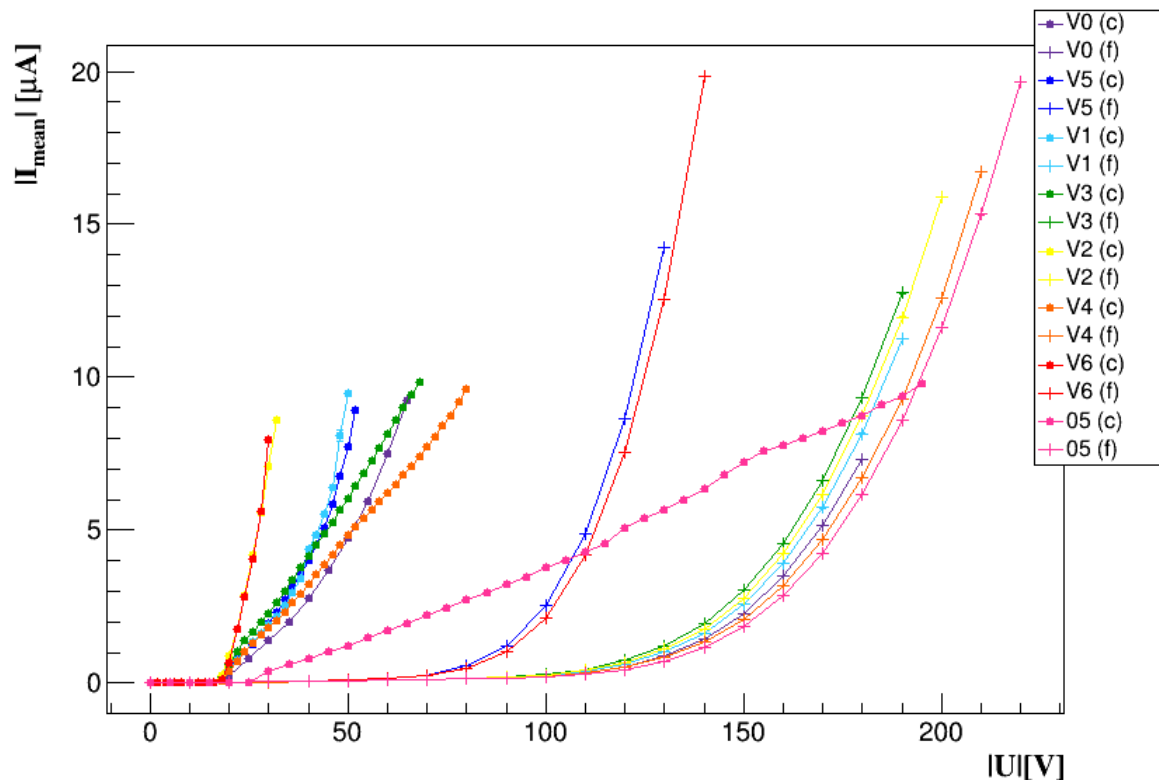
Figure 4.24: Comparison of the IV measurements of the cut and full sensor 310892-01.

The cut sensors result irreversibly damaged, as the breakdown voltages are largely reduced from about 90 V/140 V to ∼ 20 V for the sensor 310892-01, and from about 140 V/240 V to ∼ 20 V for sensor 310892-05. Figure 4.26 and 4.27 show a zoom of the IV curves of the cut sensors, where it is evident that they have completely lost the REINER sensors' properties therefore they can be hardly used in further application.

Also the CV measurements of the full and cut sensors are compared. The comparison is shown in Figure 4.28 for the sensor 310892-01 and in Figure 4.29 for the sensor 310892-05. Only the CV curves of V3, V4, V1, V2 and 05 are shown for the sensor 310892-01
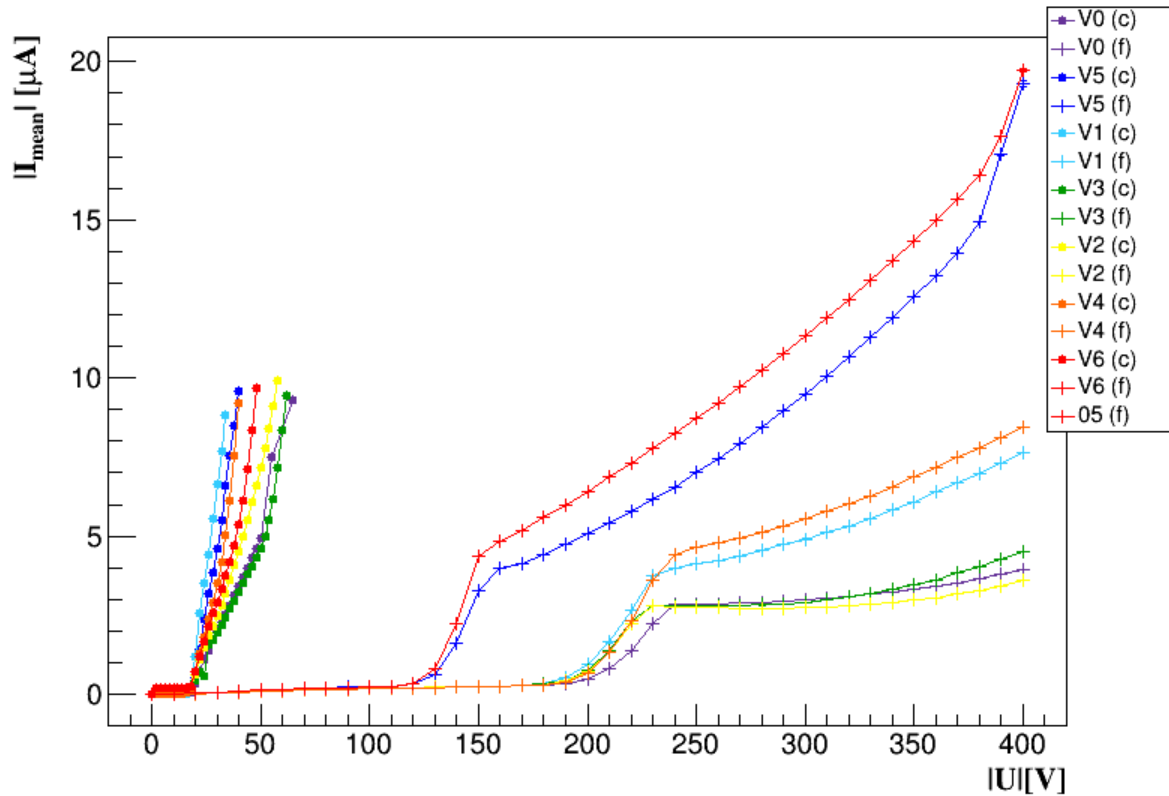
Figure 4.25: Comparison of the IV measurements of the cut and full sensor 310892-05.

and the designs V2 and V3 for the sensor 310892-05 because the other sensors show not comparable behaviour with the full sensors curves.

In Figure 4.28a, the rising is visible until 20 V but no plateau can be measured because the breakdown voltage is already reached. The same happens in Figure 4.29a, where a small plateau is visible before the breakdown voltage is reached. Therefore, the depletion voltage is the same of the breakdown voltage ($\sim$25 V) for sensor 310892-01 and just a little smaller for sensor 310892-05 ($\sim$20 V).

Further analysis

The idea that the higher resistance at the cutting lines may influence the measured IV curves of the cut sensors led to check also its behaviour. The resistance R is calculated
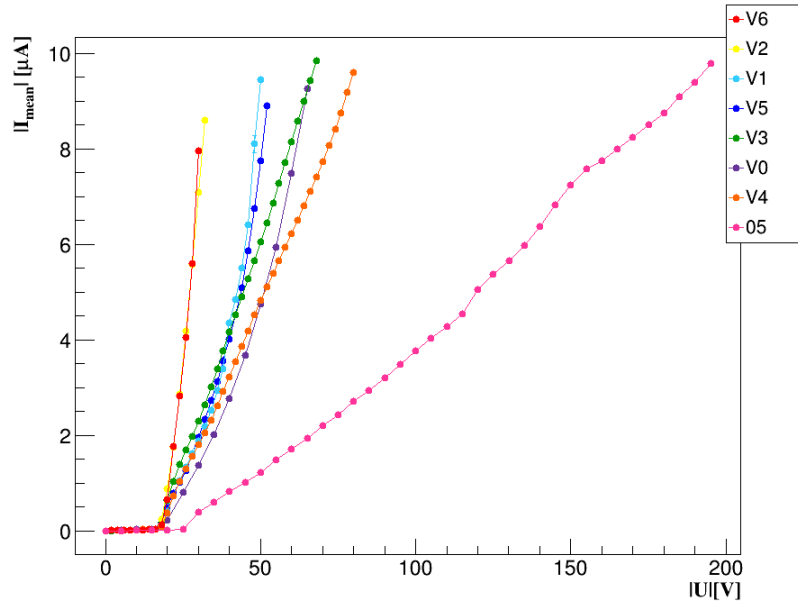
Figure 4.26: Zoom of the IV curves of the cut 310892-01.
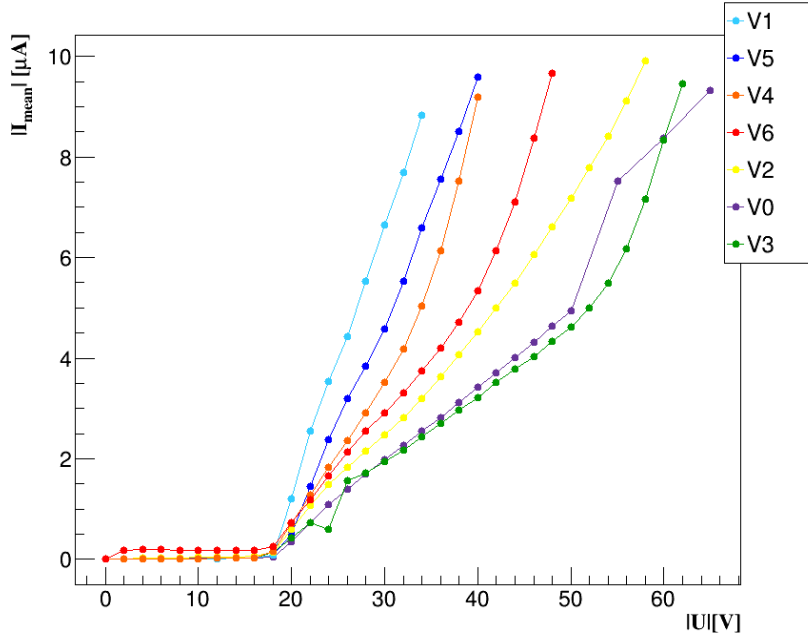
Figure 4.27: Zoom of the IV curves of the cut 310892-05.
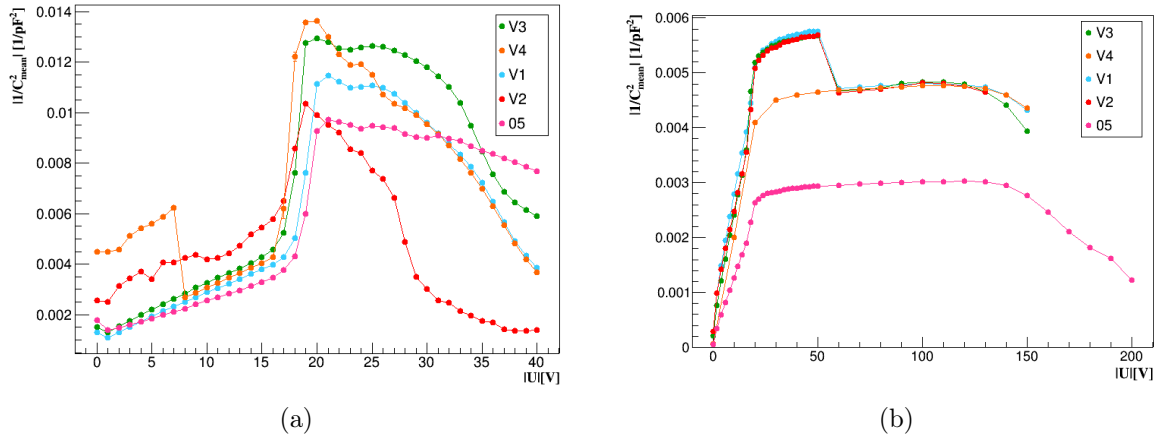
Figure 4.28: CV measurements of the cut (a) and full (b) 310892-01 sensor.
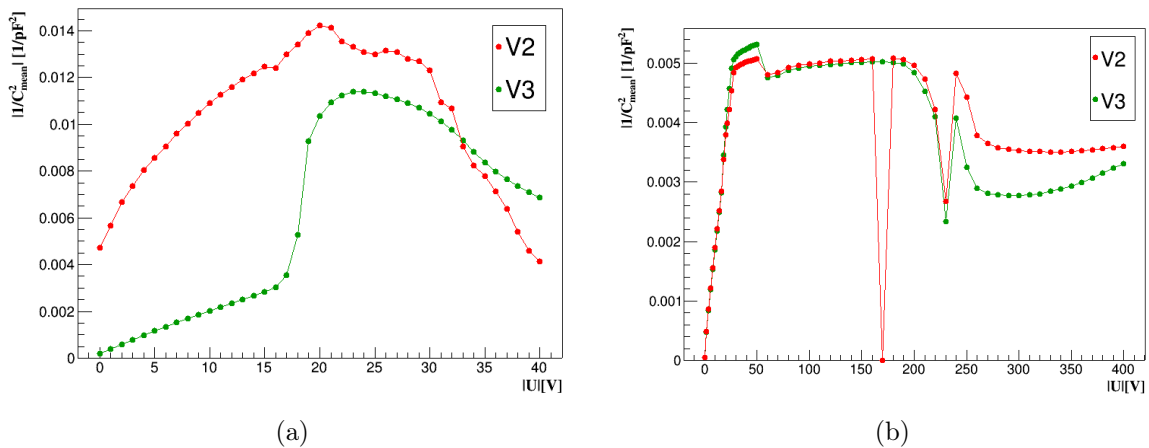
Figure 4.29: CV measurements of the cut (a) and full (b) 310892-05 sensor.

from the LCR parameters D and C using the formula[3]:

$$R = \frac{1}{2\pi f C D} \tag{4.2}$$

The calculated R is plotted as function of the applied bias voltage in order to compare the curve with the IV characteristic of the cutted sensors.

Figure 4.30 shows the IV and RV curves of V1 cut from 310892-01. The other designs are not shown since the curves show a similar behaviour. As expected, the resistance

---

[3]HP4284A Precision LCR Meter Operation Manual, Sixth Edition.
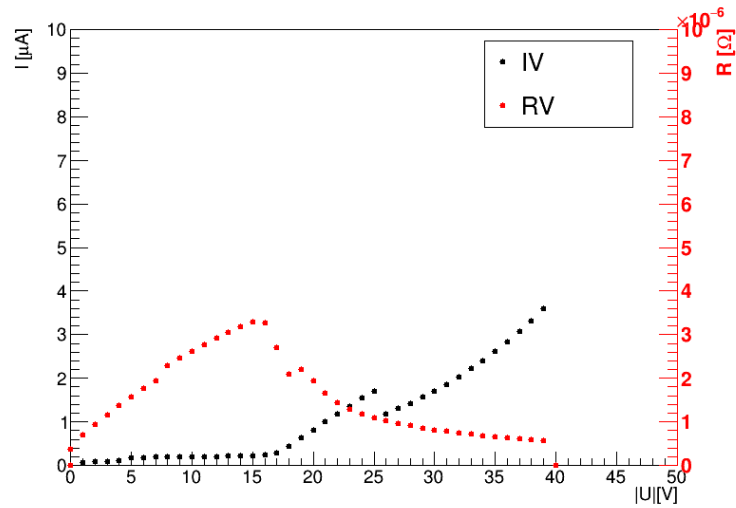
Figure 4.30: IV measurement and Resistance as a function of the bias voltage of the V1 design of the sensor 310892-01.

is increasing with higher bias voltages before reaching the breakdown voltage, and then sharply decrease. Anything anomalous is registered and therefore the strange behaviour in the cutted IV curves cannot be ascribed to a resistance influence.

Chapter 5

Guard Ring Structure Investigation

The characteristic "knee" shape of the IV curves of the REINER sensors (Figure 4.15 and 4.16) confirmed the results shown in the previous works [26, 37]. On the other hand, the measurements on the cut sensors have not encounter the expectation that the different pixel designs are electronically independent from each other. Therefore, the investigation of the 13 guard ring structure is necessary in order to study the potential distribution, hence the electric field development, between different pixel designs. Also, the edge is a critical issue for these sensors because of their "slim edge" design, shown in Figure 3.8. If an electric field reaches this region, the high density of surface defects, at the cutting edge, will generate high surface leakage current and, eventually, will cause breakdown.

In this chapter, the methodology and the setup to investigate the guard rings are described. Results of a pixel sensor and a diode are presented to verify the setup before guard ring studies are performed on the REINER sensors which are the same sensors investigated in Chapter 5.

5.1 Methodology

The main parameter of the investigation is the voltage drop over the guard rings, when biasing the sensor. Sensors are biased like in the setup described in Chapter 5, but additionally, a guard ring is contacted and the voltage between the setup ground and the guard ring is measured.

The HV is provided by the *Keithley 2400* and is applied on the p-side of the sensor, while the ground is applied on the n-side through the chuck. The voltage on the guard rings is logged by the multimeter *Keithley 2000*, already included in the *e4meas*-library, and has an input impedance in AC mode of $1\,\mathrm{M\Omega}$. The ground of the multimeter and the source meter are connected. Two probe needles are used for the measurement: the "HV needle" providing the bias voltage of the source meter, and the "GR needle" (GR = guard ring) measuring the voltage of the specific guard ring under test. The use of the

needle for the voltage measurement on the guard rings is justified by the small dimension of only $\sim (11 - 12)\,\mu$m for the smallest inner guard rings.

The measurements are performed inside a box, shown in Figure 5.1, in a clean room. The microscope is used to ensure good and precise positions of the needles. The chuck, where the sensors are placed, is connected with vacuum on ground potential.
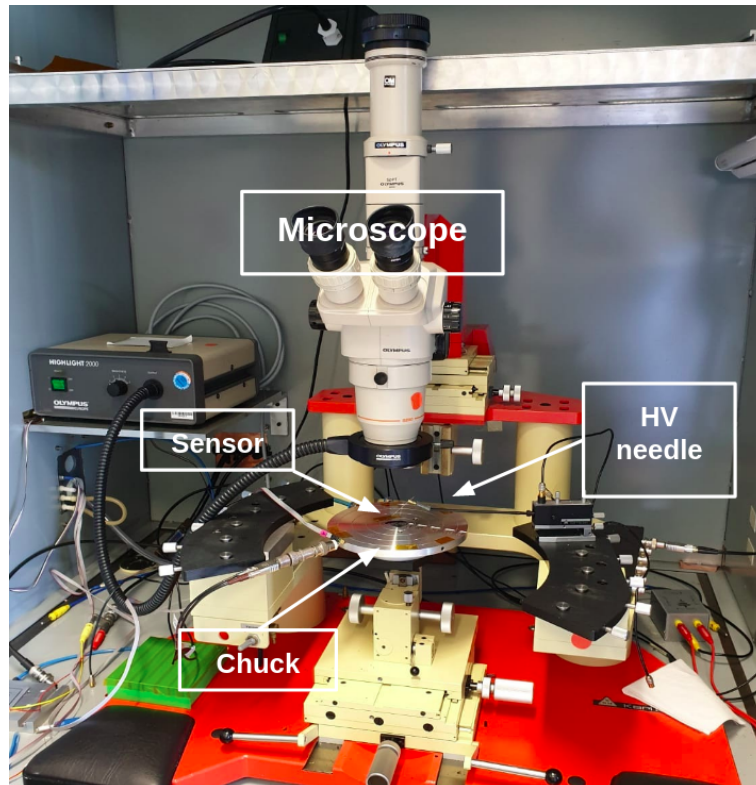
Figure 5.1: Setup in the box of the clean room with inside the microscope and the placement plane for the needles.

Guard rings are a very sensitive part of the sensor, therefore any measurements regarding them have to be done with the highest carefulness. The risk of damage on the sensor by contacting the guard rings is high since their role is to control the surface leakage current and the breakdown of the sensors.

The guard rings of n^+-in-n sensors are made of three layers (see Figure 3.5), from the inside outwards: p^+ implantation, metal and passivation. The passivation layer is used as a protection against mechanical damage and chemical contamination. Thus, the GR needle has to penetrate the passivation in order to measure the potential on the guard ring. Some sensors have an opening in the passivation layer to enable direct contact with the metal. The term *opening* (or *no-opening*) is used to indicate the absence (or the presence) of the passivation layer above the aluminium.

To contact the guard rings of a sensor with openings in the passivation layer, the n^+-in-n wafer piece (331831-21) is used. It is a part of the upper right corner of the wafer shown in Figure 4.1 and contains, among the others, the pixel sensor 11 and the diodes 21-25 (more details in Appendix A). An image of the opening in the 16 guard ring structure of the diode 22 on the wafer 331831-21 can be seen in Figure 5.2. The right image is a zoom of the opening, which appears in a brighter zone in the guard ring structure. In the figure, also the cutting lines (the so-called *dicing streets*) and some scratches are indicated.
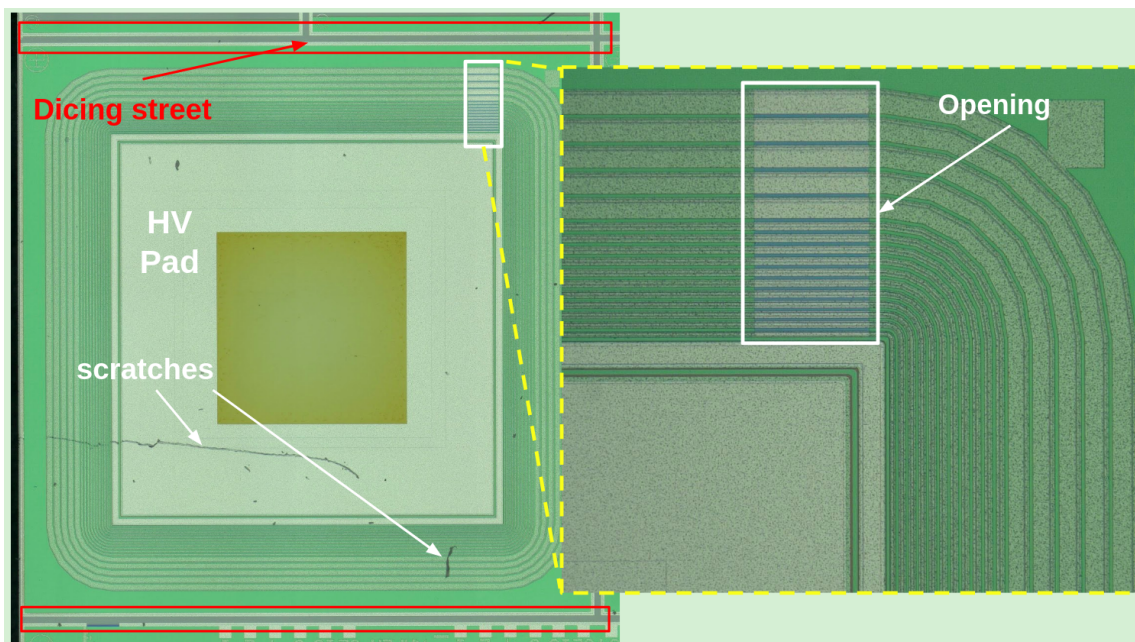
Figure 5.2: A microscopic view of the diode 22 on 331831-21: the opening in the passivation (in the zoom), the dicing streets, the HV pad and some scratches are indicated. The images are taken with the digital microscope *Keyence* with magnification factor of 100 (the whole diode) and 200 (the zoom).

5.1.1 Measurements on the Pixel Sensor

The pixel sensor 11 on the same wafer 331831-21, used for the first guard ring measurements, is shown in Figure 5.3. The contact points of the GR needle for the measurements are visible in this image as black marks, on the guard rings in the area with and without passivation, as well as on the dicing streets.

The sensor has a 13 guard ring structure which is shown in Figure 5.4. The guard rings are labelled from the outermost guard ring as 1 in increasing order going inwards of the sensor. The width of each guard ring is indicated in Table D.2 (in Appendix D). The
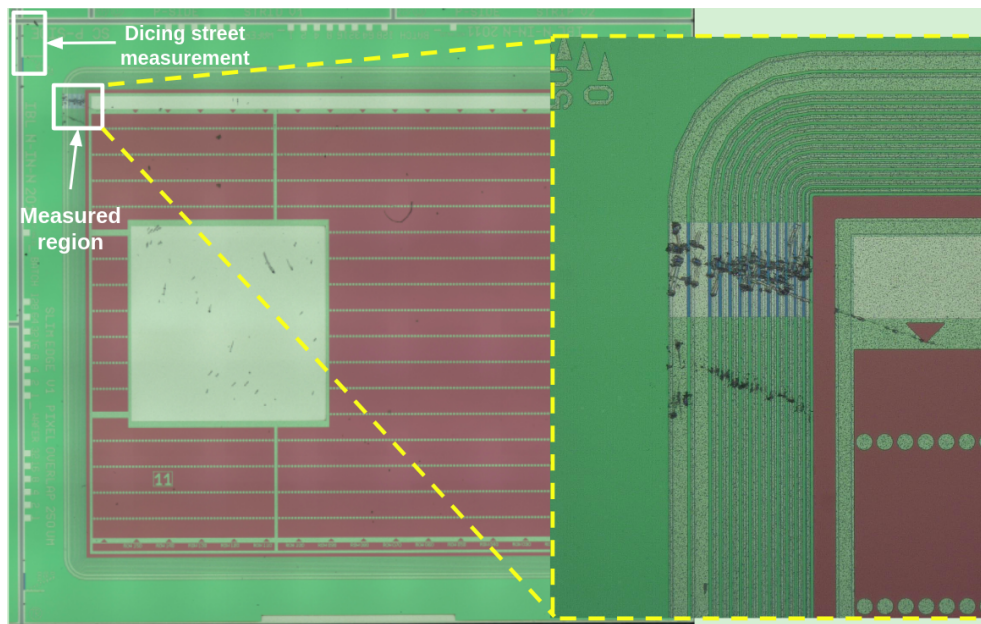
Figure 5.3: The pixel sensor 11 on the wafer 331831-21 showing the needle positions on the dicing streets and on the guard rings as black marks.
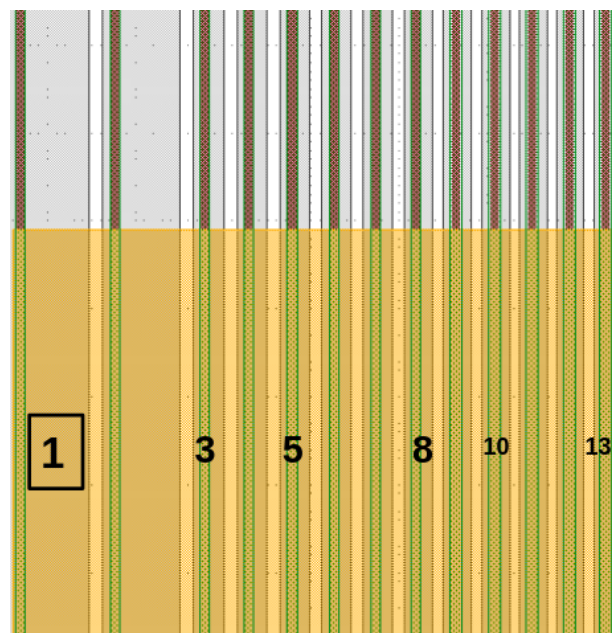
Figure 5.4: Schematic view of the 13 guard rings of the pixel sensor 11 (331831-21), provided by the graphic software *klayout*, with indicated the number of the guard ring. The orange band is the opening in the passivation layer, the metal is in gray.

broadest guard rings (1,2) are at the outermost part of the sensor with width $\sim$46 μm and the smallest are the innermost ones with a width of $\sim$12 μm. In Figure 5.4, the orange band indicates the opening in the passivation, while the metal is in gray.

E4control does not provide software for the guard ring measurements. Therefore a python software has been developed to take the voltage measurements on the guard ring. The guard rings measurements on the pixel sensor 11 (Figure 5.5) are taken applying a bias voltage in the voltage range U_{set} = (-5, -400) V, with a step width of 10 V, and the current limit set to 10 μA. Each measurement is directly plotted in the graph without error bars, because the first goal is to build and verify the experimental setup.

The guard ring structure is investigated from the outermost guard ring to the innermost, in the opening. In the Figure 5.5, the voltage measured U_{meas} for each of the 13 guard rings in dependence of the bias voltage applied via the HV pad U_{set} is shown.
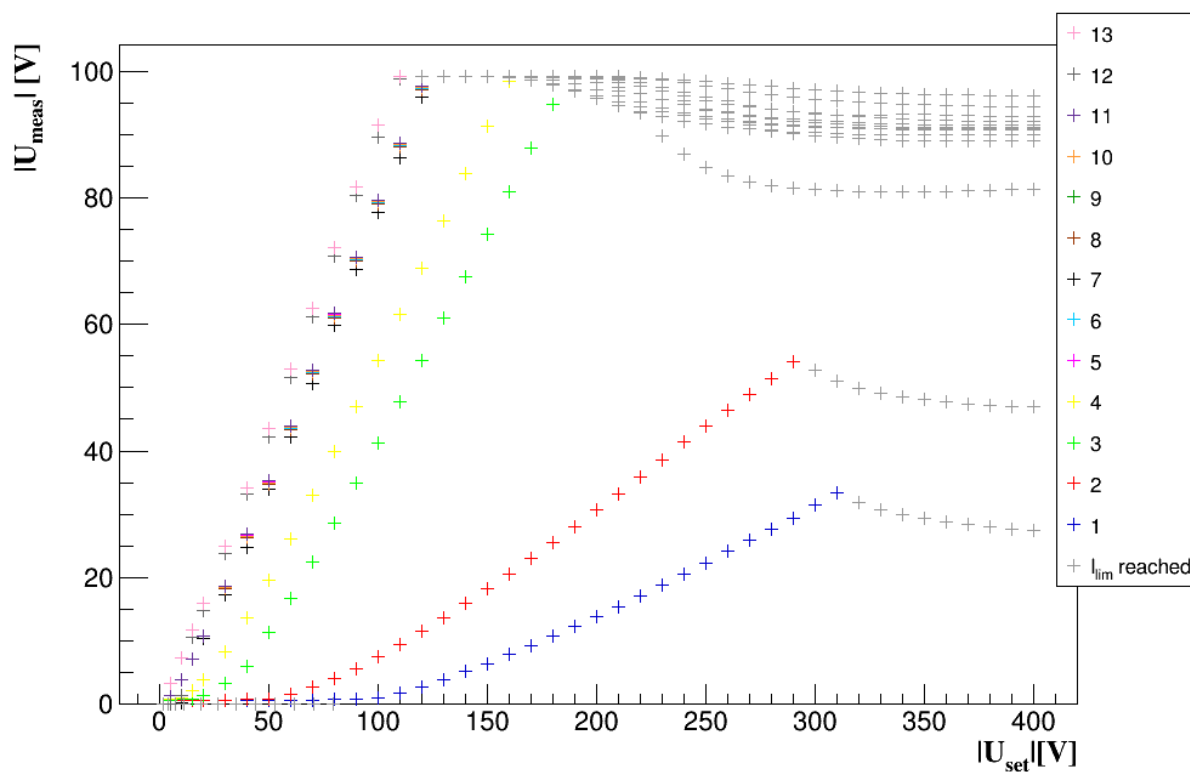
Figure 5.5: Measured voltage on the guard ring structure of the pixel sensor 11 (331831-21) at different bias voltage; with contact in the opening. The light gray cross, departing after the "kink" of each guard ring curve, indicates the measurements given by the multimeter after reaching the current limit of 10 μA.

Since the multimeter is measuring the voltage between the guard ring and the ground,

the measured potential is influenced by the number of guard rings in between the HV pad and the guard ring under test. For this reason, the innermost guard ring (the 13th, pink crosses in the figure) shows the smallest voltage difference from the bias potential. As expected, the guard rings 1 and 2, farthest from the HV pad but closer to the dicing streets of the sensor, have almost zero potential until, respectively, $\sim$100 V and $\sim$60 V. The dicing streets are measured to be at zero potential. The other guard rings show a behaviour in between the innermost and the outermost guard ring.

A "kink" is clear visible in the curves: for the guard rings from 3 to 13, the kink is at almost $U_{set} = (100 - 150)$ V, while for guard ring 1 and 2 it is at $\sim(280 - 300)$ V. The points after the kink of each guard ring are marked in light gray. As indicated in the legend, this kink indicates the point at which the current limit is reached, thus the voltage is lowered down by the source meter in a way that the current limit is not reached anymore.

However, before the kink, the guard rings fulfil their role, since the voltage measured on them decreases with distance from the HV pad and the number of guard rings in between. The outermost guard ring is about 0 V until a bias voltage of $\sim$100 V. Therefore, the bias voltage is completely reduced. After this point, there is still a high reduction of the bias voltage (reduction of about 90% at 300 V, because only $\sim$30 V are measured). Thus, the guard rings are properly working, but the current limit for the bias voltage has to be set in a way that it does not influence the measurements.

Cross-checks

To check that the sensor properties do not change by contacting the guard rings with a needle, three different sets of measurements are performed. Each set consists of measurements for all guard rings, in the opening, starting from the outermost to the innermost guard ring. These sets are labelled in chronological order: I, II, III, with the set II being the measurements shown in Figure 5.5.

Only the comparisons of the guard rings 1, 2, 4 and 11 are shown, in Figure 5.6. The behaviour of the guard rings 1 and 2 (Figure 5.6a and Figure 5.6b) seems to be affected by the repetition of the measurement. While the measured voltage of the guard ring 1, for the set I, is at zero potential until $\sim$200 V, this zero potential is only measured until $\sim$50 V in the measurement set III. The same behaviour is visible for the guard ring 2: the measured voltage for the set I is at zero potential until the bias voltage of $\sim$100 V, but for the measurements of set III, the zero potential can only be measured on the guard ring 2 until $\sim$10 V. The behaviour of the other guard rings, instead, do not seem to be so different among the three sets but it is possible to see small differences as the curves are not perfectly superimposed. These small difference in the absolute measured voltage of the guard rings can be traced back to temperature, contacting or other systematic effects.

IV curves of this sensor before and after the guard ring measurements are compared

(a) Guard ring 1.

(b) Guard ring 2.

(c) Guard ring 4.
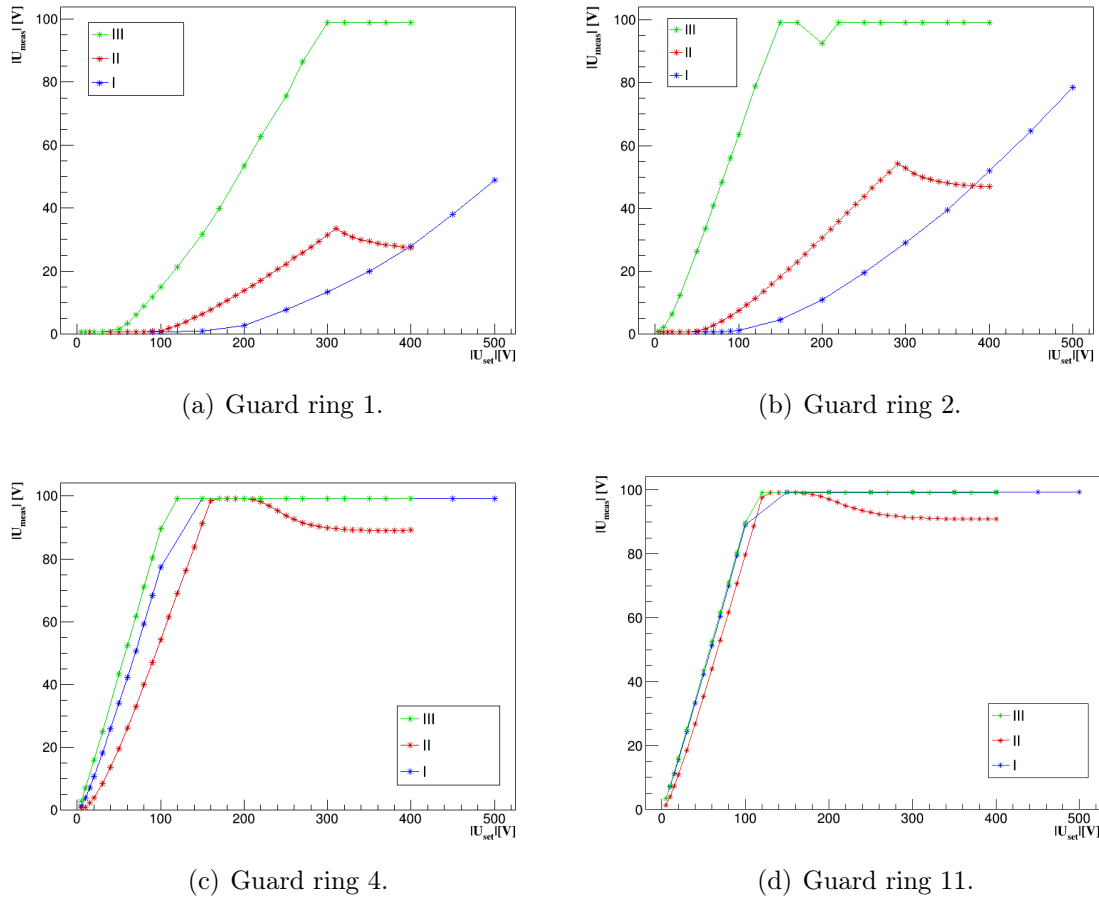
(d) Guard ring 11.

Figure 5.6: The three set of measurements I, II, III taken, in chronological order, for the guard ring 1, 2, 4 and 11 of the pixel sensor 11 (331831-21).

in Figure 5.7. The three sets of guard ring measurements are indicated with I, II and III, and "Before" is the IV curve measured before any guard ring measurements. As can be clearly seen, the breakdown voltage of the sensor is clearly decreased from ∼400 V to ∼80 V (reduction of 80%). Therefore the measurements on the guard rings change the electrical properties of the sensor significantly.

As a second cross-check, guard ring measurements of the diode 22 on the wafer piece 331831-21 are performed. The diode is shown in Figure 5.8, with a zoom in the area of measurements, in the opening and no-opening region. It has a 16 guard ring structure that can be seen in Figure 5.9, with the width of each guard ring shown in Table D.1 (Appendix D). Figure 5.10 shows the guard ring measurements performed on this sensor contacting the needle in the opening, with the same method already explained for the pixel sensor, going from the outermost guard ring inwards of the sensor. The bias voltage
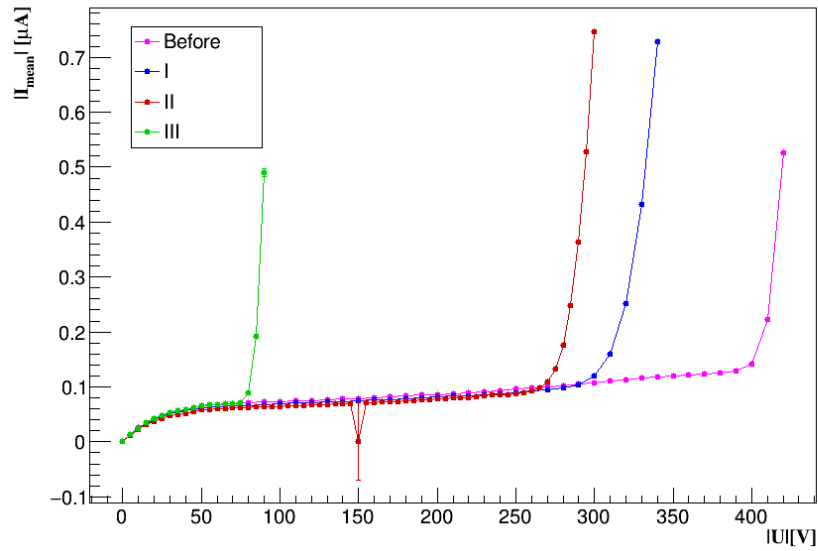
Figure 5.7: IV curves of the pixel sensor 11 (331831-21) taken before (magenta line) and after the I, II, III set of measurements (blue, red and green line).
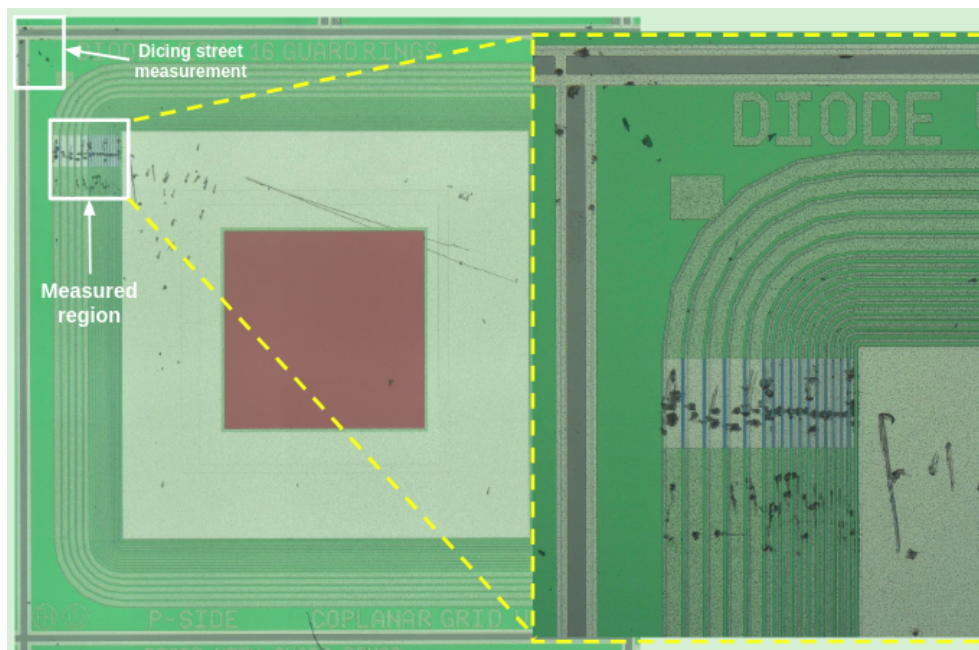
Figure 5.8: The diode 22 on the wafer 331831-21 showing the needle positions on the dicing streets and on the guard rings as black marks.
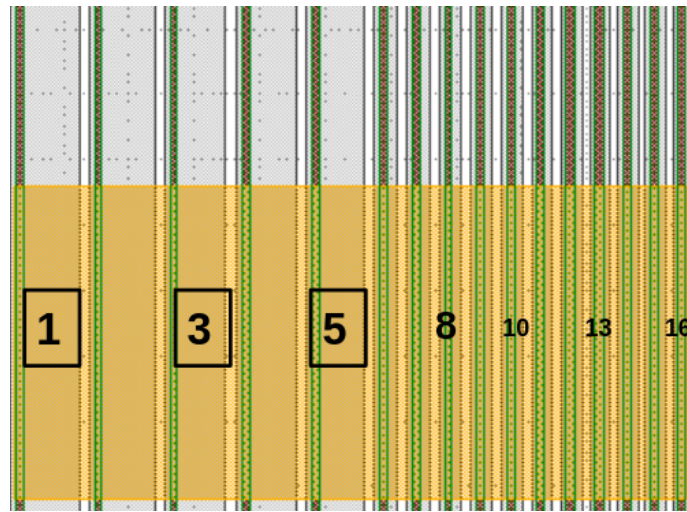
Figure 5.9: Schematic view of the 16 guard rings of the diode 22 (331831-21), provided by the graphic software *klayout*, with indicated the number of the guard ring. The orange band is the opening in the passivation layer, the metal is in gray.
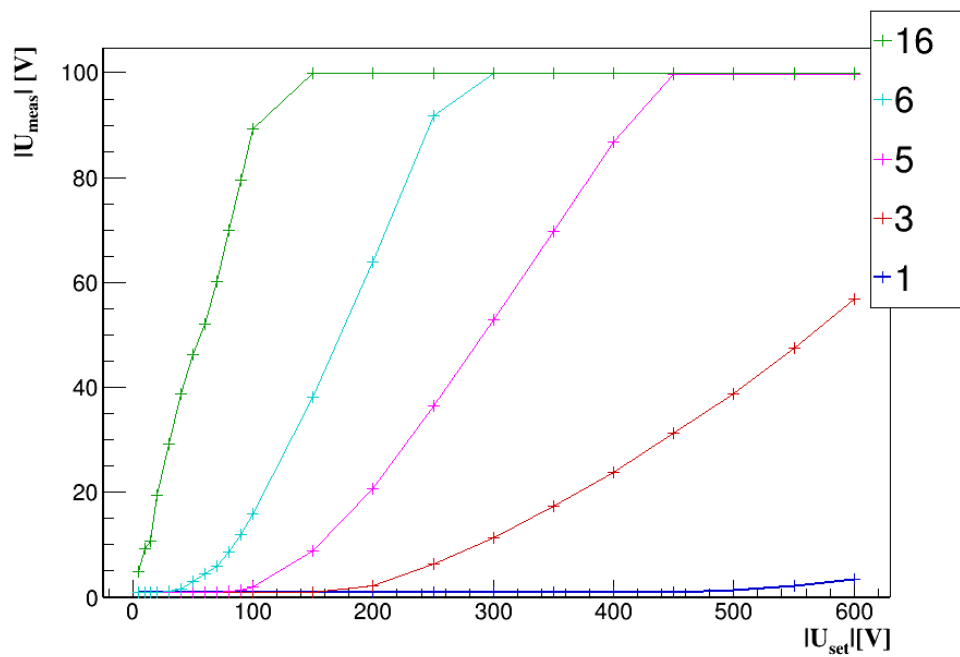
Figure 5.10: Voltage measured on the guard ring structure of the diode 22 at different bias voltage, contact in the opening.

is applied in the voltage range U_{set} = (-5, -600) V, with a step width of 10 V until -100 V and a step width of 50 V until -600 V. The current limit set to 10 μA.

Guard ring 1 has almost zero potential in all the voltage range, while guard ring 2 until ~180 V. Going inwards of the sensor, the other guard rings show similar behaviour as seen in Figure 5.5, reaching, at different bias voltage value, the limit of 100 V due to the current limit.

IV curves of the diode before and after the guard rings measurements are shown in Figure D.1 (Appendix D). The breakdown voltage of the sensor is clearly decreased from ~460 V to ~340 V (reduction of ~30 V). Thus, as for the pixel sensor 11, also the electrical properties of the diode 22 change after the guard ring measurements.

5.1.2   Improvements of the setup

During the guard ring measurements, the current is also registered by the multimeter. Figure 5.11 shows the IV curves monitored during the measurement of each guard ring. Since these measurements are registered by the same software used for the guard ring measurements, the current measurements are directly plotted on the graph (the IV curves logged with the software *IVmeas* are mean values of n measurements performed at each voltage step).
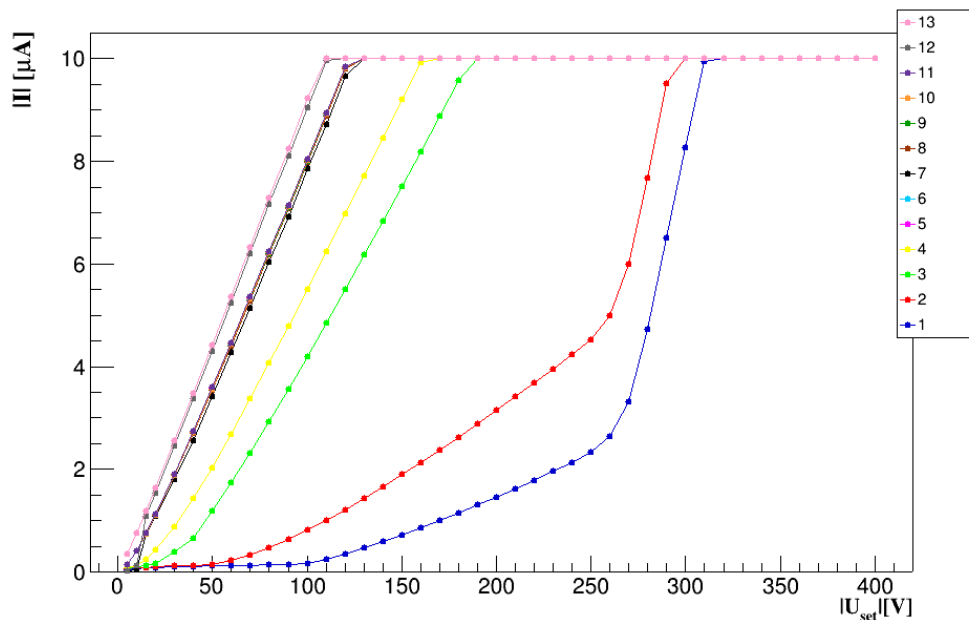
Figure 5.11: IV measurements taken during the measurement of each guard ring of the pixel sensor 11 of the wafer 331831-21.

The almost ohmic behaviour of the curves can be attributed to the low impedance of

the *Keithley 2000* with respect to the sensors investigated. The resistance of the sensors can be calculated from their IV curve taken before the guard ring measurements:

$$R(\text{sensor}) = (2040 \pm 20)\,\text{M}\Omega \tag{5.1}$$

$$R(\text{diode}) = (11400 \pm 280)\,\text{M}\Omega \tag{5.2}$$

Both values are significantly higher than the $1\,\text{M}\Omega$ of impedance of the *Keithley 2000*. Thus, when contacting the GR needle to the guard ring under test, the IV of the multimeter is logged instead of the current flowing through the sensor. For this reason, the multimeter *Keithley 2000* is replaced by the multimeter *K617*, which has an input impedance $> 200\,\text{T}\Omega$ and an extremely low input offset current that allows more accurate measurements. The drawback is the restricted voltage range of $(10\,\mu\text{V} - 200\,\text{V})$.

Since the *e4meas*-library does not provide the *K617* multimeter, it needs to be implemented in the library before starting the guard ring measurements with the software developed. Before its use, the *K617* requires to set the *zero check* and *zero correct* options to cancel any offset. The multimeter is used with the option *V, Ω Switch*, useful to speed up the response time of the instrument and to minimize the effects of leakage resistance. To use this option, the input of the multimeter is connected with a triaxial cable[1] to the GR needle and to the ground of the box, while the ground of the source meter is connected to the COM of the multimeter.

The GR needle is also replaced from a radius to a sharp tip (see Figure 5.12a,b). With a sharp needle tip, a better electrical contact with the metal of the guard ring is possible when the passivation needs to be pierced. In this way, a more stable and precise contact is achieved.
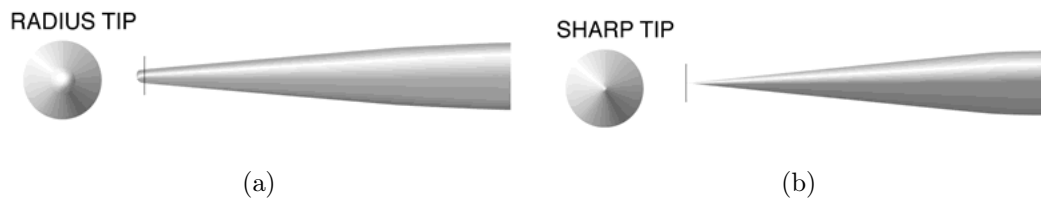
Figure 5.12: The two types of needle tips used [39].

5.1.3 Measurements on the Coplanar Diode

To investigate if the improvements of the setup with the multimeter *K617* is successful, the diode 22 (wafer 331831-21) is used. The microscopic image of the diode is shown in

---

[1]The *Model 6011* cable is made up of 3 feet of triaxial cable that is terminated with a triax plug on one end and 3 alligator clips on the other end.

Figure 5.8 and the 16 guard ring structure is shown in Figure 5.9, with the width of each guard ring listed in Table D.1 (Appendix D).

The guard ring measurements on the diode 22 are taken in the opening, from the outermost guard ring to the innermost, applying a bias voltage in the voltage range U_{set} = (-5, -190) V with a variable step: 5 V step until 20 V; 10 V step until 100 V; 20 V step until 190 V. The current limit is set to $10 \, \mu$A.

Figure 5.13 shows that the IV curves monitored during the measurement of each guard ring do not have a ohmic behaviour, meaning that the setup is measuring the current flowing in the guard ring.
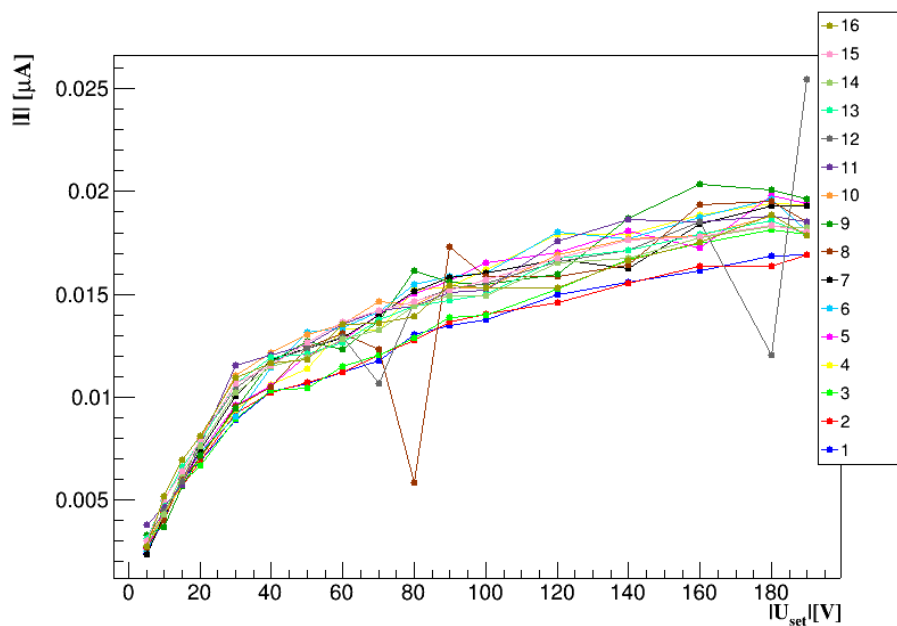
Figure 5.13: IV measurements taken during the measurement of each guard ring of the diode 22 of the wafer 331831-21.

In Figure 5.14 the scan of the measured voltage of the guard ring at different bias voltages is shown. Each measurement is directly plotted in the graph without the error bars. No kink can be seen in the curves since the current limit is not reached anymore, as can be also seen in Figure 5.13. The guard ring 1 (the outermost), together with the guard ring 2 and 3, is at almost zero potential until the end of the scan. In particular, guard ring 1 shows a potential of ∼3 V in the full voltage range. Since guard ring 3 is almost at zero potential, reaching a maximum of ∼12 V at $U_{set} = 190$ V, the two outermost guard rings 1 and 2 are not really necessary. Guard ring 4 and 5 (the outermost ones with larger width) measure ∼70 V at a bias voltage of 190 V (reduction of ∼60% of the bias voltage). Instead, the voltage measured at the innermost guard ring (16th) differs in a very small amount from the bias voltage (reduction of 6% of the bias voltage).
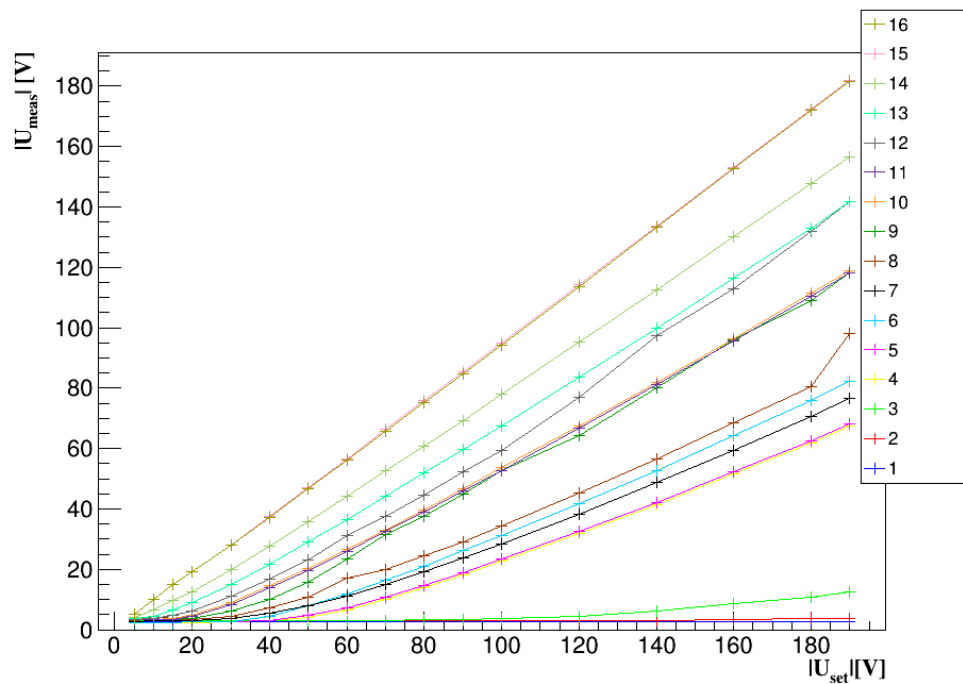
Figure 5.14: Voltage measured on the guard ring structure of the diode 22 (contact in the opening), with the multimeter *K617*.
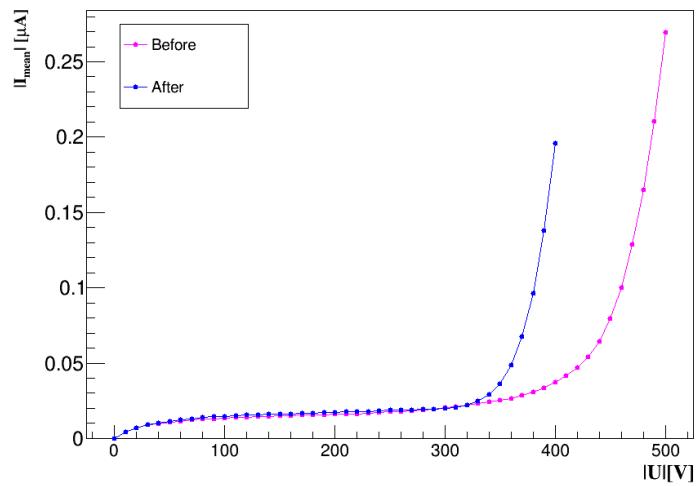
Figure 5.15: IV curves of the diode 22 (331831-21) taken before (magenta line) and after (blue line) the guard ring measurement.

The IV curves of the diode 22 before and after the guard ring measurements are compared in Figure 5.15. The breakdown voltage of the curve results reduced by $\sim$100 V after the guard ring measurements, therefore the sensor results irreversibly affected and damaged after contacting the guard rings.

Comparison between the measurements in the Opening and no-Opening

The goal is to measure the guard rings of the REINER sensors, which do not have openings in the passivation layer. Therefore, in order to understand if the measurements of the guard rings without the openings are possible and give reasonable results, tests are performed in the no-opening of the diode 22 of the same wafer 331831-21. The measurements in the opening of this diode are the ones shown in Figure 5.14.

(a) Guard ring 1

(b) Guard ring 2

(c) Guard ring 4
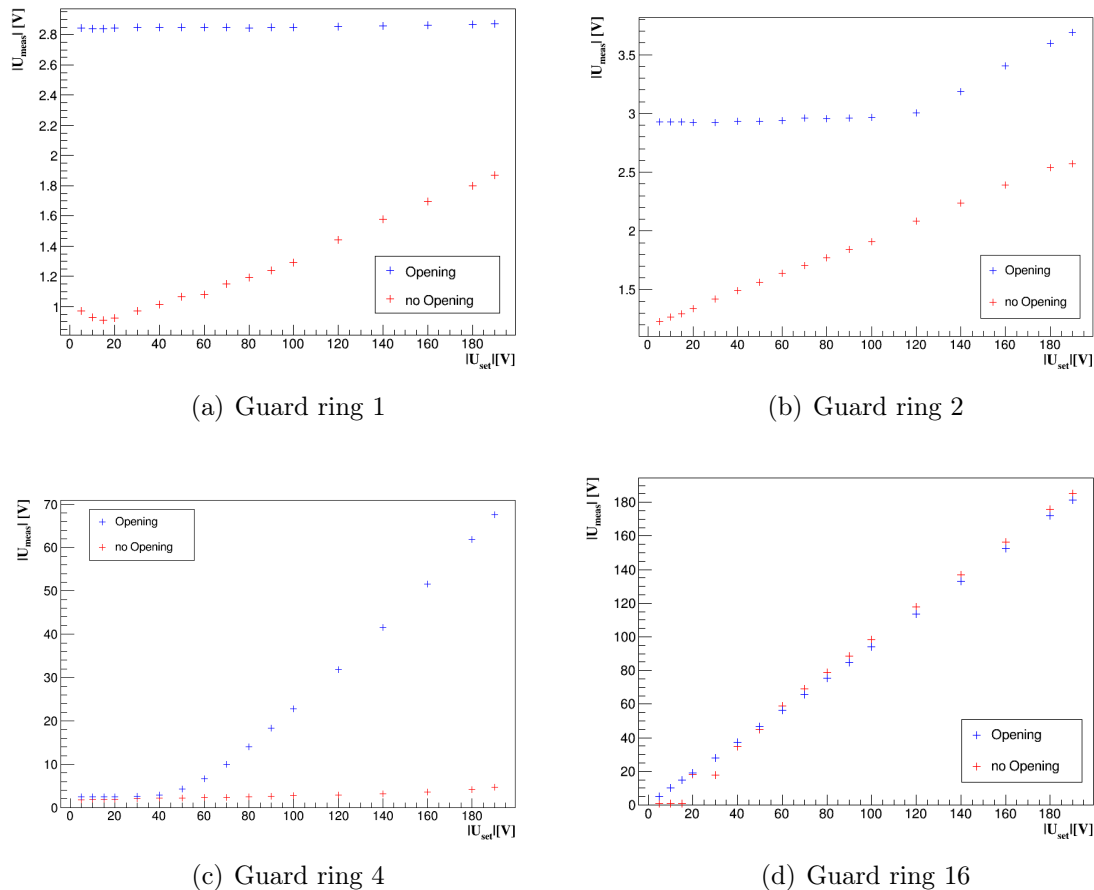
(d) Guard ring 16

Figure 5.16: Comparison between the guard ring measurements in the opening (blue cross) and in the no opening (red cross) of the guard ring 1, 2, 4 and 16 of the diode 22 (331831-21).

The comparison between the measurements of the guard rings 1, 2, 4 and 16 of this

diode, in the opening and in the no-opening, are shown in Figure 5.16, while the results for all the other guard rings are shown in Appendix D (Figure D.2, Figure D.3, Figure D.4).

The measured voltage in the opening is always higher than the voltage in the no-opening, except for Figure 5.16d (guard ring 16), which shows almost the same behaviour and a little higher voltage for the no-opening measurements. If the needle penetrates through the passivation perfectly, the metal of the guard rings should be contacted and the same behaviour should be obtained for the opening and no-opening measurements. Instead, if the needle in the no-opening measurement only contacts the metal partially or if there still is passivation between the electric contacts, a lower voltage is measured as the resistance of the passivation is higher than the one of the metal.

The results indicate that for the measurements of the guard rings 1, 2 and 4, the needle did not pass through the full passivation layer. Therefore, contacting the guard ring structure where there is no-opening in the passivation layer requires a further attention to check if the needle is really penetrating the layer of passivation and measuring the voltage on the guard ring.

5.1.4 Cross-checks with diode and pixel sensor from 331831-22

As a cross-check of the results obtained on the diode 22 of the wafer 331831-21, guard ring measurements are performed on the diode 22 (Figure 5.17) and the pixel sensor 11 (Figure 5.18) of the wafer 331831-22, which are in the same position on the wafer layout as 331831-21 but a different wafer.

The methodology followed these steps:

A. IV curves of the diode 22 and the pixel sensor 11, in order to check their functionality and receive a reference measurement before the guard ring measurements;

B. measurement of the high voltage applied on the HV pad (GR needle connected to the HV pad as well as the needle for the bias voltage);

C. guard ring measurements in the opening, starting from the outer guard rings towards the innermost ones;

D. re-check of the IV curve of the sensor;

E. guard ring measurements in the no-opening, from the outer guard rings towards the innermost ones;

F. dicing street measurements to check if they are grounded;

G. IV curve of the sensor;

The software used for the guard ring measurements calculates the mean value U_{mean} of five measurements and the error as the standard error ΔU_{mean}. Five measurements are considered for the calculation of the mean value because it is a good balance between the measurement time and a reasonable estimate of the error bars.

Only the guard ring measurements in the no-opening of the diode 22 (Figure 5.17) and the pixel sensor 11 (Figure 5.18), on the same wafer 331831-22, are shown, since they look similar to the ones in the opening (shown in Figure D.5a for the diode and Figure D.5b for the pixel sensor, in Appendix D). Only a small difference can be noticed between the two measurements, and in the most cases the two measurements overlap. As a result of the developed methodology, a good electrical contact to the guard rings can be obtained by piercing the passivation layer with a probe needle.
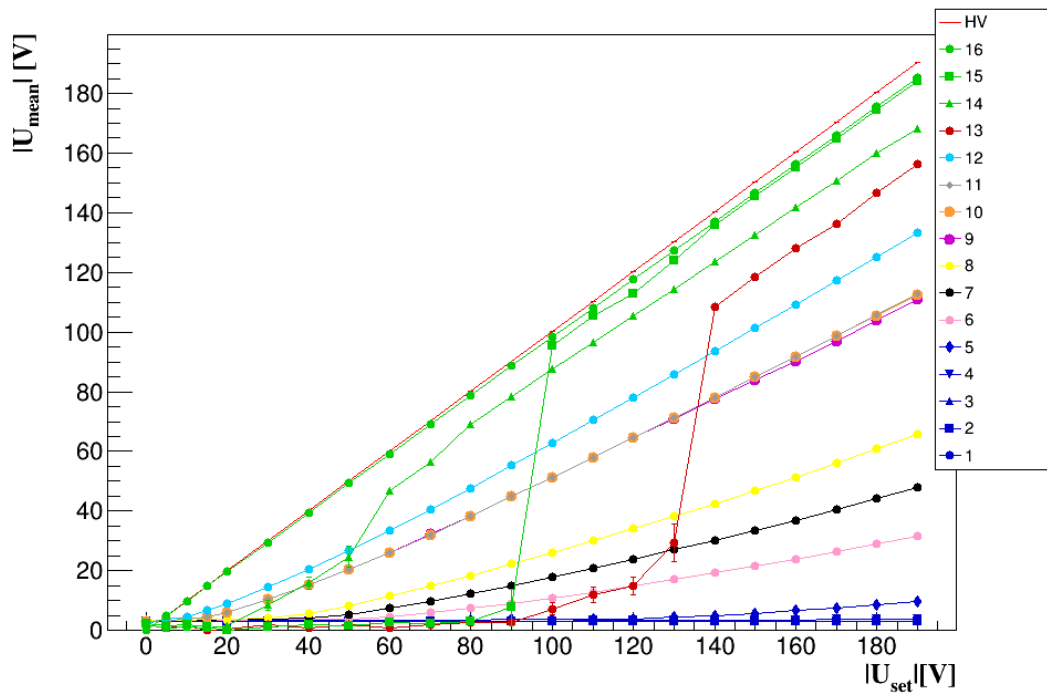
Figure 5.17: Guard ring measurements of the diode 22 (wafer 331831-22) in the no-opening.

In the Figure 5.17, the smallest and broadest guard rings are indicated with the same color (green = smallest, blue = broadest), but different markers are used for identification. The measurements of the guard rings 9, 10 and 11 on the diode 22 (Figure 5.17) are superimposed, therefore different size and type of markers are used to visualize them in the plot. The reason of the overlap is due to difficulties in positioning the needle and to target these only $\sim$16 μm wide guard rings, separated only by $\sim$5 μm. Thus, the measured results are probably not of different guard rings but all three of the same guard
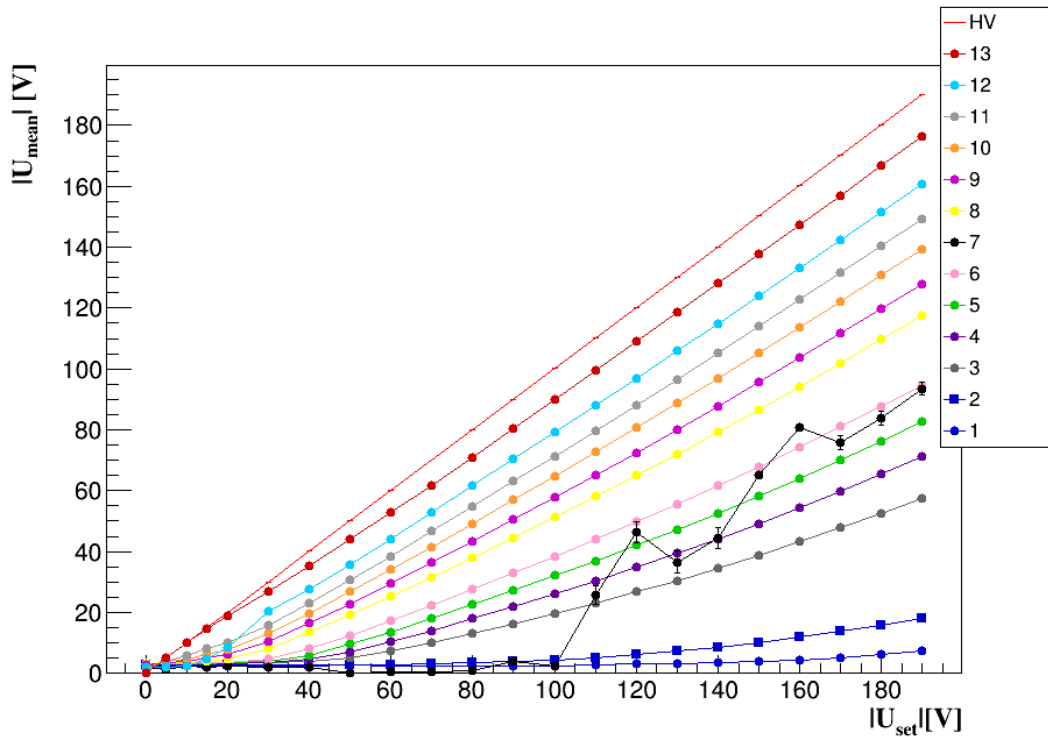
Figure 5.18: Guard ring measurements of the pixel sensor 11 (wafer 331831-22) in the no-opening.

ring.

The curves of the guard rings 13 and 15 in Figure 5.17 and the measurement of the guard ring 7 in Figure 5.18 show a different behaviour than all the other curves. A loss of contact or movement of the needle between the guard rings might have caused these visible discrepancies. Except for guard ring 7, the measurements on the pixel sensor 11 show the expected behaviour.

The comparison between the IV curves before and after the guard ring measurements is shown in Figure 5.19 and Figure 5.20 respectively for the diode 22 and the pixel sensor 11. In the legend, the step of the previous list, at which the IV measurement is performed, is indicated.

The IV curves of both sensors, the diode 22 and the pixel sensor 11, result strongly related to the measurement of the guard rings. But the effect is different: for the diode, an increase in leakage current over all voltages can be recognized with increasing guard ring measurements, while for the pixel sensor, a drastic reduction of the breakdown voltage ($\sim$200 V) is visible with more guard ring measurements. The breakdown voltage of the diode, instead, changes from $\sim$20 V to $\sim$80 V.

The IV curves "history" showed that any contact to the guard rings with the needle
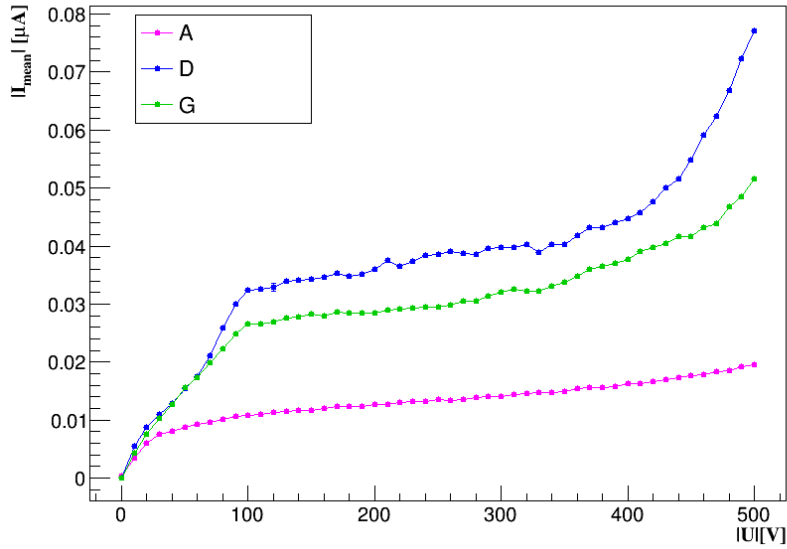
Figure 5.19: Comparison among the IV measurements of the diode 22 (331831-22) before and after the guard ring measurements. The legend refers to the steps in the method list.
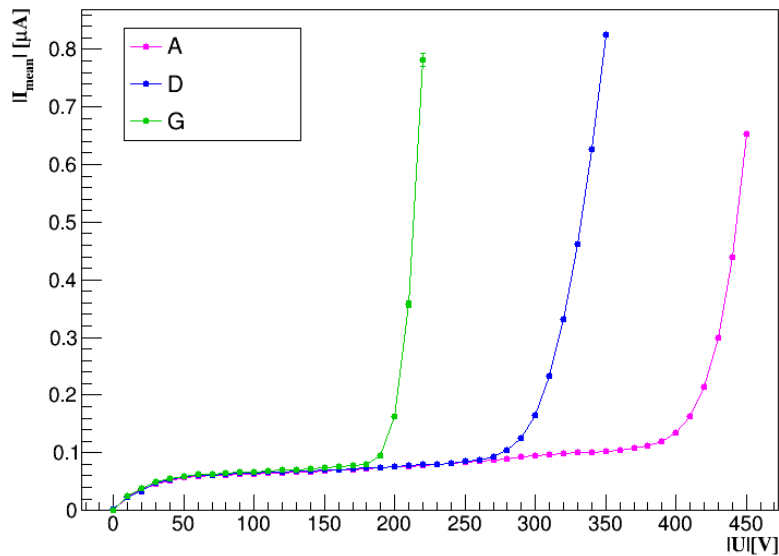
Figure 5.20: Comparison among the IV measurements of the pixel sensor 11 (331831-22) before and after the guard ring measurements. The legend refers to the steps in the method list.

has consequences for the sensor properties. Therefore, the number of guard ring measurements should be limited on the minimum possible in order to preserve the performances of the sensor.

5.2   Guard ring measurements on the REINER sensor

The guard rings of the REINER sensor 310894-22 are measured with the same methodology explained in 5.1.4. The guard ring measurements of the pixel design V5 is shown in Figure 5.21, including the measurements of the HV pad (red line). Each voltage value is the mean number of five measurements and is plotted with its error, calculated by the program using the standard error ΔU_{mean}. As can be seen, the voltage measured on the guard rings decreases with higher distance from the HV pad. The guard ring are well contacted individually, since no contact loss can be observed in the plot.
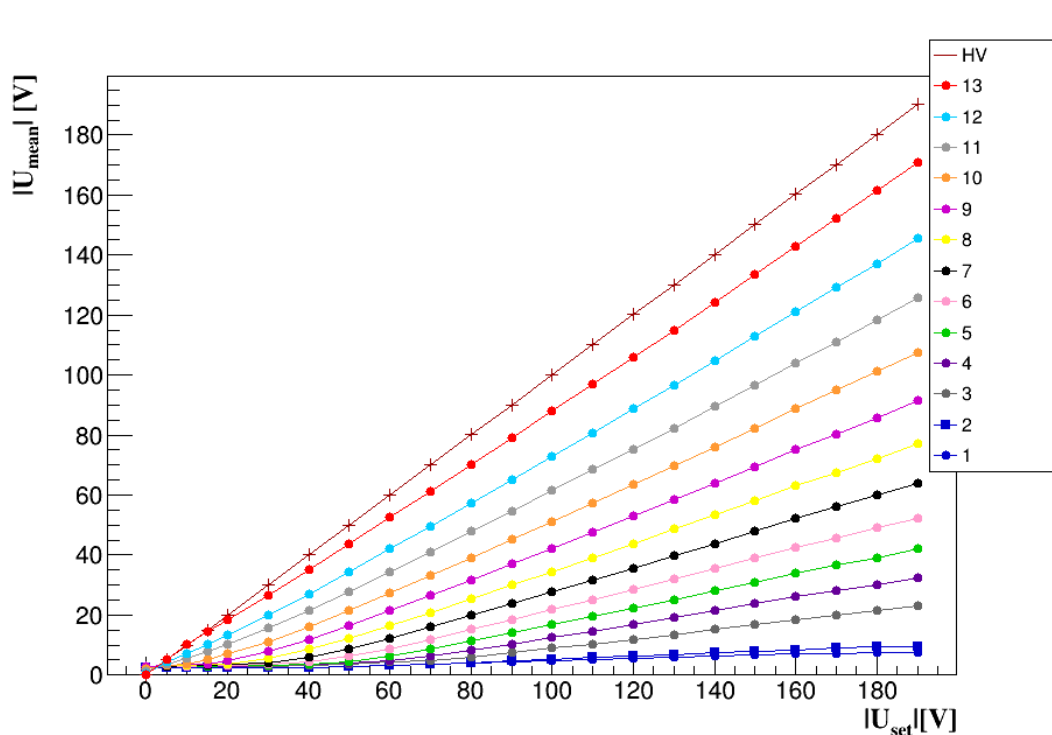
Figure 5.21: Guard ring voltage measurements on the pixel design V5 of the REINER sensor 310894-22.

The same blue color but different markers, are used for the two largest guard rings (1,2) of the multi-guard ring structure. These two guard rings measure a potential between $\sim(2 - 9)$ V, but no zero potential is measured on the guard ring 1, neither on

2. The dicing streets are checked to be at ground potential. The innermost guard ring (13) does not differ more than 1% from the values measured on the HV pad.

The guard ring measurements of the other pixel designs are not shown since they look really similar to the measurements of V5. This confirms that the multi-guard ring structure of each pixel design on the REINER sensor is properly working and that the methodology developed allows to contact the guard rings by penetrating in a proper way the passivation layer.

(a) Guard ring 1

(b) Guard ring 2

(c) Guard ring 9
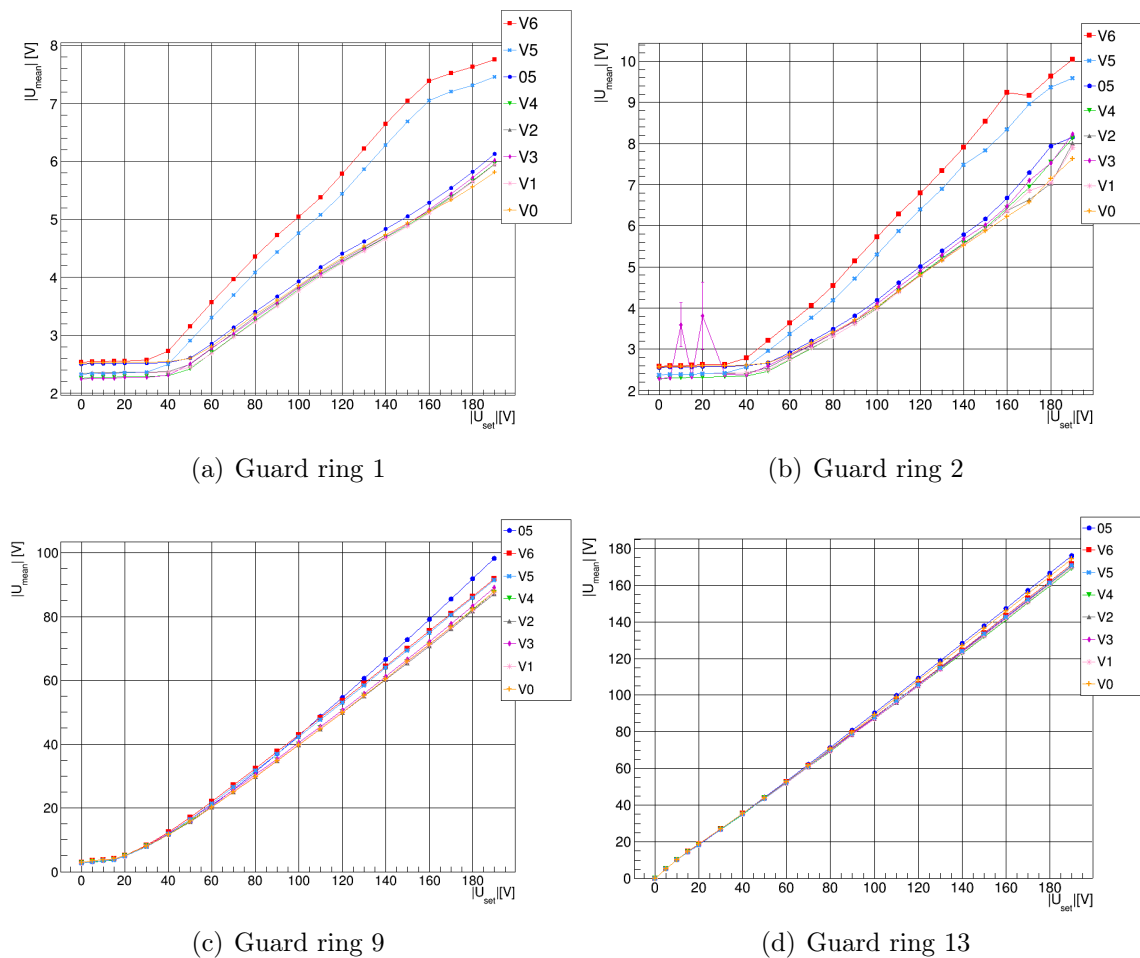
(d) Guard ring 13

Figure 5.22: Measurements taken on the guard ring 1, 2, 9, 13 for the eight designs of the REINER sensor 310894-22.

One way to investigate the guard ring structures of the pixel designs is to look at the measurements taken for a specific guard ring of different designs. Figure 5.22 shows the results for the guard rings 1,2 as the outermost, the guard ring 9 as a guard ring in the center, and the guard ring 13 as the innermost, taken for the eight different pixel designs

of the REINER sensor 310894-22. The measurements of the other guard rings are shown in Appendix D (Figure D.6 and Figure D.7).

The measurements of the outermost guard ring 1, 2 have a different behaviour for the pixel design V5 and V6, while the measurements of the other guard rings, in different pixel designs, behave similarly. The scale on the y-axis is different among the guard rings. Two kinks can be noted for guard ring 1 and 2 (Figure 5.22a,b). At $U_{set} = 40\,\text{V}$ for both the guard rings 1 and 2, while the second kink at $U_{set} \sim 180\,\text{V}$ is more visible for guard ring 1. The first kink can be related to the value of the depletion voltage which is $\sim 30\,\text{V}$, while the second kink for the design V5 and V6 can be related to the breakthrough ($\sim 170\,\text{V}$), as can be seen in the IV curves in Figure 4.15.

The measured voltage of the guard ring 1 and 2 is at $\sim 2.5\,\text{V}$ until $U_{set} = 40\,\text{V}$. Then, the voltage on guard ring 1 increases reaching a maximum value of $\sim 8\,\text{V}$ for the designs V5 and V6, and $\sim 6\,\text{V}$ for all the other designs, while on guard ring 2 a maximum value of $\sim 10\,\text{V}$ is measured for the designs V5 and V6 and $\sim 8\,\text{V}$ for all the other designs.

The higher voltages reached by the designs V6 and V5 can be related to their higher flow of leakage current with respect to the other designs (IV curves in Figure 4.15). As can be seen comparing also the measurements on the other guard rings shown in Figure D.6 and Figure D.7 (Appendix D), going inwards of the sensor, namely getting closer to the HV pad, the measurements for all the different pixel designs group together and are not significantly distinguishable anymore.

5.2.1 Influence between Different Designs

The influence among different pixel designs in the REINER sensor is investigated by applying the bias voltage on one pixel design and measuring the guard rings of another structure. The different combinations analysed are listed in Table 5.1

Biased design	Measured design
05	V0
V0	05, V1, V2, V5, V6
V1	V0
V2	V0, V3, V4, V5
V6	V0
V3	V2
V4	V2
V5	V2

Table 5.1: Combinations of biased design and guard ring measurements of the other design for the REINER sensor 310894-22, used to study the influences among them.

An example of the results of this measurement is given in Figure 5.23, where the bias voltage is applied on the design 05 and the guard rings of the design V0 are measured.

They have the same pixel layout and with this combination the most distance between the applied voltage and the measured voltage of the guard rings is reached (they are placed at the opposite side on the REINER sensors, see Figure 3.10).

The bias voltage is applied in the range $U_{set} = (0, -500)$ V with a step of 10 V. The voltage range is enlarged until -500 V because, when measuring the guard rings potential of a design not biased, it is not expected to measure any voltage if the guard rings of any structure are working properly. Therefore the voltage measurements should not exceed the *K617* multimeter range (10 μV - 200 V). Instead, for the previous measurements, when the guard rings of a biased design are measured, the maximum set voltage allowed with this multimeter is 190 V, since it is expected that the innermost guard ring has a voltage closer to the voltage applied on the HV pad (e.g. see Figure 5.21).
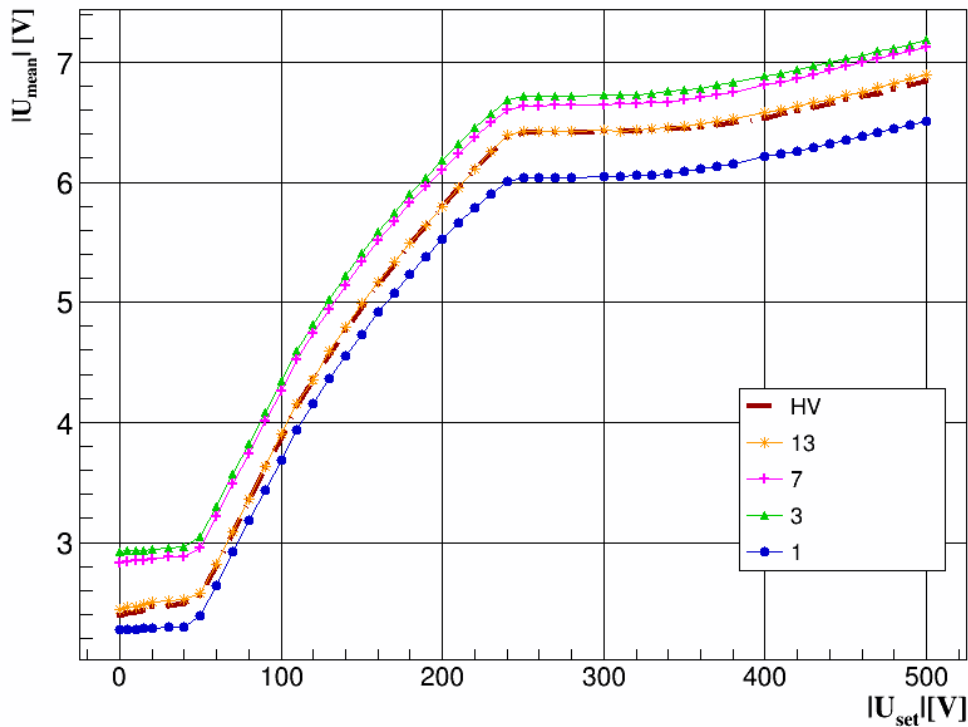
Figure 5.23: The measurements of the guard ring structure V0, biasing the pixel design 05, of the sensor 310894-22.

Not all the guard rings of the V0 design are measured in Figure 5.23 in order to reduce the measurement time. Five minutes are approximately needed to scan one guard ring[2]. Guard ring 1, 3 and 7 (as inner guard rings), and 13 are measured. The curves have a

---

[2]The measurement time is a rough estimate that considers the time of positioning of the needle on the guard ring under test and initialization of the measurement software.

similar behaviour among each other. Two kinks are visible, at (40 - 50) V and $\sim$240 V. As for the plots in Figure 5.22, the first kink may be related to the reaching of the depletion voltage of the sensor, while the second one may be due to the breakthrough of the most structures (see the IV curves shown in Figure 4.15 and Figure 4.16).

Guard ring 1 is at the lowest voltages in all the range, while the inner guard rings 3 and 7 reach higher voltages in all range. The innermost guard ring (13) completely overlaps the voltage measured on the HV pad of the design V0 (brown thick line labelled as "HV") in all range.
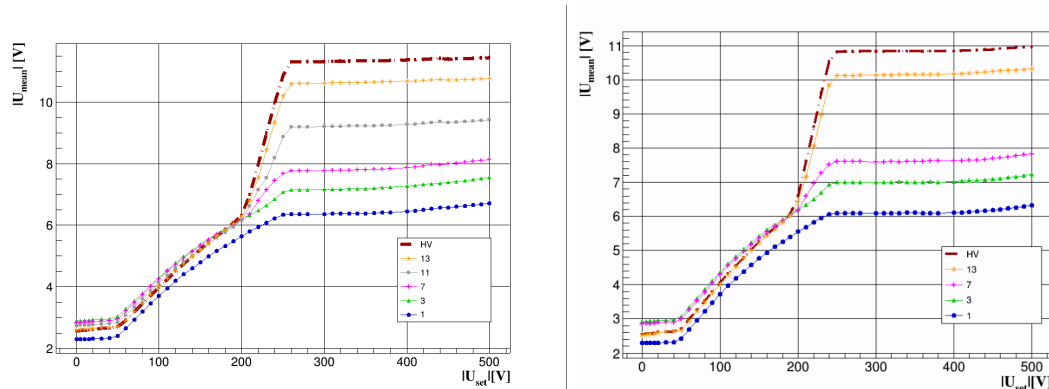
(a) Bias on V0, GR of V5

(b) Bias on V2, GR of V5
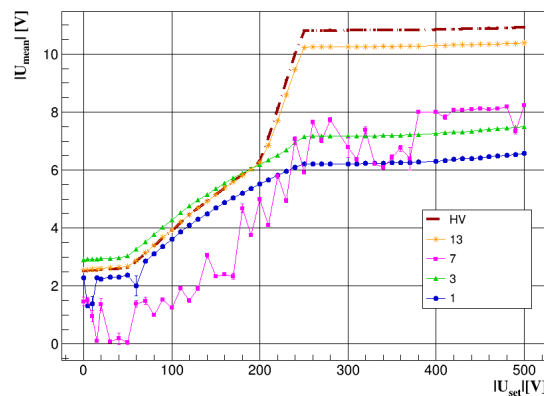
(c) Bias on V0, GR of V6

Figure 5.24: Upper images: measurements on the guard ring structure of the design V5, biasing the design V0 (a) and the design V2 (b). Bottom image: measurements on the guard ring structure of the design V6, biasing the design V0.

Since a non-zero voltage is measured on the guard rings structure of the design V0 while the bias voltage is applied on the design 05, it may be concluded that the different designs on the REINER sensor influence each other. Either the guard ring structure of

the design V0, or of the design 05, or of both, is not properly working. Moreover, the inner guard rings 3 and 7 show a completely unexpected behaviour, having the highest voltage values in all range instead of showing voltages in between the innermost guard ring 13 and the outermost 1, like in Figure 5.21.

A similar behaviour is registered for the reverse combination (biasing V0 and measuring 05) and for all the other combinations listed in Table 5.1, shown in Figure D.8 and Figure D.9 (Appendix D). Only the measurements of the guard rings of design V5 and V6 show a different behaviour than the other measurements independent of the biased structure.

In Figure 5.24a and Figure 5.24b, the measurements on the guard rings of the design V5, biasing respectively the design V0 and V2, are presented, while in Figure 5.24c the measurements of the guard rings of V6 (V0 biased) are shown. In all three cases, the HV pad measures a voltage of (10.5 - 11) V and is followed by the measurements of the guard rings in sequential order of their local position: the lowest voltages for the outermost guard ring (1) and then increases towards the structure center. This behaviour seems a feature related on the guard ring structures of the design V5 and V6, since it does not depend on which other design the bias voltage is applied. The remarkable measurements of the guard ring 7 in Figure 5.24c are clearly traced back to loss of contact between the needle and the guard ring.

For completeness, the IV curves before, after the first and second guard ring measurements of the designs V0 and V4 of the REINER sensor 310894-22 are shown respectively in Figure 5.25a and Figure 5.25b

(a) Design V0 (b) Design V4
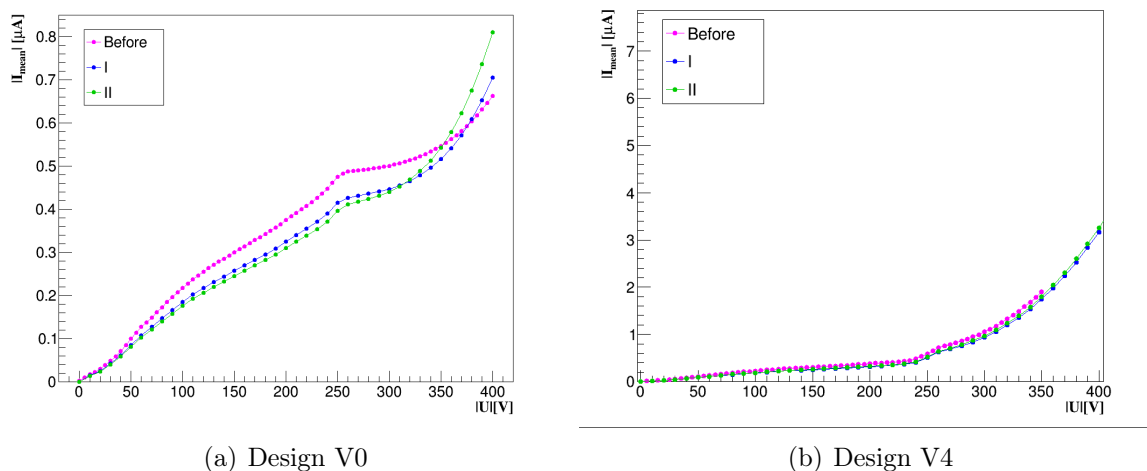
Figure 5.25: Comparison among the IV curves of the design V0 (a) and V4 (b) taken before and after the guard ring measurements. "I" indicates the first guard ring measurements and "II" indicates the measurements taken to test the influence among the different designs.

The design V0 shows an overall decrease of the leakage current at all voltages after the guard ring measurements, while the design V4 does not show a significant change that can be caused by temperature, contacting or other systematic effects. These two designs are taken as an example since the other designs show similar behaviour to these. This means that the guard ring measurements did not damage the sensor 310894-22 and can be considered as a validation of the methodology used for the guard ring measurements.

5.2.2 Measurements on the assembly on PCB

To check if the unexpected measured behaviour of the guard rings structure is due to the non-ideal contacts of the pixels with the chuck, the guard ring structure of the assembly listed in the last row of Table 4.1, and shown in Figure 3.13, is investigated. The difference in the setup is that, using an adaptor for the biasing of the structure (which is placed where the jumpers are indicated), the "HV needle" is not needed anymore, and the structures are biased using LEMO connectors. The voltage on the guard rings is measured with the GR needle.
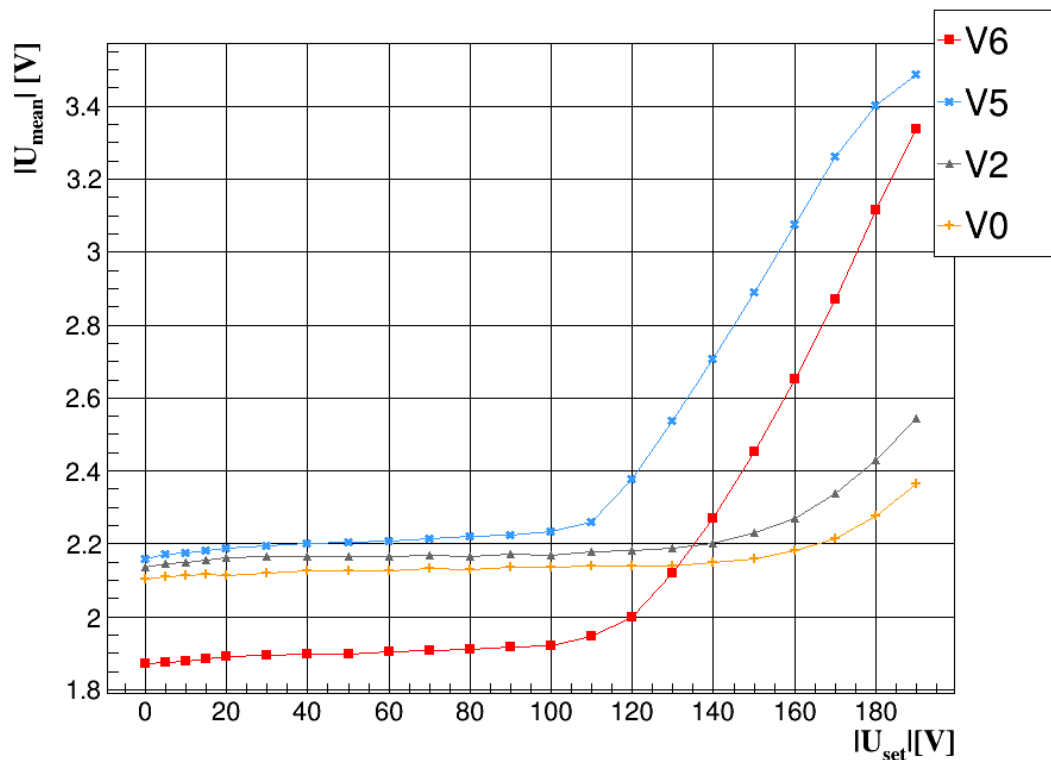
Figure 5.26: Measurements taken on the guard ring 1 for the design V6, V5, V2 and V0 of the assembly.

Not all the guard rings of each design are measured, but only the guard rings 1, 7, 11 and 13, since the behaviour confirmed what already measured for the REINER sensor 310894-22. The guard ring measurements of the pixel design V2 of the assembly are shown in Figure D.10 in Appendix D. The measurements on the guard ring 1 of the design V6, V5, V2 and V0 are shown in Figure 5.26.

As already seen in Figure 5.22a for the bare REINER sensor, the guard ring 1 measurements of the designs V5 and V6 are separated from the other pixel designs. But for this assembly, V5 exceeds the measurement of V6, as can be also seen in the IV curves shown in Figure D.11 (Appendix D). Another difference from the measurement on the bare sensor is that the first kink is different among the designs: for the designs V5 and V6 it is at U_{set} ~120 V, while for the others it is at ~180 V. If this first kink is related to the value of the depletion voltage, the designs could show different values. The second kink is at ~180 V for the designs V5 and V6, that seems to be related to the breakthrough of these designs, looking at the IV curves in Figure D.11 (Appendix D). The second kink of the other designs (V0 and V2) is instead not visible in this range but it can be at higher voltages, when there is the breakthrough which happens at voltage larger than 400 V, as can be seen in the IV curves of Figure D.11. The absolute values at the beginning of the bias scan are comparable between the bare sensor and the assembly ~(2 - 2.5) V. Instead, the absolute values at the final set voltage are significantly different: ~7.5 V for V5 and V6 and ~6 V for the other designs of the bare sensor, ~3.4 V for the V5 and V6 and ~2.4 V for the other designs of the assembly.

Influence between Different Designs

The different combinations of biased design and guard ring measurements of another design, analysed for the assembly, are listed in Table 5.2.

Biased design	Measured design
V0	V2, V5, V6
V3	V2
V5	V6
V6	V0

Table 5.2: Combinations of biased design and guard ring measurements of the other design for the assembly on PCB to study the influences among them.

These measurements are more difficult to handle with the GR needle because of the presence of substructures on the PCB (the DATA box or the LV box, see Figure 3.13), which prevents the use of the GR needle in all the needed positions. Therefore the choice of the combinations is also driven by practical reasons.

The measurements on the guard rings of the design V2 biasing the designs V0 and V3 are respectively shown in Figure 5.27a and 5.27b, while 5.27c shows the guard ring

measurements on the design V6 biasing V0 (the reverse combination of the one shown in Figure 5.24c).

All the plots look very similar to each other. There is an overall slight increase of the measured voltage on the guard rings with higher bias voltage. The order of the values for the guard ring measurements is always the same (also for the bare sensor): the guard ring 3 is the highest, followed by 7 and 11. The values of guard ring 13 is always close to the ones of the HV pad, in the middle, while the values for guard ring 1 are always the lowest.

(a) Bias on V0, GR of V2

(b) Bias on V3, GR of V2

(c) Bias on V6, GR of V0
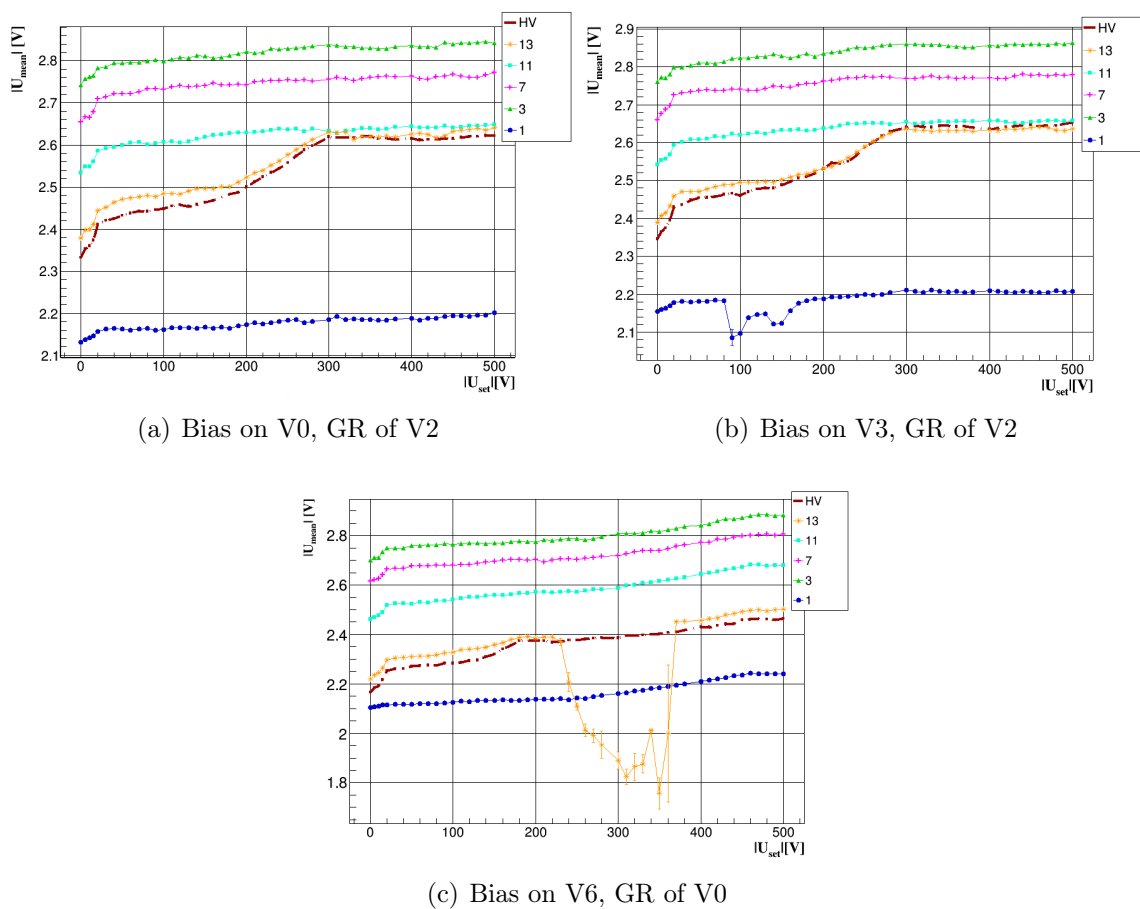
Figure 5.27: Upper images: measurements on the guard ring structure of the design V2, biasing the design V0 (a) and the design V3 (b). Bottom image: measurements on the guard ring structure of the design V0, biasing the design V6.

The HV pad of the pixel design V2 shows two kinks at a bias voltage of ~10 V and ~300 V (independent from which pixel design is biased, V0 or V3). The fact that the measured voltages for the guard rings of pixel design V2 are almost the same if V0 or V3

is biased, indicates that these measurements are independent from the distance between the biased design and the measured design (V3 is closest neighbour to V2, while V0 is furthest apart, see Figure 3.10). Therefore, if the results are independent from the biased design and only depend on the measured design, it is possible to compare Figure 5.27c with Figure 5.23, where the guard rings of the design V0 are measured while biasing the design 05: the absolute values are completely different and there are no prominent kinks visible, beside the very small one of the HV pad at $\sim 20\,\mathrm{V}$.

The measurements on the guard ring structures of the design V5 and V6 are shown in Figure 5.28.

(a) Bias on V0, GR of V5

(b) Bias on V0, GR of V6

(c) Bias on V5, GR of V6
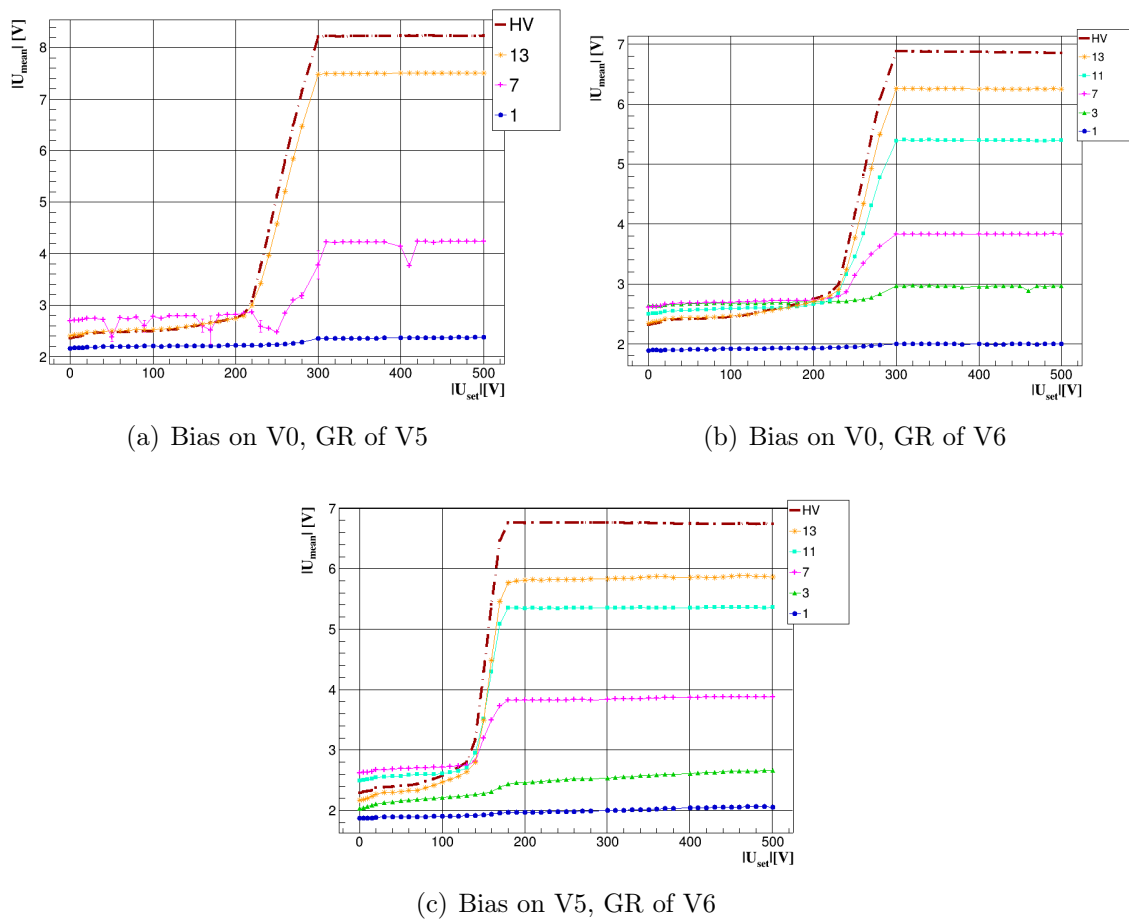
Figure 5.28: The measurements of the guard ring structure of design V5 and V6, biasing another design.

All these plots show the same order with the HV pad at the highest measured voltages, $\sim (7\text{ - }8)\,\mathrm{V}$. Then, the order of the guard rings follows, from the innermost towards the outermost ones. These measurements are comparable with the ones of the bare REINER

sensors of the designs V5 and V6 shown in Figure 5.24, but the highest measured voltages in the HV pad reach almost 11 V.

The shapes of all curves look similar, with a prominent increase in voltage and saturate after a specific bias voltage. Two kinks are visible. The first one is at $\sim$220 V for the guard ring measurements of the design V5 and V6 (V0 biased for both), and at $\sim$120 V for the guard ring measurements of the design V6 (V5 biased). This is in contrast to the measurements on the bare sensor shown in Figure 5.24, where the guard ring measurements are independent from the biased structure. In the assembly, the measurements show that the biased structure makes a difference, otherwise the Figure 5.28b and Figure 5.28c would look alike.

The results of the assembly look significantly different from the bare sensor, but it is not clear if it is an effect of the sensor or of the connection of the pixels to the FE changes the results. The absolute values are different as well as the position of the kinks. However, the order of the highest measured voltages of the guard rings is the same for the bare sensor and the sensor with the FE, for all the pixel designs. There is something special about the designs V5 and V6 because their order is in both cases different from the others.

Conclusion and Outlook

In order to study the electrical performance of the REINER sensors, different preliminary studies were performed for the development of the measurement methodology and the building of the experimental setup.

The investigation of the most important properties characterising the sensors, such as the leakage current and the depletion voltage, has been carried out using some test sensors. Also the scaling of the leakage current with temperature was considered since the changing of the conditions in the environmental setup affects the measurements. The results of the measured scaling have been compared and verified with the theoretical expectation given by the scaling law 2.10.

The full REINER sensors have been characterised by measuring the flow of the leakage current in the different pixel designs and their depletion voltages. A deeper investigation of the pixel designs was possible through the cutting of the individual designs from the full REINER sensor. The experimental setup had to be adapted to the smallness of these sensors. The comparison between the full and the cut sensors showed that the sensors completely changed their behaviour. The very early breakdown does not allow to use them in a proper way anymore. It has also been shown that the reason of this completely different behaviour of the cut sensors in the IV curves and CV curves cannot be traced back to higher resistance present at the cutting edges. However, it may be concluded that the cutting of the REINER sensors is not beneficial in any sense.

The systematic study of the multi-guard ring structure of sensors required the development of a new experimental setup as well as a new measurement software. The influence of the multimeter on the voltage measurements was the biggest problems of these measurements, since the analysed sensors have a very large resistance. Moreover, it is important to consider a proper penetration of the passivation layer, which otherwise can modify the results on the measured voltage, decreasing its value.

Test sensors have been used to verify the measurement methodology and the construction of the setup. The results on the coplanar diode and the pixel sensor of the wafer 331831-22 showed reliable results with the combined use of the *K617* multimeter (input impedance $> 200\,\mathrm{T\Omega}$) and a sharp tip needle (to penetrate the passivation layer in a better way). However, the guard ring measurements irreversibly affect the electrical properties of the sensors, which is clearly visible in the IV curves check perfromed at the

three fundamental steps listed in the method of Section 5.1.4.

With the developed method it was possible to investigate the 13 guard ring structure of each pixel design on the REINER sensor. The guard rings of each structure are found to behave as expected, with the innermost guard ring at the highest voltages close to the HV pad and the other guard rings going outwards the sensor at decreasing voltage values. Checking the behaviour of each guard ring in all the eight pixel designs, some unexpected results were found. The outermost guard rings 1 and 2 of the designs V5 and V6 are at higher voltages than the ones of the other designs in the full voltage range. This is related to the IV measurements of the REINER sensors, which showed that the designs V5 and V6 have an earlier breakdown and the highest leakage current, and can be due to the fact that the outermost guard rings of these designs do not prevent the flowing of leakage current as the ones of the other designs. Therefore, there is a larger contribute also coming from the surface of these sensors. The other guard rings, instead, behave in the same way for all the eight pixel designs, thus the difference found in the IV curves seems to be related to the behaviour of the outermost guard rings 1 and 2.

The influence between the pixel implantations has been further investigated by measuring the guard ring structure of a pixel design while biasing another structure. The results showed that the eight designs are electrically connected with their guard ring structures because a non-zero voltage is always present in the measured (but not biased) structure. Measuring any design except for the V5 and V6, the order of the guard ring is always the same: the third guard ring and the other inner guard ring measured (usually guard ring 7) at the higher voltages in all range, than the HV pad overlapping or close to the guard ring 13, and the outermost guard ring 1 at the lowest voltages. Therefore, the inner guard rings seem to behave in the most unexpected way with respect to the other guard rings.

For the designs V5 and V6, the measurement of the guard ring structure always gave the same results no matter which structure is biased. The order of the guard rings is different, with the HV pad of the measured structure at the highest voltage values in all range and then the other guard rings from the 13 to the outermost guard rings at decreasing voltages. Higher voltages are measured for the pixel design V5 when another structure is biased compared to the design V6.

The guard ring measurements on the assembly confirms that the unexpected measured behaviour were caused by a non-ideal contact of the pixels with the ground of the chuck. For the assembly, the measured guard ring voltages of all the designs were partially in agreement with the measurements for the bare sensor. The order of the guard rings was found to be the same: for the pixel design V5 and V6, the HV pad at the higher voltages in all range and the other guard rings from the innermost one to the outermost at decreasing voltage values; for all the other designs, the central guard ring 3 measures a higher voltage in all range, the outermost one at the lowest voltages and the HV pad with the innermost guard ring in the middle. However, the absolute values, at the highest bias voltages, measured for the assembly resulted smaller the ones measured

for the bare sensor.

The characteristic kinks present in the measured voltages of the bare sensor were smoothed in the assembly or even vanished. Since in general the guard ring measurements in the assembly showed smaller absolute voltage values than the ones in the bare sensor, an effect of the contacts between the pixels/chuck and the pixel/FE may be considered.

To understand the physical processes resulting in the reported unexpected results for the guard rings, TCAD simulations [40] are useful. With this tool, the full sensor and/or the different pixel designs can be simulated and the resulting electric field in the sensor investigated. Simulations of the guard rings might give an explanation for the observed results. In addition, the investigation of further REINER sensors can increase the statistics.

Appendix A

IBL Wafer Production 2011

The detailed list of the structures manifactured in the IBL Wafer Production in 2011. In this thesis, the pixel sensor 11 and the guard ring diode 22 are used.

	structure	properties
01	FE-I4 1x2-MCM	slim edge, 13 guard rings, Pixel overlap 250um
02	FE-I4 1x2-MCM	slim edge, 13 guard rings, Pixel overlap 250um
03	FE-I4 1x2-MCM	slim edge, 13 guard rings, Pixel overlap 250um
04	FE-I4 1x2-MCM	slim edge, 13 guard rings, Pixel overlap 250um, w/ temperature resistor
05	FE-I4 SC sensor	different pixel shapes, segmented HV-pad, w/ temperature resistor
06	FE-I4 SC sensor	slim edge, 13 guard rings, Pixel overlap 250um
07	FE-I4 SC sensor	slim edge, 13 guard rings, Pixel overlap 250um, w/ temperature resistor
08	FE-I4 SC sensor	slim edge, 13 guard rings, Pixel overlap 250um, w/ temperature resistor
09	FE-I3 SC sensor	conventional design, 16 guard rings
10	FE-I3 SC sensor	different pixel shapes, 16 guard rings
11	FE-I3 SC sensor	slim edge, 13 guard rings, Pixel overlap 250um
12	FE-I3 SC sensor	pixel shifted stepwise, 16 guard rings, no ganged pixels
13	guard ring diode	pixelated pad, 16 guard rings
14	guard ring diode	conventional design, 16 guard rings
15	guard ring diode	comb like pad v1.2, 16 guard rings, no moderated p-spray
16	guard ring diode	comb like pad v1, 16 guard rings, moderated p-spray
17	guard ring diode	comb like pad v2, 16 guard rings, moderated p-spray, area wide metal
18	guard ring diode	coplanar grid like pad v2, 16 guard rings, grid on n- and p-side
19	guard ring diode	pixelated pad, 16 guard rings
20	guard ring diode	conventional design, 16 guard rings
21	guard ring diode	conventional design, 16 guard rings
22	guard ring diode	coplanar grid like pad v1, 16 guard rings, grid on n-side only
23	guard ring diode	comb like pad v1.2, 16 guard rings, no moderated p-spray
24	guard ring diode	comb like pad v2, 16 guard rings, moderated p-spray, area wide metal
25	guard ring diode	comb like pad v1, 16 guard rings, moderated p-spray
26	GCD	ATLAS production design
27	GCD	ATLAS production design
28	MOSFET	ATLAS production design, p-side
29	MOSFET	ATLAS production design, n-side
30	test structure	for doping profile measurements
31	omegapix sensor	LAL design v4, pixel 50x50um, without fanout
32	guard ring diode	LAL design, 1 guard rings, easily contactable
33	guard ring diode	LAL design, 3 guard rings, easily contactable
34	guard ring diode	LAL design, 4 guard rings, easily contactable
35	guard ring diode	LAL design, 2 guard rings, easily contactable
36	Interpixel structure	LAL desgin, pixel 400, 100 and 50um long
37	omegapix sensor	LAL design v4, pixel 50x50um, without fanout
38	test sensor	for Uni Bonn, 250x50um pixels

Figure A.1: The structures of the IBL wafer production 2011 [28].

Appendix B

Temperature IV Scaling

The comparison between the IV curves calculated at T = 15 °C and measured for the "down" scaling (a) and the "up" scaling (b)

(a) "Down" scaling (T = 22 °C → 15 °C)

(b) "Up"scaling (T = 5 °C → 15 °C)
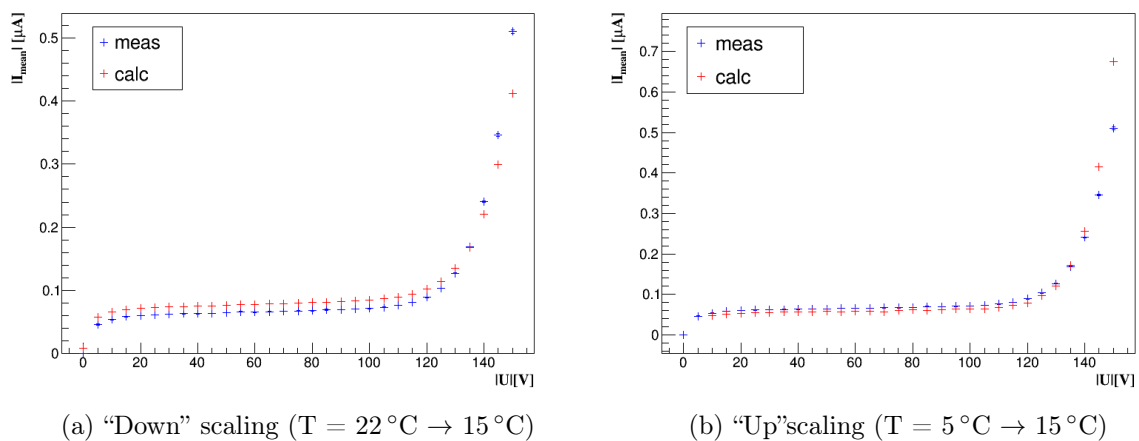
Figure B.1: The calculated IV values with the scaling law 2.10 (red cross) are compared with the measured values (blue cross) at T = 15 °C.

Appendix C

Etching

The zoom-plot of the relative current ratio of the etched designs V0, V1, V4 and 05 of the REINER sensor 312060-07 as a function of the bias voltage.
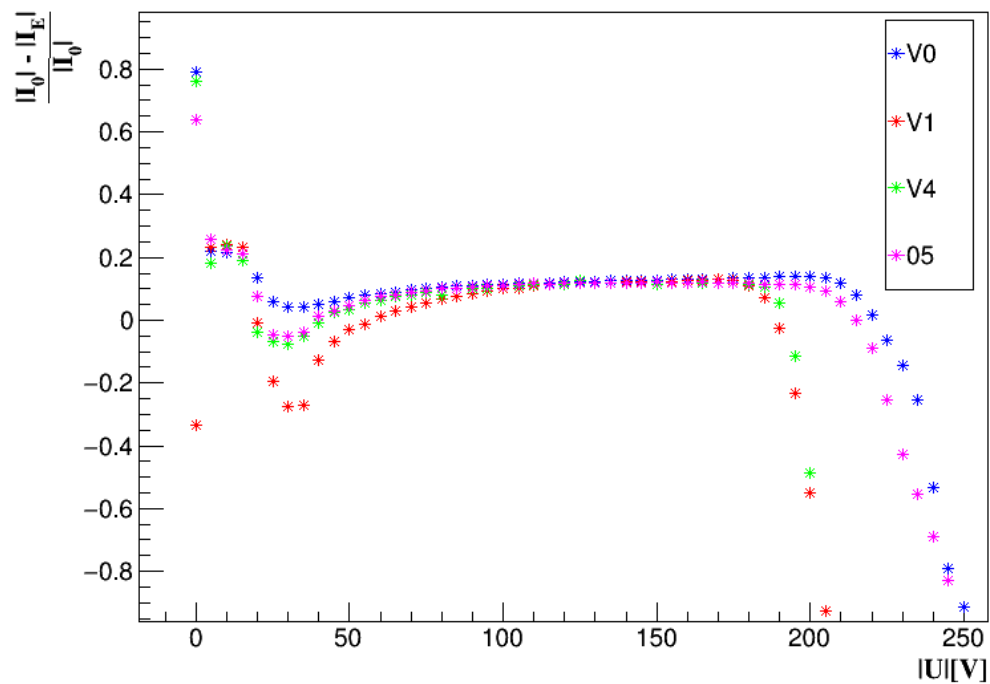
Figure C.1: Zoom in the x- and y-axis of Figure 4.21, to see the oscillation of the relative current ratio around zero.

Appendix D

Guard rings

Guard rings width

In this section of the Appendix D, the guard rings width of the diode 22 (Table D.1) and of the pixel sensor 11 (Table D.2) on the wafer 331831-21 are shown, from the outermost one (guard ring 1) to the innermost in increasing order.

Guard ring	Width (μm)
1	52
2	50
3	47
4	46
5	44
6	17.5
7	17
8	17
9	16.5
10	16.5
11	16
12	16
13	15.5
14	15.5
15	15
16	11

Table D.1: Guard rings width of the diode 22 (wafer 331831-21), shown in Figure 5.8, labelled from 1 (the outermost), in increasing order going inwards of the sensor.

Guard ring	Width (μm)
1	46
2	44
3	17.5
4	17
5	17
6	16.5
7	16.5
8	16
9	16
10	15.5
11	15.5
12	15
13	12

Table D.2: Guard rings width of the pixel sensor 11 (wafer 331831-21), shown in Figure 5.3, labelled from 1 (the outermost), in increasing order going inwards of the sensor.

IV curve of the diode 22 on the wafer 331831-21

The IV curves of the diode 22 on the wafer 331831-21 before and after the guard ring measurements (Section 5.1) are shown.
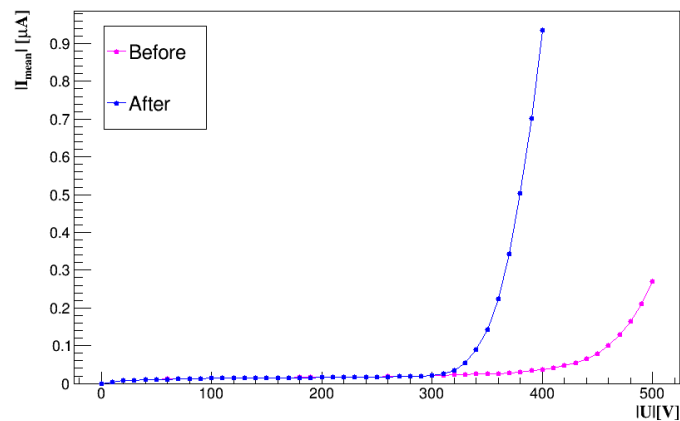
Figure D.1: IV curves of the diode 22 (331831-21) taken before (magenta line) and after (blue line) the measurements shown in Figure 5.10.

Guard rings measurements on the diode 22 on the wafer 331831-21

The comparison of the measurements in the opening and in the no-opening in the guard rings of the diode 22 (wafer 331831-21) are shown in Figure D.2 for the guard rings 3, 5, 6 and 7; in Figure D.3 for the guard rings 8, 9, 10, 11, 12; in Figure D.4 for the guard rings 13, 14, 15.

(a) Guard ring 3

(b) Guard ring 5

(c) Guard ring 6
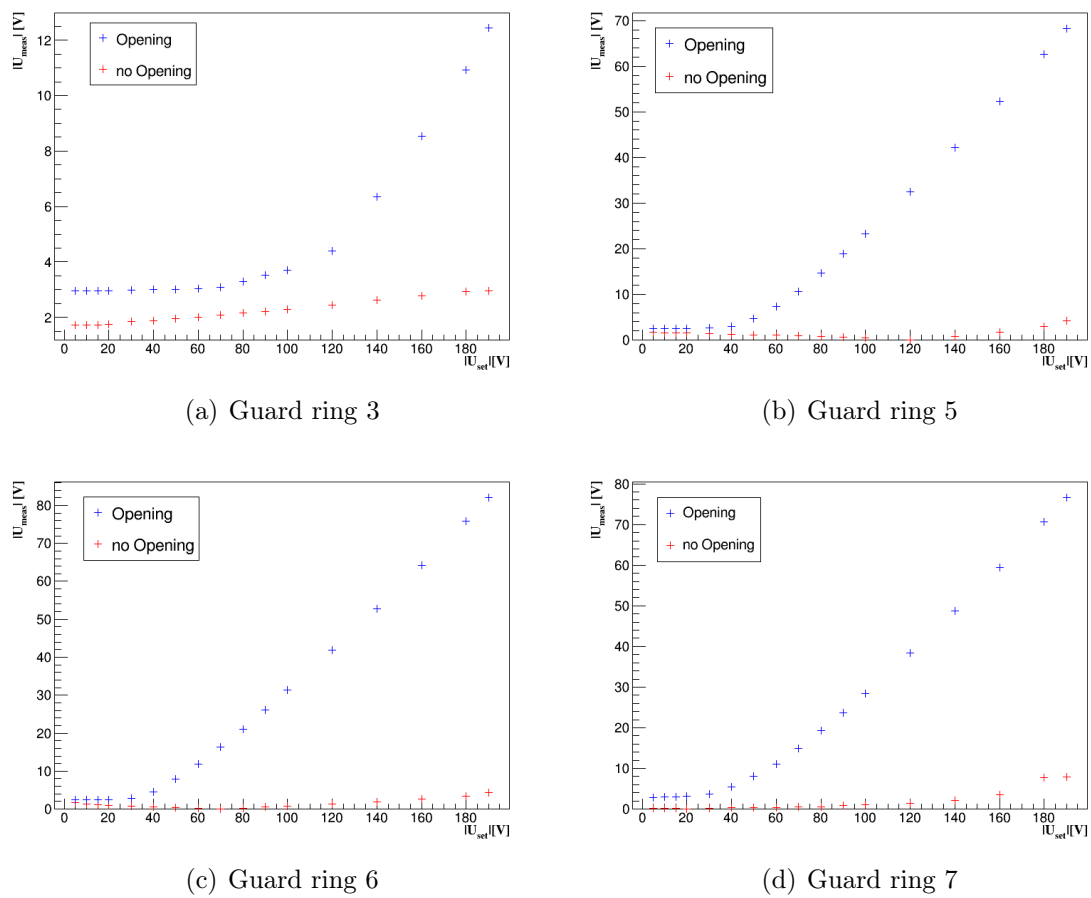
(d) Guard ring 7

Figure D.2: Comparison between the guard ring measurements in the opening (blue cross) and in the no opening (red cross) for the guard ring 3, 5, 6, 7.
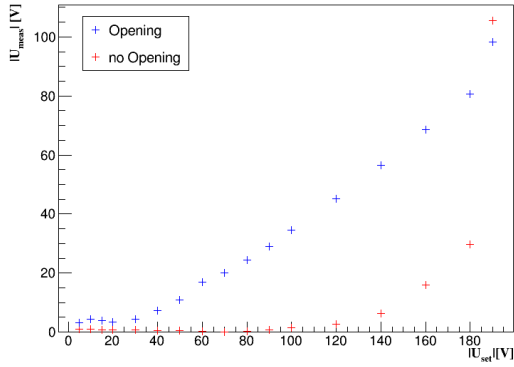
(a) Guard ring 8
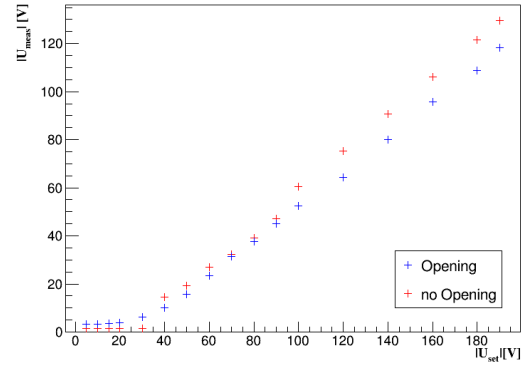
(b) Guard ring 9
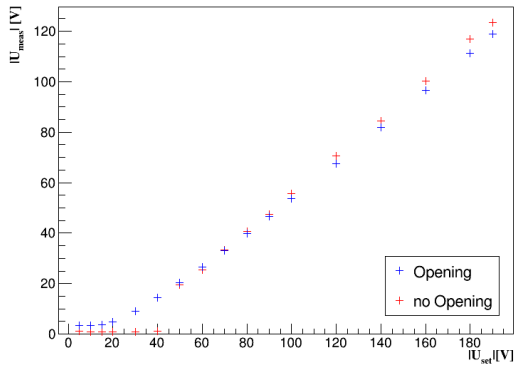
(c) Guard ring 10
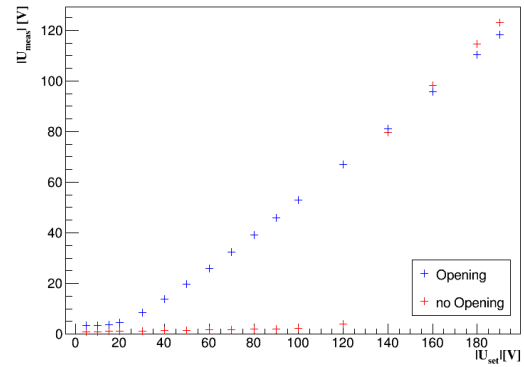
(d) Guard ring 11
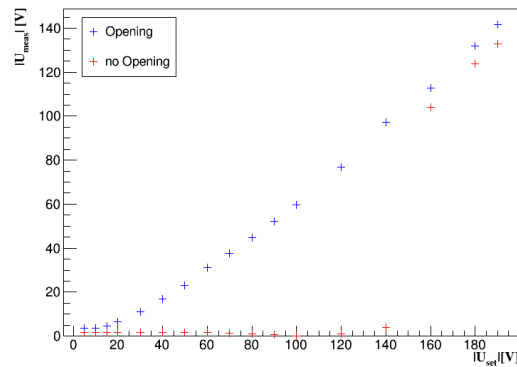
(e) Guard ring 12

Figure D.3: Comparison between the guard ring measurements in the opening (blue cross) and in the no opening (red cross) for the guard ring 8, 9, 10, 11, 12.
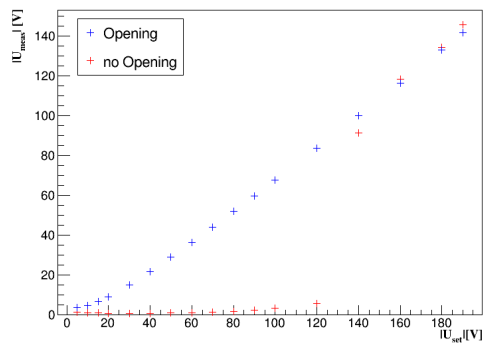
(a) Guard ring 13
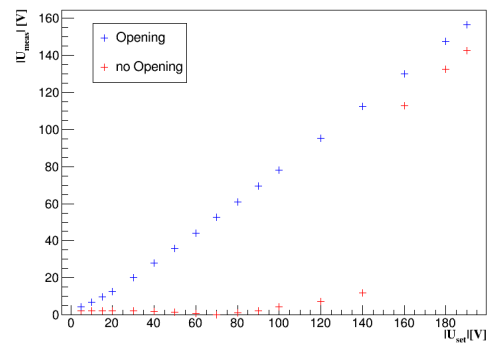
(b) Guard ring 14
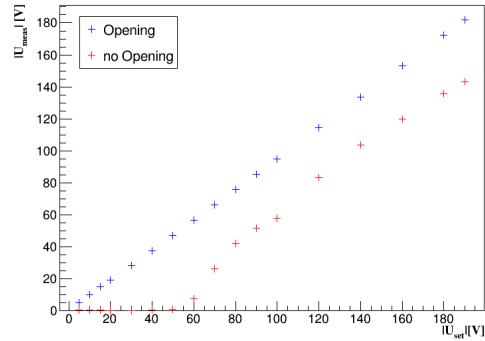
(c) Guard ring 15

Figure D.4: Comparison between the guard ring measurements in the opening (blue cross) and in the no opening (red cross) for the guard ring 13, 14, 15.

Guard ring measurements of the diode 22 and the pixel sensor 11 on the wafer 331831-22

The guard ring measurements in the opening of the diode 22 and the pixel sensor 11 (wafer 331831-22) are shown in Figure D.5a and Figure D.5b to be compared with the measurements in the no-opening in Figure 5.17 for the diode and in Figure 5.18 for the pixel sensor.
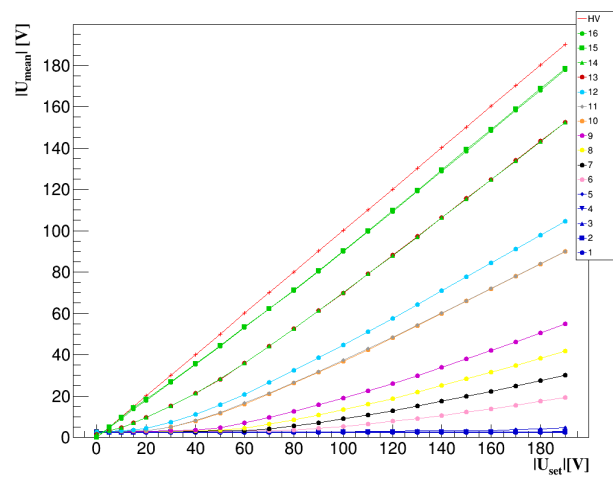
(a) Diode 22
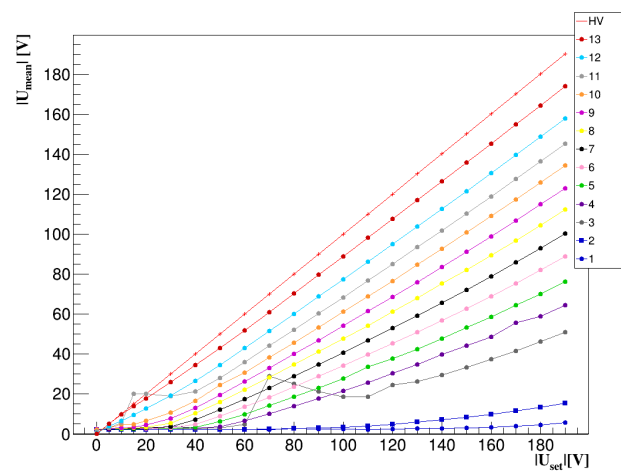
(b) Pixel sensor 11

Figure D.5: Guard ring measurements of the diode 22 (a) and the pixel sensor 11 (b) of the wafer 331831-22, in the opening.

Guard rings of the REINER Sensor 310894-22

The measurements on the guard rings of the eight pixel designs of the REINER sensor 310894-22 are shown in Figure D.6 for the guard rings 5, 6, 7, 8, and in Figure D.7 for the guard rings 9, 10, 11, 12, 13.

(a) Guard ring 5

(b) Guard ring 6

(c) Guard ring 7
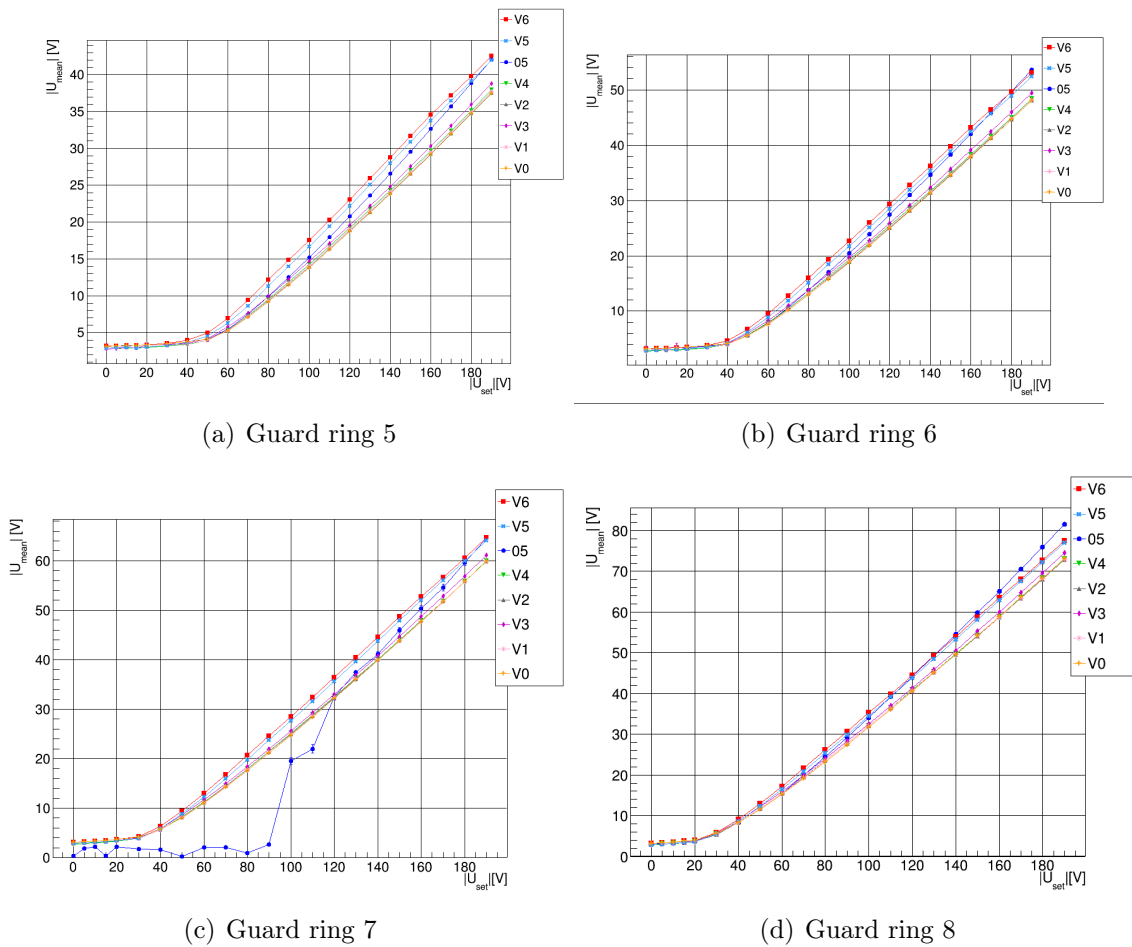
(d) Guard ring 8

Figure D.6: Measurements taken on the guard ring 5, 6, 7, 8 for the eight designs of the REINER sensor 310894-22.
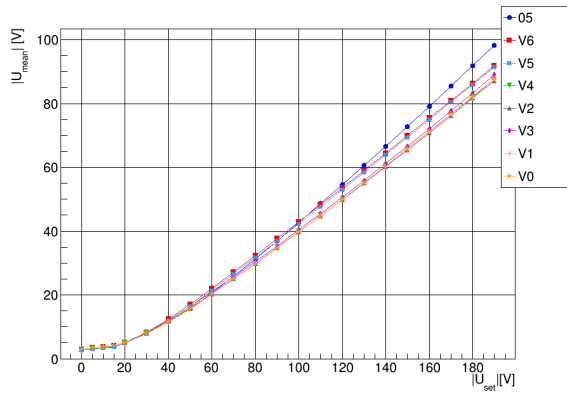
(a) Guard ring 9
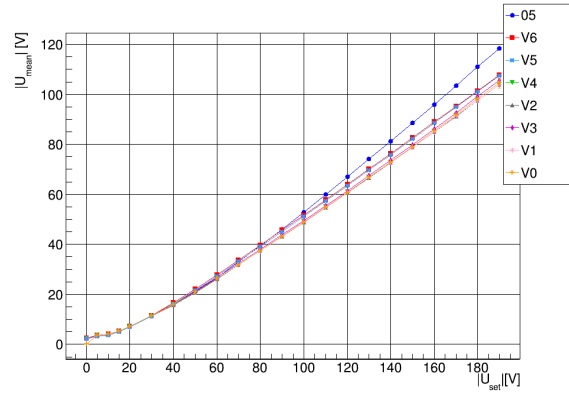
(b) Guard ring 10
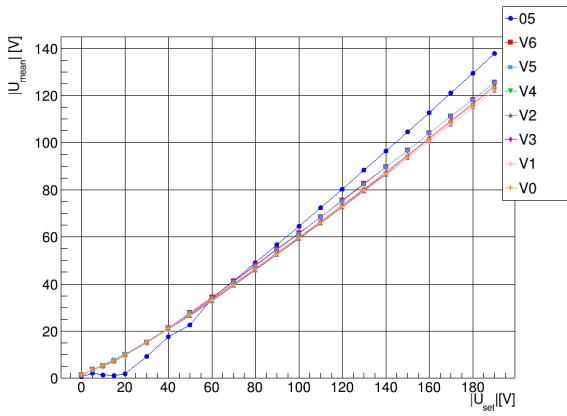
(c) Guard ring 11
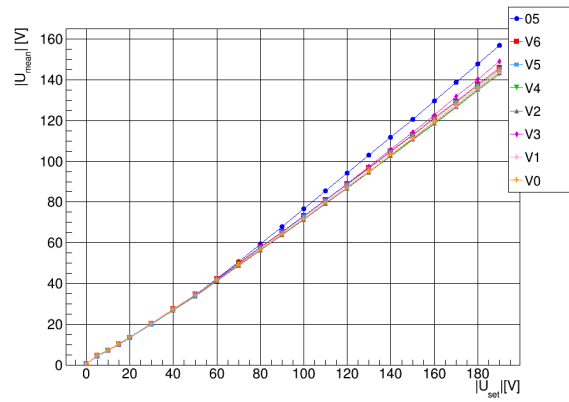
(d) Guard ring 12
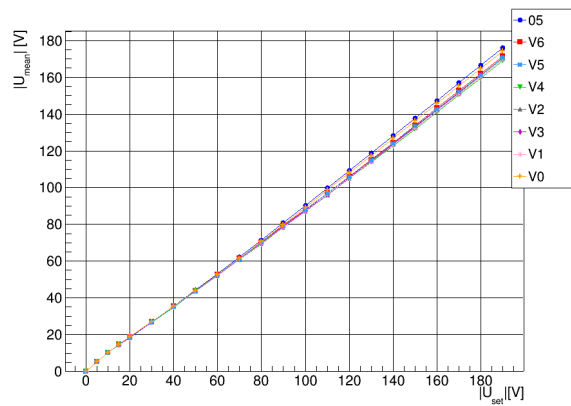
(e) Guard ring 13

Figure D.7: Measurements taken on the guard ring 9, 10, 11, 12, 13 for the eight designs of the REINER sensor 310894-22.

Influence between Different Designs

The combinations of biased and measured designs listed in Table 5.1, except the ones the text in Figure 5.23 and Figure 5.24, are shown in Figure D.8 and Figure D.9.
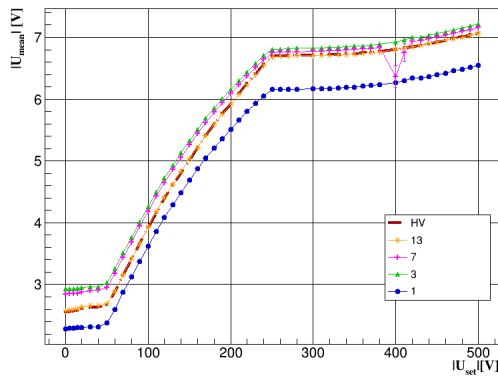
(a) Bias on V0, measuring GR of V2
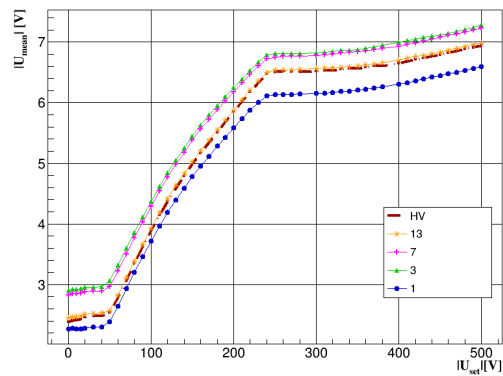
(b) Bias on V1, measuring GR of V0
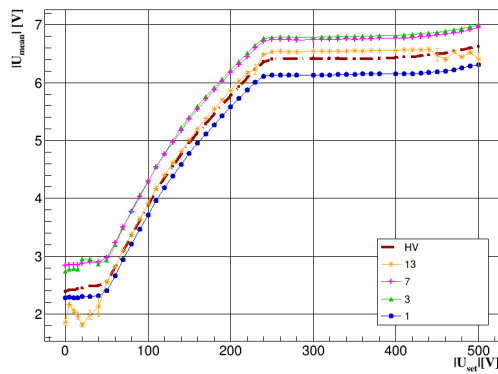
(c) Bias on V2, measuring GR of V0
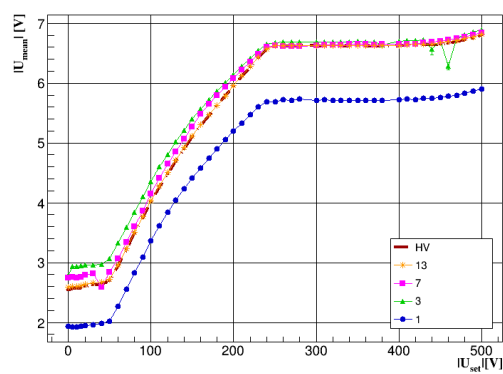
(d) Bias on V2, measuring GR of V3

Figure D.8: The influences among the different pixel designs in the REINER 310894-22.
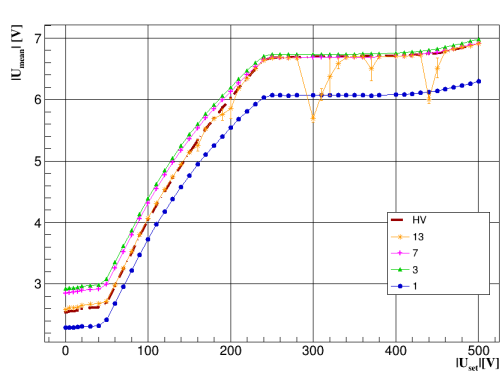
(a) Bias on V2, measuring GR of V4
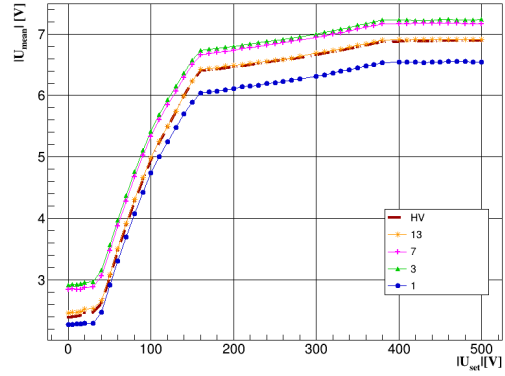
(b) Bias on V6, measuring GR of V0
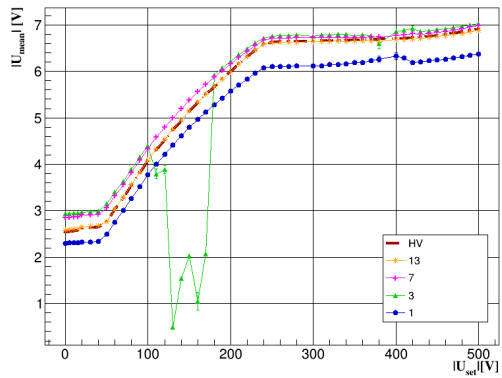
(c) Bias on V3, measuring GR of V2
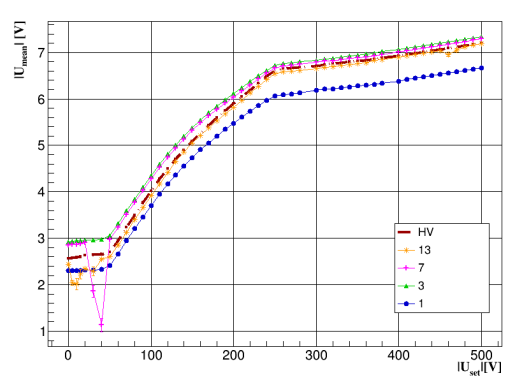
(d) Bias on V4, measuring GR of V2
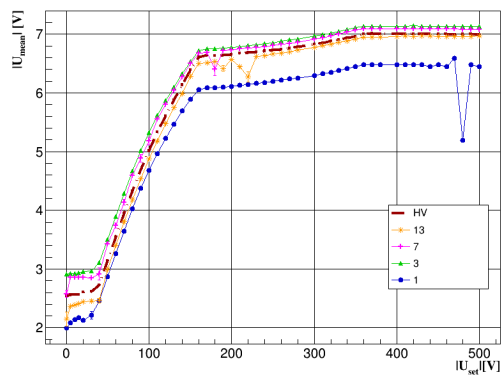
(e) Bias on V5, measuring GR of V2

Figure D.9: The influences among the different pixel designs in the REINER 310894-22.

Guard ring measurements on the V2 design of the assembly on PCB

The measurements on the guard rings 3, 7, 11 and 13 of the design V2 of the assembly on PCB (Figure 3.13) are presented in Figure D.10.
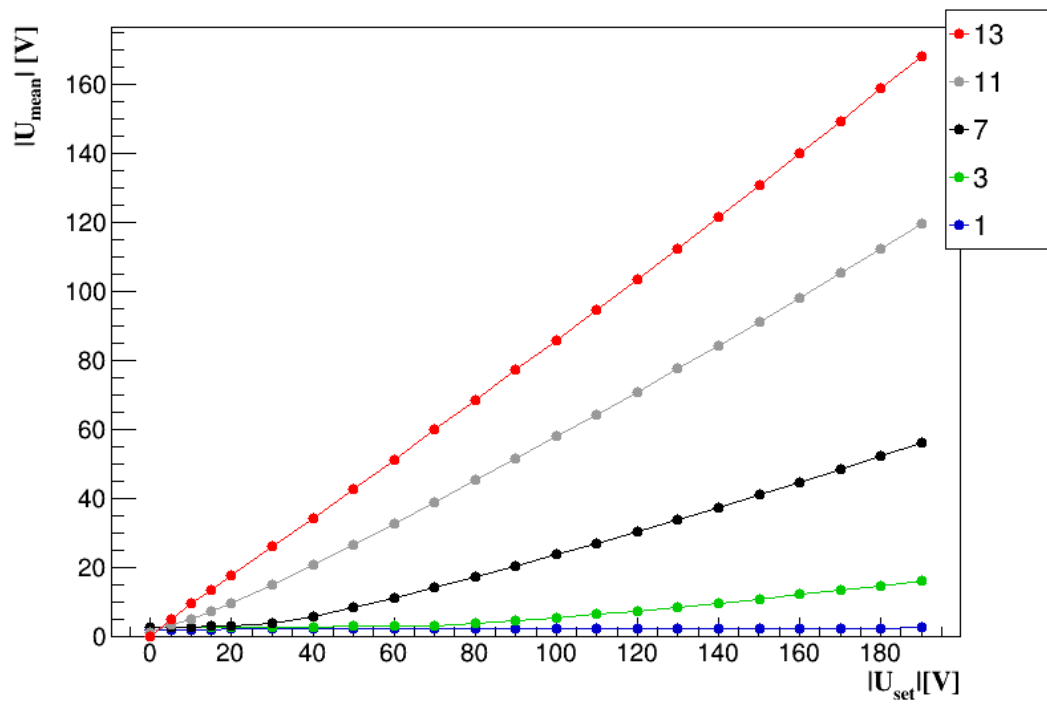
Figure D.10: Guard ring 13, 11, 7, 3 and 1 measurements on the pixel design V2 of the assembly on PCB.

IV curves of the assembly on PCB

The IV curves of the designs V5, V6, V2 and V0 of the assembly on PCB (Figure 3.13) taken before the guard ring measurements are shown in Figure D.11.
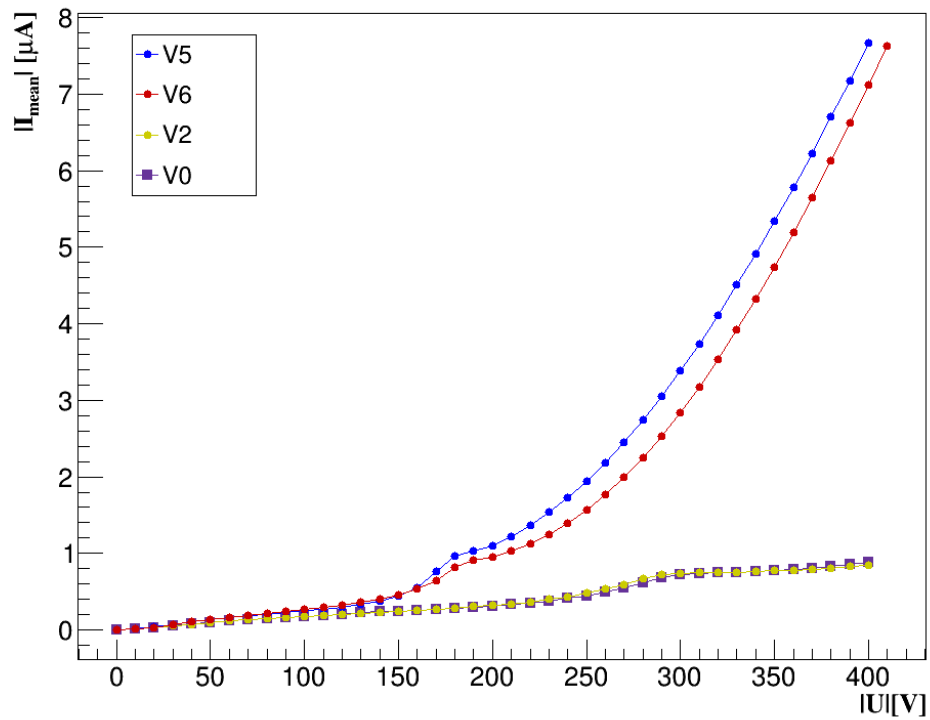
Figure D.11: IV curves of the designs V5, V6, V2 and V0 of the REINER sensor 371409-19 with the Front End A8PL4WH-60-R10.

Bibliography

[1] E. A. Mobs. The CERN Accelerator Complex, 2016, General Photo OPEN-PHO-ACCEL-2016-013, URL: `http://cds.cern.ch/record/2225847`,

[2] CERN website, URL: `https://home.cern/science/experiments`. Accessed January 2020.

[3] CERN website, URL: `https://home.cern/science/accelerators`. Accessed January 2020.

[4] ATLAS website Glossary, URL: `https://atlas.cern/glossary`

[5] Joao Pequenao, *Computer generated image of the whole ATLAS detector*, URL: `http://cds.cern.ch/record/1095924`, accessed January 2020.

[6] J. Pequenao and P. Schaffner, *How ATLAS detects particles: diagram of particle paths in the detector*, 16 Jan 2013, URL: `https://cds.cern.ch/record/1505342`, accessed January 2020.

[7] ATLAS Collaboration, *Performance of the ATLAS track reconstruction algorithms in dense environments in LHC Run 2*, Eur. Phys. J. C **77** (2017) 673, CERN-EP-2017-045, arXiv:1704.07983 [hep-ex]

[8] ATLAS Collaboration, *The ATLAS Experiment at the CERN Large Hadron Collider*, JINST **3** (2008) S08003

[9] The HL-LHC project website, URL: `https://hilumilhc.web.cern.ch/content/hl-lhc-project`, accessed January 2020.

[10] ATLAS Collaboration, *Observation of a new particle in the search for the Standard Model Higgs boson with the ATLAS detector at the LHC*, Physics Letter **B716** (2012) 1-29, CERN-PH-EP-2012-218, arXiv:1207.7214 [hep-ex]

[11] CMS Collaboration. *Observation of a new boson at a mass of 125 GeV with the CMS experiment at the LHC*, Physics Letter **B716** (2012) 30, CERN-PH-EP-2012-220, arXiv:1207.7235 [hep-ex]

[12] ATLAS Collaboration, *Physics at a High-Luminosity LHC with ATLAS*, ATL-PHYS-PUB-2013-007, arXiv:1307.7292 [hep-ex]

[13] ATLAS IBL Collaboration, *Production and integration of the ATLAS Insertable B-Layer*, JINST **13** T05008 (2018), arXiv:1803.00844 [physics.ins-det]

[14] S. Altenheiner et al., *Planar slim-edge pixel sensors for the ATLAS upgrades*, JINST **7** C02051 (2012), DOI: `10.1088/1748-0221/7/02/c02051`

[15] A. Gisen, *Quad module prototypes and design improvement studies of planar n^+-in-n silicon pixel sensors for the ATLAS Inner Tracker Upgrade.* Dissertation, TU Dortmund, **2018**

[16] ATLAS Collaboration, *Technical Design Report for the ATLAS Inner Tracker Pixel Detector*, Technical Report CERN-LHCC-2017-021 ATLAS-TDR-030, CERN, Geneva, Sep **2017**, `https://cds.cern.ch/record/2285585`

[17] ATLAS Collaboration, *Technical Design Report for the ATLAS Inner Tracker Strip Detector*, Technical Report CERN-LHCC-2017-005 ATLAS-TDR-025, CERN, Geneva, Apr **2017**, `https://cds.cern.ch/record/2257755`

[18] ATLAS Collaboration, *Expected Tracking Performance of the ATLAS Inner Tracker at the HL-LHC*, ATL-PHYS-PUB-2019-014, CERN, Geneva, Mar **2019**, `https://cds.cern.ch/record/2669540`

[19] S. M. Sze and M. K. Lee. *Physics of Semiconductor Devices.* John Wiley & Sons, New York, 3rd edition, 2007. ISBN-I 3: 978-0-47 1-1 4323-9

[20] G. Lutz. *Semiconductor Radiation Detectors: Device Physics.* Springer Berlin Heidelberg, 2007. ISBN 978-3-540-71678-5

[21] M. Weers, *Test Beam Studies of Planar n + -in-n Silicon Pixel Sensors with Modified Pixel Implantation.* Master Thesis, TU Dortmund, **2017**

[22] G. F. Knoll, *Radiation Detection and Measurement.* John Wiley & Sons, New York, 3rd edition, 2010. ISBN-13: 978-0470131480

[23] F. Wizemann, *Building and Testing of a Setup for Capacitance Measurements of ATLAS-Pixel-Sensors Under the Influence of High-Voltage.* Master Thesis, TU Dortmund, **2015**

[24] TheNoise, *A PN junction in thermal equilibrium with zero bias voltage applied* (2007)
URL: `https://en.wikipedia.org/wiki/File:Pn-junction-equilibrium-graphs.png`

[25] M. Benoit, *Étude des détecteurs planaires pixels durcis aux radiations pour la mise à jour du détecteur de vertex d'ATLAS.* Dissertation, Université Paris XI, Orsay, **2011**

[26] A. Raytarowski, *Comparison of Leakage Current Characteristics of the Pixel Designs of Irradiated and non-Irradiated REINER Pixel Sensors.* Master Thesis, TU Dortmund, **2018**

[27] W. R. Leo, *Techniques for Nuclear and Particle Physics Experiments. A How-To Approach.* Second Revised Edition, Springer-Verlag Berlin Heidelberg GmbH, 1994. ISBN 978-3-540-57280-0

[28] T. Witting, *Slim edge studies, design and quality control of planar ATLAS IBL pixel sensors.* Dissertation, TU Dortmund, **2013**

[29] L. Rossi et al., *Pixel Detectors: From Fundamentals to Applications.* Springer-Verlag Berlin Heidelberg, 2006. ISBN 978-3-540-28333-1

[30] J. M. Klaiber-Lodewigs, *The ATLAS Pixel Sensor - properties, characterization and quality control.* Dissertation, TU Dortmund, **2005**

[31] N. Savic et al. *Investigation of thin n-in-p planar pixel modules for the ATLAS upgrade,* JINST **11** C12008 (2016), DOI: `10.1088/1748-0221/11/12/C12008`

[32] A. Gisen et al. *Investigation of modified ATLAS pixel implantations after irradiation with neutrons,* (2018) DOI: `10.1016/j.nima.2018.08.030`

[33] ATLAS IBL collaboration, *Prototype ATLAS IBL Modules using the FE-I4A Front-End Readout Chip,* JINST **7** P11010 (2012), DOI: `10.1088/1748-0221/7/11/P11010`

[34] V. Mishra et al., *Role of guard rings in improving the performance of silicon detectors* Pranama **65** (2005) 259-272, URL: `https://link.springer.com/content/pdf/10.1007/BF02898614.pdf`

[35] A. Bischoff et al., *Breakdown protection and long-term stabilisation for Si-detectors,* Nucl. Instr. and Meth. in Phys. Res. **A326** (1993) 27-37, DOI: `10.1016/0168-9002(93)90329-G`

[36] M. Benoit et al., *Simulation of guard ring influence on the performance of ATLAS pixel detectors for inner layer replacement,* JINST **4** P03025 (2009), DOI: `10.1088/1748-0221/4/03/P03025`

[37] J. Helmig, *Investigation of Modified Pixel Implantations for planar n^+-in-n Silicon Sensors.* Master Thesis, TU Dortmund, **2015**

[38] M. Wagner et al., *Test Beam and Lab Results of ATLAS Sensors with Modified Pixel Implantations*, 8th Beam Telescopes and Test Beams Workshop, **2020**, URL:`https://indico.cern.ch/event/813822/contributions/3648331/attachments/1979020/3294875/MareikeWagnerBTTB2020.pdf`

[39] Acme Technology Inc., *Probe Needle Specifications - Tip Shapes*, URL: `http://www.acmetechprobes.com/tip-shapes/`

[40] Technology Computer Aided Design (TCAD) website, URL: `https://www.synopsys.com/silicon/tcad.html`

Acknowledgements

Prima di tutto, vorrei ringraziare il prof. Maximiliano Sioli per avermi dato la possibilità di fare questa esperienza, per avermi invogliata a svolgere un progetto di ricerca in hardware, e per avermi seguita con sostegno, pazienza e disponibilità durante questi sei mesi, sopratutto nell'ultimo periodo di scrittura della tesi, nonostante la lontananza.

I would like to thank prof. Kevin Kröninger for kindly welcoming me at the beginning and for being always available for any kind of problems.

I want to express my thanks to Dr. Jens Weingarten from whom I learned the importance of discussing doubts and issues in a constructive criticism.

I would really like to thank Dr Andreas Gisen for guiding me from the very first days at Dortmund. Specifically, I appreciated his help with my accomodation and in introducing me in the department, explaining me all the rules and customs. Also, I'm grateful to him for helping me with the work in the laboratory, how to deal with *die Frustrationstoleranz*, and the scientific way of understanding and presenting the results.

I want to express my gratitude to Mareike Wagner for her precious supervision, whose corrections, suggestions, patience and willingness improved the writing of this thesis.

I want to acknowledge all the members of the "ATLAS Upgrade" group, without whom this work could not have been carried out in the same way: Dr. Felix Wizemann for his relevant advices, Mike Muschak, Valerie Hohm, the precious collaboration and brainstorming with the other master students Falko Barth and Sebastian Pape, and the essential presence of Jonas Lönker in the office, without whose comments, encouragements, break talks and biscuits, I could not have go on in the most stressful days.

I also want to give thank to Nils for being my first friend in Dortmund, for spending good time together and for being always present when I needed his friendly support.

I want to show my gratitude to Janina and Kevin for their kindness, the friendship, and for hosting me during my last days in Dortmund.

I want to really thank all the people of the E4 chair, Markus Alex, Marius, Froch, Myriam, Florian, Isabelle, Hannah, the precious presence of Andrea Teichmann and everyone who welcomed and integrated me in a natural way.

I want to give a big thank to all the Erasmus crew, without whom my Erasmus